DESIGN, PERFORMANCE, AND ECONOMIC ASSESSMENT OF RENEWABLE AND ALTERNATIVE FUEL PRODUCTION PATHWAYS

by

William L. Becker

A thesis submitted to the Faculty and the Board of Trustees of the Colorado School of Mines in partial fulfillment of the requirements for the degree of Master of Science (Engineering).

Golden, Colorado
Date 8/29/2011

Signed: William Becker
William L. Becker

Signed: Robert Braun
Dr. Robert Braun
Thesis Advisor

Golden, Colorado
Date 8/29/2011

Signed: John R. Berger
Dr. John Berger
Acting Department Head
Department of Engineering

ABSTRACT

Harnessing and storing electric power produced from renewable resources through its conversion to transportation fuels broadens the potential for renewable energy integration and serves to mitigate national dependence on crude oil. The focus of this thesis is on the examination of renewable and alternative energy conversion strategies for transportation fuel production. Two mid-scale (50 MW) fuel production plants are presented which demonstrate electricity-to-fuel pathways using renewable electricity and recycled carbon dioxide. The first pathway considers hydrogen (produced from renewably powered electrolysis) as a feedstock to a synthetic natural gas (SNG) production plant, which catalytically converts hydrogen and carbon dioxide to SNG. The second pathway explores the production of gasoline and diesel fuel from renewably powered co-electrolysis of steam and carbon dioxide followed by Fischer-Tropsch synthesis. A third pathway to fuel is presented which considers an alternative means of small-scale hydrogen production using stationary fuel cell technology for the polygeneration of hydrogen, heat, and electricity (CHHP); this strategy enables flexibility of production for meeting the hydrogen demand of a small-scale market penetration of fuel cell vehicles.

The design, thermochemical performance, and economic analysis of these three fuel production plants are presented. The plant efficiencies for the first two production plants are 78% and 50% (HHV), respectively. The cost of fuel production is highly dependent on the operating capacity factor of the plant, and this is a major barrier for pathways which use intermittent renewable energy resources, such as wind. The overall efficiency for the fuel cell-based polygeneration plant is 79.3% (HHV), and the economics of hydrogen production are favorable if electricity prices are high compared to the cost of natural gas.

TABLE OF CONTENTS

LIST OF FIGURES

LIST OF TABLES

ACKNOWLEDGMENTS

I would like to thank my advisor Rob for guiding me along the way to accomplish the greatest feat in my educational career. I have greatly improved my critical thinking ability and communication skills during the past two years with his help. My goal for attending graduate school was to gain knowledge of renewable energy systems, and I accomplished that goal and more with the opportunities that Rob provided for me.

I would like to acknowledge the National Renewable Energy Laboratory for providing funding for the research projects on which my thesis builds. Mike Penev was a great help as my supervisor at NREL. Through many arduous tasks using and debugging Aspen Plus™ software, we pulled through and solved the issues.

CHAPTER 1

INTRODUCTION

Fossil fuels are being depleted at increasing rates, and it is clear that renewable energy and alternative fuels must play a significant role in meeting the future energy demands. The accumulation of carbon dioxide in the atmosphere from burning fossil fuels is a growing concern because of its warming effects on the planet. Renewable pathways to fuels for use in existing infrastructure are a key interest in the interim preceding a transition to more direct renewable energy uses and widespread distributed generation systems. Studies which explore renewable pathways to fuels are essential for determining the capability of potential technologies which can reduce our dependence on fossil fuels and mitigate global warming. This chapter includes a background in renewable energy and transportation fuels production as a motivation for the work in this thesis.

1.1 Importance of Renewable Fuels

The current consumption rate of fossil fuels poses an economic and environmental threat to society. By relying on oil for transportation fuel, the United States is vulnerable to fluctuations in the supply and cost of this resource, which is largely *imported*. Continuous economic growth in countries with large populations, such as China, will further strain the supply of fossil fuels. Many countries which supply the majority of crude oil are in politically unstable regions, and this brings further interest to obtaining energy independence. Energy independence can be improved through harnessing renewable resources, such as wind, to produce synthetic fuels.

In addition to resource depletion, reducing pollution to the atmosphere is a motivating factor to decrease the use of non-renewable fossil fuels. The carbon dioxide emitted from burning fossil fuels is believed to contribute to the warming of the Earth’s atmosphere at a rate that will likely disrupt the stable environmental conditions which exist presently. It is estimated by Tripati et al. [1] that the current composition of carbon dioxide in the atmosphere is more than 25% higher than it has been on Earth for 15-20 million years; a major reason for this increase is the burning of fossil fuels for about 200 years. The stabilized climate associated with the current levels of carbon dioxide is estimated with temperatures 5-10 °F hotter and sea levels 75-120 feet higher than present [2]. There is scientific consensus that the rise in carbon dioxide is mainly caused from the anthropogenic behavior of combusting fossil fuels, and the future effects of global warming could have dire impacts on society.

1.2 The Hydrogen Economy: A Long-Term Prospect

The hydrogen economy is a term to describe a future energy and economic system which is based heavily on hydrogen as an energy carrier. Hydrogen can be produced by renewably powered electrolysis, and this is the most direct and technologically mature way to convert electrical energy to chemical energy (fuel). Hydrogen can potentially be used as fuel for fuel cell vehicles (FCV), heat for both cooking appliances and space heating, and power generation using stationary fuel cell systems. Ideally (no carbon emissions), hydrogen is produced from a renewably powered electrolysis process or biomass refining and used to replace natural gas and petroleum for residential and transportation energy needs. Figure 1.1 illustrates a pathway for the production to end-use in a hydrogen economy. Aside from large scale hydrogen production, additional costs include hydrogen pipeline construction for distribution to homes and fueling stations, and hydrogen-compatible end-use devices which are a major barrier to the hydrogen economy.

Barriers for the hydrogen economy include the replacement of the large fleet of internal combustion engine vehicles with fuel cell vehicles, natural gas pipelines with hydrogen pipelines, and household heat and power generating devices with hydrogen compatible devices. Hydrogen has a low volumetric energy density, so it must be highly compressed before use or transport; storage and transport of hydrogen are energy intensive processes. These issues related to the hydrogen economy invite alternative methods for increasing the utilization and implementation of renewable energy resources.

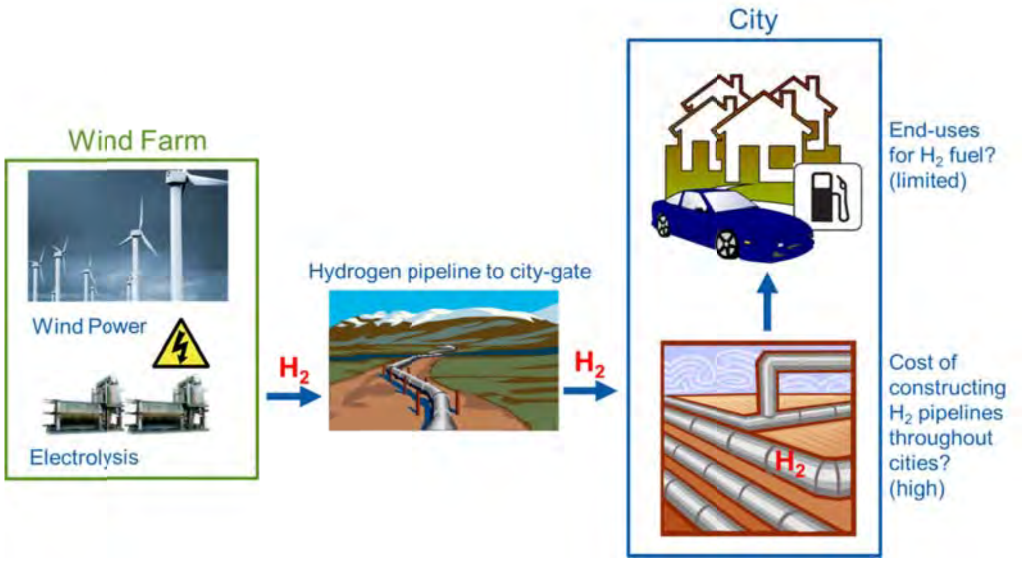

Figure 1.1 Hydrogen pathway scenario in a hydrogen economy

The realization of a hydrogen economy is a long term prospect. Alternatively, hydrogen as an energy carrier can be used for processes which involve conversion to a more readily usable product for which a market demand is currently in place.

1.3 Issues with Harnessing Wind Power

Harnessing the power of wind is inconvenient due to the unpredictability of weather conditions which enable the generation of electricity. Without a storage medium, the electricity must be used as it is generated. The electric power production capability of wind farms does not often coincide with the demand from end-users. If the wind farm is connected to the grid, the electricity can be sold to the utilities companies for distribution to end-users. Unfortunately, most of the best wind resources are not located near highly populated areas; Figure 1.2 shows the relative wind resources throughout the U.S.

Transmission of the wind-generated electricity on long power lines leads to power losses; these losses (P_{loss}) are caused by the resistance (R) in the transmission lines ($P_{loss}= i^2R$), which increases with distance. Ramping up the voltage lowers the transmission power losses by lowering the current (*i*), but the process of increasing the voltage also causes some power loss.

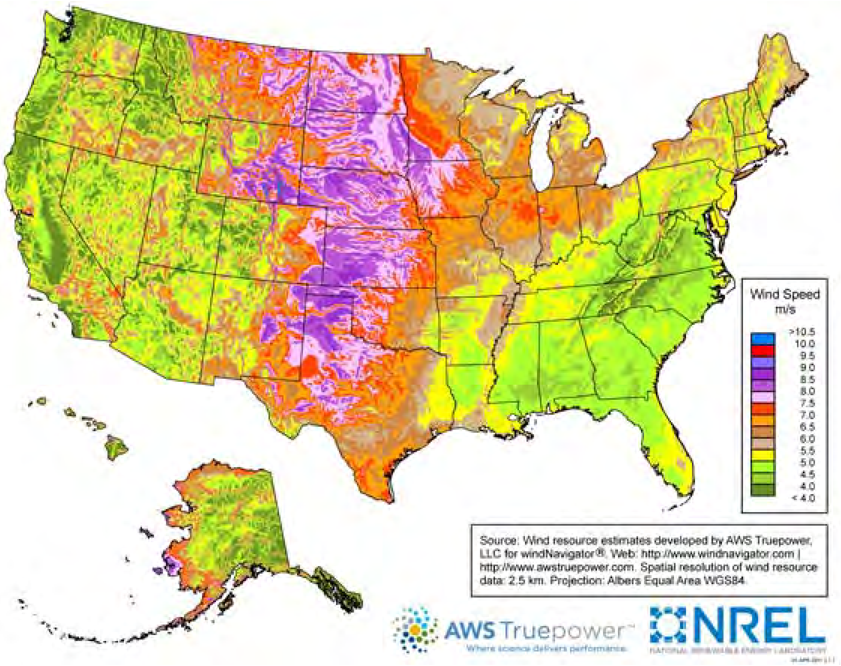

Source: Wind resource estimates developed by AWS Truepower, LLC for windNavigator®. Web: http://www.windnavigator.com | http://www.awstruepower.com. Spatial resolution of wind resource data: 2.5 km. Projection: Albers Equal Area WGS84.

Figure 1.2 Wind resources throughout the U.S. [3]

As an alternative to generating electricity for the immediate demand, storing the electric energy is a topic of great interest for renewable energy generation due to its intermittent nature and remote locations. Storing electric energy directly into batteries is one of the most efficient ways to preserve the energy generated from renewable resources, but capacity limitations of batteries are currently too great to economically store enough energy at utility-scales. Using the generated electricity to compress air or pump water to elevated heights are other ways of storing the potential energy of electric power; these strategies also come with conversion inefficiencies and transmission power losses.

The issue of storing the power generated by wind through its conversion to fuel is becoming a topic of great interest. Storing energy as a fuel requires first the conversion of the wind resource to electricity, and then the electricity must be used to process chemical molecules into a useful fuel. While hydrogen production from wind-powered electrolysis has been considered for this type of process, the current infrastructure and demand for hydrogen is small. Alternatively, the market for natural gas and liquid fuels such as gasoline and diesel is large.

1.4 Carbon Dioxide Recycling

Carbon dioxide is produced in every fossil fuel conversion process. Many sources contribute to carbon dioxide emissions: from the large (500-1200 MW) coal-fired power plants to the gasoline-powered car. Especially regarding large power plants, potential governmental policies for reducing the rate of carbon dioxide emissions are inviting research into methods for carbon capture and storage (CC&S) from power plants. Carbon dioxide emissions policies are also promoting research into alternative methods of fuel and electricity generation from which CC&S is accomplished more easily (e.g. gasification of coal). A difficult and controversial task of CC&S is storage; there is no fail-safe and cost effective method for storing carbon dioxide (e.g. underground) which ensures that it will not be eventually released.

There is growing interest in carbon dioxide "recycling" by which the net emissions of carbon dioxide to the atmosphere are reduced or eliminated. This recycling means re-using the captured carbon dioxide to produce useful fuels again. While using carbon dioxide derived from fossil fuels is not a carbon-neutral cycle (or renewable), it enables a second use of the carbon before being emitted to the atmosphere. Using the same methods of CC&S from fossil fuel power plants, a biomass-fueled power plant utilizing CC&S would make the cycle carbon neutral and renewable.

One example of both re-using and storing carbon dioxide is to use it for enhanced oil recovery (EOR). In North Dakota, the Great Plains Synfuels Plant (GPSP) gasifies coal for synthetic natural gas production, and it captures and transports the carbon dioxide from its site to the reservoir for EOR, where it is then pumped into the reservoir to extract additional oil. There are numerous wind turbines (and potential for more) in

North Dakota, but there is not a large population nearby to demand the electricity that is produced by them. Recycling the carbon dioxide from the existing pipeline in a chemical conversion process, which could store the power produced from the wind turbines, is one option that can slow the emissions of carbon dioxide to the atmosphere while producing valuable fuel.

Presently, there are very few power plants or fuel production plants that employ CC&S because it is not cost effective, and there are not enough stringent governmental policies which incentivize the process. For large-scale renewable energy penetration into the energy market, both science and government will have to increase the capabilities and motivations for CC&S.

1.5 Pathways to Transportation Fuels

Conventional transportation fuels include gasoline and diesel, which are produced by refining crude oil. Alternative transportation fuels include compressed natural gas (CNG), hydrogen, and biofuels (e.g. biodiesel and ethanol). Synthetic production pathways to various transportation fuels are shown in Figure 1.3; the bold red arrows indicate the pathways which will be explored in this thesis.

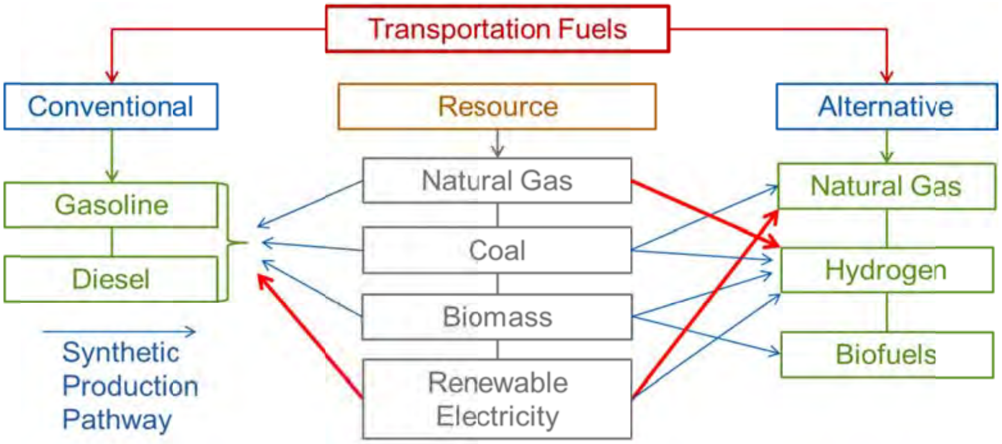

Figure 1.3 Pathways to synthetic transportation fuels

There are various strategies and technologies used to accomplish the production of synthetic fuels. One strategy employed to convert coal or biomass (solids) to liquid fuels is gasification followed by Fischer-Tropsch synthesis. The gasification process produces a chemically reactive syngas (hydrogen and carbon monoxide), and the syngas is catalytically converted to hydrocarbons by the Fischer-Tropsch process. Natural gas (NG) can be reformed into syngas, whereby either a Fischer-Tropsch process converts it to liquid fuels or a purification process is used to produce hydrogen. Biofuels such as ethanol can be produced by breaking down the cellulous of organic matter (biomass) into sugars, and fermenting the sugars into alcohol.

Concerning the electricity-to-fuels pathway, electricity must be produced by an energy source, so there must be another process that generates electricity before the electricity can be converted to fuel. Conventional methods of electricity generation use the heat from coal or natural gas combustion. It would be inefficient and wasteful to use coal or natural gas for electricity generation (e.g. electricity from the grid) followed by an electricity-to-fuels process because there are more direct ways to the fuel product, as shown in Figure 1.3. Alternatively, using electricity produced from a renewable resource such as wind allows a more direct conversion of the energy source, and there are no additional carbon emissions. To produce fuel from electricity, an electrolytic process must be involved; this process electrochemically converts chemical molecules (e.g. water and/or carbon dioxide) into a useful fuel (e.g. hydrogen or syngas). Water can be converted directly to hydrogen by electrolysis, but the production of hydrocarbons requires a carbon source; recycling carbon dioxide which is captured from processes described in *Section 1.4* can provide this carbon source.

The conventional method for hydrogen production is a process called steam methane reforming (SMR), which catalytically reforms methane (from natural gas) to hydrogen and carbon monoxide. Further processing is required to produce pure hydrogen, but this is a technologically mature process which is used commonly in the oil refining industry. The SMR process has been a proposed strategy for distributed, small-scale hydrogen production to make hydrogen available for FCVs. SMR is not a renewable process for hydrogen production, and carbon dioxide emissions are not mitigated by this strategy.

There are several common factors which influence the viability of all transportation fuel pathways:

- *Production*
    - Conversion of resource to useful fuel
    - *The focus of this thesis*
- Transmission
    - Long distance transport from production plant to city-gate
- Distribution
    - Complex transport network throughout the city.
- Fueling stations
    - Storage and dispensing to consumer

Production involves the conversion of the energy resource into useful fuel; this could be a large, centralized plant or a small-scale, distributed plant. For example, an oil refinery is a large centralized plant which produces gasoline and diesel fuel by processing the crude oil. Transmission refers to long distance travel, most commonly referring to pipeline transport from the production plant to the city-gate. Tanker trucks traveling long distances from the oil refinery to the city-gate could also be regarded as transmission, although the same trucks would be responsible for distribution to the fueling stations. Distribution refers to the transportation network to deliver the fuel throughout the city to the consumer or fueling station. The fueling stations are used to store the delivered fuel and dispense it to the consumer on-demand. Following the production of a fuel, the transmission, distribution, and fueling station (TD&F) factors add cost and inefficiency to the process of delivering the produced fuel to the consumer. While this thesis does not focus on in-depth cost and efficiency analysis for TD&F, it is clear that avoiding additional costs and inefficiencies associated with TD&F is beneficial.

1.6 Thesis Focus: Renewable and Alternative Pathways to Fuel Production

This thesis focuses on renewable and alternative strategies for transportation fuel *production*. Two mid-scale (~50 MW) fuel production plants demonstrate options for the electricity-to-fuels pathway using renewable electricity and recycled carbon dioxide. The first study (Chapter 2) considers hydrogen (produced from renewably powered electrolysis) as a feedstock to a synthetic natural gas (SNG) production plant, which catalytically converts hydrogen and carbon dioxide to SNG. The second pathway (Chapter 3) presents the production of gasoline and diesel fuels from renewably powered co-electrolysis of steam and carbon dioxide followed by Fischer-Tropsch synthesis. An alternative strategy (Chapter 4) to SMR for meeting the hydrogen demand of small-scale FCV market penetration using stationary fuel cell technology for the polygeneration of hydrogen, heat, and electricity (CHHP) is presented.

1.6.1 Mid-scale Fuels Production Plants

Using renewable energy resources to produce fuel limits the plant size due to the geographical barriers and the diffuse and intermittent nature of resources such as wind and solar energy. With enough geographical area and favorable weather conditions, wind energy can produce electricity at scales up to 800 MW for the largest U.S. wind farms. These large wind farms are only feasible in select areas, and it is necessary to scale the production plant down to accommodate the capabilities of smaller wind farms. Also, the fuel production plant capacity should be sized to less than that of the wind farm, so that a higher operating capacity (percentage of time that the plant is operating at full capacity) can be obtained; if only a portion of the wind turbines are operational at a given wind farm, the plant could still run at a high capacity. The strategy of under-sizing the plant to the wind farm will increase the capacity factor to some degree, but the plant capacity factor will only be slightly greater than that of a wind farm (30-40%). The effects of capacity factor on the economics of fuel production will be explored for the mid-scale plants presented in Chapters 2 and 3.

While the capacity factor is important, it is also necessary to have a large enough production plant to benefit from the economy of scale for the capital investment of the plant. The scale of the two fuel production plants modeled in this thesis is chosen to be about 50 MW, which considers aspects of operating capacity and economy of scale from which the main energy source is a wind farm. The following fuel production plants are options to increase the renewable energy portfolio for the gas fuel and transportation markets while recycling carbon dioxide.

1.6.2 Hydrogen (from Electricity) to SNG

Natural gas, comprised mostly of methane, is the most common fuel for residential and commercial building use, and there is also a growing transportation sector using CNG-fueled vehicles (NGV). The natural gas industry has established an extensive transport network of piping to deliver natural gas to homes, buildings, and to a lesser extent, CNG fueling stations. CNG fueling stations are mostly found in urban areas where fleets of bus and taxi-cab NGVs are common. Using renewable sources of energy to eventually produce a synthetic natural gas (SNG) would take advantage of the established transport and end-use infrastructure to leverage the value of the SNG product. Figure 1.4 shows the distribution network of natural gas pipelines in the U.S. and their proximity to power plants. It is clear that the network is extensive, and the pipelines are located close to existing power plants.

The U.S. has approximately 300 thousand miles of natural gas pipeline. An estimate for the cost of constructing an equivalent length of hydrogen pipelines (assuming 12 inch diameter) is $160 to 300 billion [5][6]; these costs are not inclusive of decommissioning the existing natural gas pipelines. The task of building pipelines in highly populated and developed cities is even more complex than just lengthy rural transport pipelines due to concerns of avoiding other infrastructure and general safety. In addition to transport costs, the replacement of appliances which are designed to use natural gas (stoves, furnaces, etc.) is an indeterminate large cost for a hydrogen economy. Regarding the transportation market for hydrogen and compressed natural gas, fueling stations are required. Storage of natural gas is less energy and cost intensive due to the increased volumetric energy density of natural gas compared to hydrogen. Although much less abundant than gasoline fueling stations, there are many more compressed natural gas stations currently in place than hydrogen fueling stations.

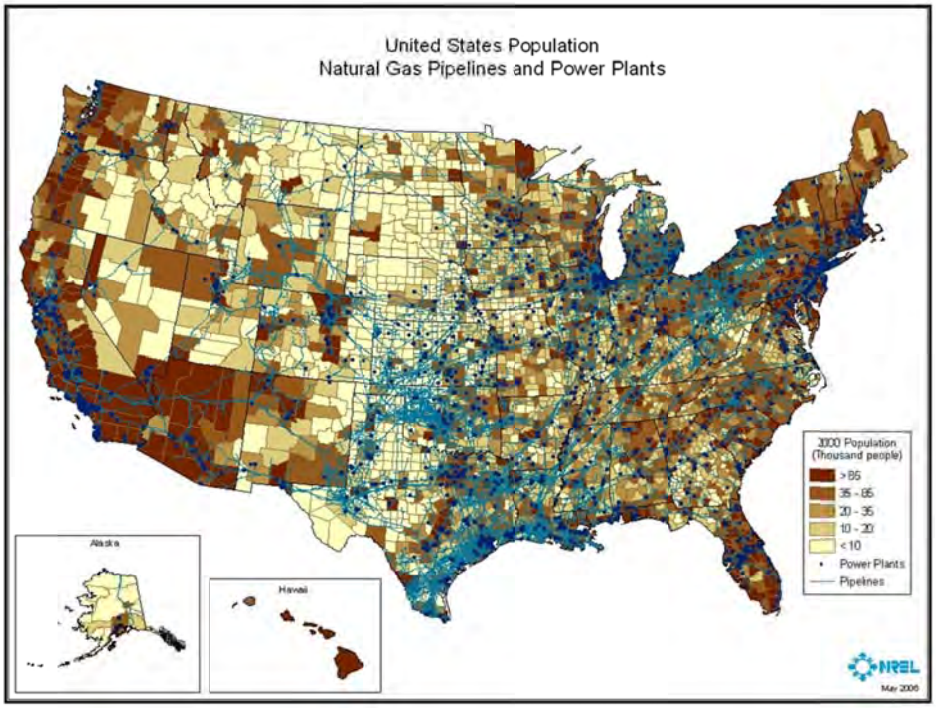

Figure 1.4 Natural gas pipeline infrastructure and power plant locations [4]

Renewably generated hydrogen can be produced by wind-powered electrolysis, which is a commercially available technology. The hydrogen can then be converted to SNG with conventional technologies in a process called methanation, and the SNG can be used as a fuel in the current infrastructure. Figure 1.5 illustrates an alternative pathway architecture in which the hydrogen is converted to SNG at the city-gate, whereby the existing natural gas pipelines are used to distribute the fuel. In comparison to the hydrogen pathway architecture from Figure 1.1, the additional costs of SNG production replace the additional costs of the distribution network and end-use applications.

As shown in Figure 1.5, the electrolysis plant is located at the wind farm, so the hydrogen must be piped to the city-gate, where the SNG plant is located. The carbon dioxide feedstock comes from a power plant which is also located at the city-gate. The SNG is compressed and piped using the NG infrastructure, and it is distributed throughout the city to fueling stations and residential consumers.

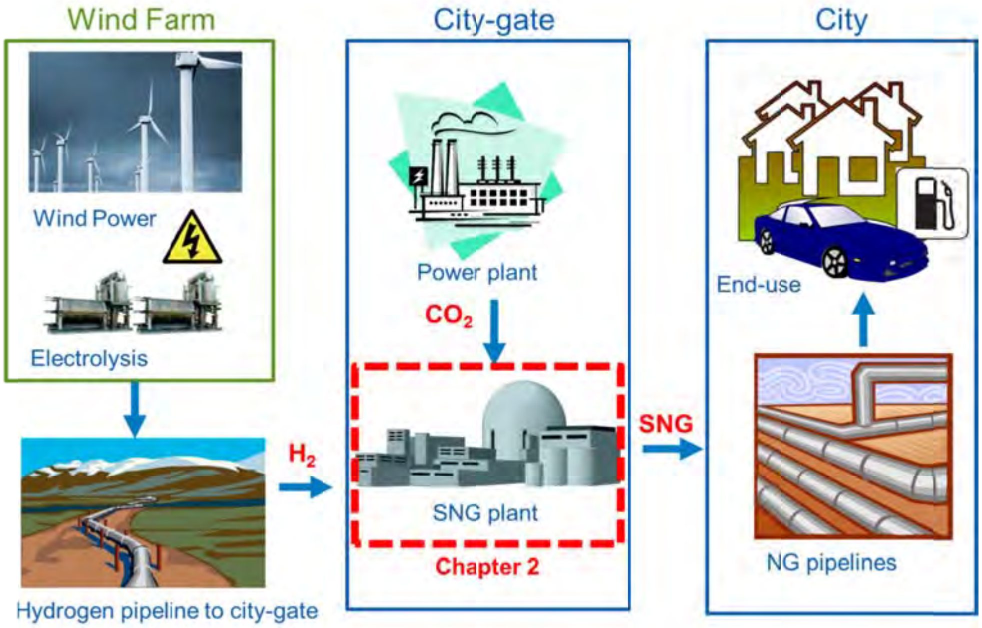

Figure 1.5 Hydrogen from wind-powered electrolysis to SNG production architecture

The SNG plant is located at the city-gate to allow the carbon dioxide to be delivered locally, while the hydrogen production is assumed to be at a location favorable for a wind farm. Although there is still the cost of a hydrogen pipeline in this scenario, the majority of this pipeline would span a relatively low-populated, rural area on which a pipeline is more easily built. The alternative is to locate the methanation plant near the hydrogen producing wind-powered electrolysis plant, but this would require both a carbon dioxide pipeline to the plant and an additional natural gas pipeline to the city-gate. By locating the plant at the city-gate, the SNG plant can easily take advantage of the existing natural gas compression stations and pipelines for distribution throughout the city.

It is recognized that natural gas is a relatively cheap utility in the energy market, and renewable hydrogen is much more expensive; this will make the SNG more expensive than conventional natural gas. In addition, the sources of carbon dioxide are limited because there are few power plants which currently employ CC&S. It becomes a challenge to warrant the production of SNG using this pathway by comparison to the present natural gas market, so it is emphasized that the motivation of this study is to increase the market penetration of renewable energy through its conversion to a usable fuel. The "hydrogen to SNG" study in this thesis aims to *quantify* the performance and economics of a renewable pathway to SNG by way of converting renewably generated hydrogen (from electrolysis) with recycled carbon dioxide.

1.6.3 Electricity to Gasoline & Diesel

The hydrogen economy would satisfy the transportation market by using hydrogen for fuel cell-powered vehicles. As mentioned above, establishing an infrastructure for distributing hydrogen throughout cities (to fueling stations) would be expensive. Additional pipelines and fueling station equipment are required to establish an infrastructure for the transportation market, and it is estimated that the costs of constructing a hydrogen delivery infrastructure to serve 40% of the light duty vehicle fleet is greater than $500 billion [6]. These costs motivate research into alternative renewable energy pathways to satisfy the transportation fuels demand.

Liquid fuels have a high volumetric energy density and are easily stored and used for vehicles. Renewably generated liquid fuels can supply some of the transportation fuel demand. The Fischer-Tropsch process involves the conversion of syngas (hydrogen and carbon monoxide) to higher chain hydrocarbons which can then be processed into gasoline and diesel liquid fuels. The resource for syngas generation must be renewable in order to have a renewably generated liquid fuel. Several methods are available for producing renewable syngas; one method is wind-powered co-electrolysis of carbon dioxide and water; Figure 1.6 illustrates this electricity to liquid fuels pathway architecture. The co-electrolysis and liquid fuels production plant would be located at the wind farm site to capture the generated electricity without suffering transmission losses. The fuel would be transported to fueling stations for dispensing to cars and trucks.

The carbon dioxide can be supplied by a power plant or fuel production plant which utilizes CC&S, such as the GPSP. In a future scenario, the carbon dioxide source for co-electrolysis could include a biomass gasification plant, but no such commercial plants exist at this time. The product gasoline and diesel fuels can directly be used in the transportation market.

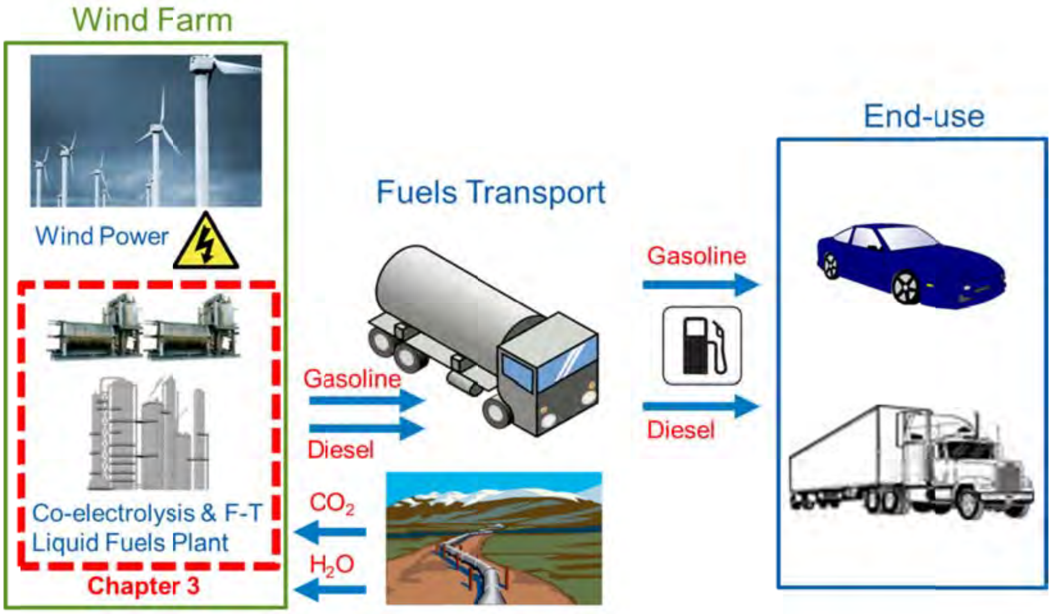

Figure 1.6 Electricity to liquid fuels production architecture

In comparison to the SNG production plant, the liquid fuels production plant in this study bypasses the separate hydrogen production process and creates a useable fuel directly from the wind-generated electricity. This eliminates the need for a hydrogen pipeline, but it requires a carbon dioxide pipeline to the plant, such as the one from the GPSP. A water source is assumed to be available near the wind farm. The market value for gasoline and diesel fuels is higher than that of natural gas; a 3.50 $/gal cost of gasoline is equivalent to 28 $/MMBTU, and the average cost of natural gas in the U.S. is

10 \$/MMBTU. The energetic equivalent market value for gasoline is almost three times higher than that of natural gas, so the economics of a renewable conversion process to gasoline is leveraged in comparison to SNG production. It should be noted if the natural gas transportation market grows significantly, the demand and value of natural gas will increase. This study aims to *quantify* the costs of a renewable pathway to gasoline and diesel fuels by way of wind-powered co-electrolysis of water and carbon dioxide and subsequent Fischer-Tropsch synthesis.

1.6.4 Small-Scale Hydrogen Production using SOFC Polygeneration

An alternative pathway to hydrogen from natural gas SMR is to combine the fuel production with heat and power generation (CHHP). Distributed generation is a scenario where an increased number of small-scale power generating units are distributed throughout the grid. Distributed generation allows for increased high efficiency power generation and flexibility for producing fuels at smaller-scales. Small-scale hydrogen production can more closely match the demand of FCVs.

Fuel cells are power generating devices which are receiving increased attention for their high efficiency compared to conventional methods (e.g. internal combustion engines). Solid oxide fuel cell (SOFC) systems exhibit high overall efficiency, especially when more than one useful commodity is produced. Co-generation is generally considered the generation of two products, such as electricity and heat (CHP), while the generation of three or more products is termed polygeneration (e.g. CHHP). SOFC units are attractive for near-term implementation because they can operate on natural gas. As a transition to a large market demand for hydrogen, small-scale production is preferred. By employing polygeneration, the plant capital investment is leveraged across all co-products, potentially offering lower hydrogen unit costs.

Figure 1.7 illustrates the architecture for the SOFC CHHP plant. The plant would be located near a large building or building cluster for which the electricity and heat is used. A fueling station to dispense the produced hydrogen would be co-located near this building, so no hydrogen transmission or distribution is necessary. While there are aspects of electricity and heat demand profiles that need to be addressed to apply the SOFC plant to a particular building, this study only focuses on the production of these co-products. The SOFC plant could be used to baseload the electric demand for a building cluster, so the production would not be dependent on the demand profiles.

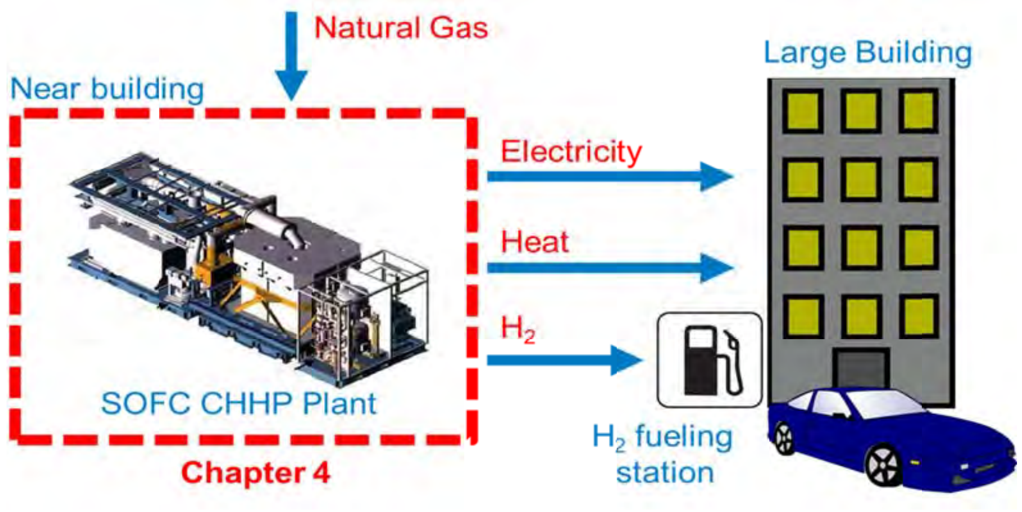

Figure 1.7 SOFC Co-generation plant with hydrogen production architecture

Although the SOFC system can be fueled by a renewable fuel such as SNG from the production plant in *Section 1.6.2*, it should be noted that a pathway from hydrogen to SNG and then back to hydrogen (and electricity and heat) is not an effective means of preserving the source energy (wind turbine electricity). The motivation behind this study is to *quantify* the costs of producing hydrogen regardless of the NG source, which closely matches the demand of a small FCV fleet, while co-producing electricity and heat in a high efficiency generator. Matching the FCV demand for hydrogen along with producing electricity and heat is a strategy for near-term market penetration of high efficiency distributed generation.

1.7 Prior Work

Several studies have analyzed alternative pathways to renewable fuels. Dean et al. [7] analyzed hybrid fuel (hydrogen) and electricity production plants using biomass gasification. The aim is to supply the shortfall of electricity generated by a wind farm with electricity from a biogas-fueled turbine and produce hydrogen if the wind farm meets the electricity demand. This enables the plant to produce the higher value product, either electricity or hydrogen, depending on the demand. Several variations of technology deployment were evaluated for hydrogen production in the hybrid plant, including purification processes and electrolysis. It was found that the direct processing and purification of biomass-derived syngas is a cost effective approach to hydrogen production at costs of 2.1 \$/kg-H_2 (1.9 \$/GGE, where GGE is the gallon of gasoline equivalent). The study considered the intermittency of wind resources and the geographical regions for which both wind power and biomass availability coincide. This scenario is consistent with a hydrogen economy, for which electricity is supplied by biomass or wind, and hydrogen fuel is produced for the transportation market.

Gassner et al. [8] analyzed a hybrid SNG production plant from the gasification of wood (biomass). The gasified wood gas stream did not have sufficient hydrogen for full conversion to SNG (mostly methane), so an electrolysis process was used to produce the make-up hydrogen. Electricity was produced internally using heat from the exothermic methanation reaction to drive a steam rankine cycle. This is a unique hybrid system using multiple technologies, and the integration of the electrolyzer resulted in improved performance and reduced carbon emissions for SNG production. Overall plant energy efficiencies of biomass to SNG ranged from 70-80% HHV. The SNG production cost ranged from 24-42 \$/MMBTU (2.9-5.1 \$/GGE).

Larson et al. [9] conducted analysis on producing multiple fuels from biomass gasification, including Fischer-Tropsch liquid fuels, dimethyl ether, and hydrogen. In addition to these fuels, electricity co-production using syngas produced from the gasification was also analyzed. The fuels production cost from this analysis depends highly on the biomass feedstock cost and the price at which electricity can be sold. The economic analysis resulted in fuel costs in the range of 15-25 \$/GJ (2.0-3.3 \$/GGE).

Carbon dioxide capture from these fuels production plants was analyzed, and this represents a scenario where renewable carbon dioxide could by re-used in the two synthetic fuels production plants described in *Section 1.6.1*. Since the fuel source for the fuel production plants in Larson et al. [9] is biomass, the cycle is carbon neutral. This analysis was done for very large production scales (~1000 MW) to benefit from economy of scale; while this size plant is achievable for biomass in limited areas, smaller scale production plants are more relevant for renewable energy sources that integrate wind or solar.

Graves et al. [10] presents technologies and processes for various renewable, non-biological pathways to liquid fuels. Recycling carbon dioxide is also discussed in relation to producing hydrocarbon fuels such as gasoline and diesel. Electrochemical, thermochemical, and photochemical methods were considered for the dissociation of water and carbon dioxide into syngas (hydrogen and carbon monoxide). The screening study for syngas production technologies resulted in high temperature co-electrolysis as the most promising method based on its efficient conversion of electricity and heat, high reaction rates, and direct production of syngas. Fischer-Tropsch synthesis was chosen for the conversion of syngas to liquid fuels. The resulting production cost range for gasoline and diesel fuel is 2-10 $/GGE, and the actual value depends highly on the cost of electricity and intermittency of the electricity source (e.g. wind turbines). The investigated sources for carbon dioxide included capture from biomass and fossil power plants, and direct capture from the air using various sorbent technologies. Direct carbon dioxide capture from the air offers another carbon-neutral cycle for liquid fuels production; this method was not considered for the source of carbon dioxide in this thesis.

Colella et al. [11] analyzed the polygeneration of hydrogen, heat and power from an SOFC system, and several advantages for generating hydrogen in this way were highlighted: controlling the production of hydrogen to meet the demand (otherwise produce more heat), kick-start the availability of hydrogen to promote the production FCVs without the supply and demand gap from centralized, large-scale hydrogen production plants, and generate hydrogen with less carbon emissions than conventional methane reforming. Hydrogen production control is obtained by changing the amount of the SOFC effluent that enters the hydrogen separation unit, by which the amount of combustible fuel that goes to heat recovery also changes. This control allows for decreased hydrogen storage requirements, which are energy and cost intensive. The production cost of hydrogen was not analyzed by Colella et al. [11]. By producing smaller amounts of hydrogen on-demand, there is potential for deployment FCVs while not over-supplying the near-term hydrogen demand.

1.7.1 Conclusions Drawn from Prior Work

The previously reviewed studies from the literature demonstrate the wide range of pathways and processes which are currently being considered to produce fuels from various renewable energy resources. While there are similarities between studies from the literature and the processes explored in this thesis, the research presented in this thesis includes the most detailed modeling and analysis of the three fuel production pathways, and there are unique processes for each pathway which are evaluated. The SNG production plant presented in Chapter 2 analyzes the electricity pathway (first to hydrogen), as opposed to the biomass pathway from Gassner et al. [8], to SNG. An SNG production plant from the hydrogenation of carbon dioxide has not been modeled previously.

The heuristic analysis from Graves et al. [10] of using renewably powered co-electrolysis with Fischer-Tropsch synthesis is a similar pathway to the study explored in Chapter 3, but no actual model to account for process efficiencies and subsystem synergies were made in Graves et al. [10]. A detailed thermochemical and economic analysis is given in this thesis for Fischer-Tropsch liquid fuel production from renewably powered co-electrolysis. The work of Colella et al. [11] is a similar analysis for hydrogen production using polygeneration from fuel cells, but other technologies for hydrogen separation are explored in Chapter 4 to increase hydrogen production efficiency; the production costs of hydrogen are also determined in the present study.

For each fuel production pathway explored in this thesis, many other literature sources are referenced for component-level modeling to achieve a well-designed system. This thesis contributes to the progress of pathway exploration by conducting detailed design modeling, process simulation, and economic analysis for three fuel production plants for which no previous studies have accomplished.

1.8 Modeling and Simulation Methodology

The modeling and simulation of the fuel production plants are carried out using Aspen Plus™ software, which is a thermochemical process simulator. Thermodynamic performance parameters and chemical reactions are specified by user input or predicted from thermodynamic and reaction chemistry solvers in the software. Using this simulation tool, all of the technologies from the fuel production plants were able to be modeled using performance estimation from literature, industry, and academic sources.

The fuel production cost was determined by using the H2A life cycle cost analysis tool developed by the National Renewable Energy Laboratory to calculate levelized cost of hydrogen production from various pathways. The production costs of other fuel products (e.g. SNG, gasoline, and diesel) from the pathways explored in this thesis are determined using this software. A detailed description of the parameters (capital investment, O&M, etc.) used to determine the levelized cost of fuel is given for each study.

1.9 Thesis Outline

This thesis presents the design, performance, and economic analysis of three fuel production plants. Chapter 2 presents an SNG production plant from renewable hydrogen and recycled carbon dioxide. Chapter 3 presents a gasoline and diesel fuels production plant which employs high temperature co-electrolysis and Fischer-Tropsch synthesis. Chapter 4 presents small-scale hydrogen production from a natural gas fueled SOFC CHHP polygeneration plant.

In each of these three chapters, a summary of relevant work from the literature is first given. Next, in-depth analysis of the major technologies associated with each plant is presented. The model of supporting plant processes is then explained to justify the chosen overall system design. The thermochemical performance of each plant is described with a discussion of the results. A life cycle cost analysis is then presented to determine the cost of fuel production.

Chapter 5 will summarize and compare the results from the three fuel production plants, including a high level analysis of TD&F costs to compare relative advantages of the presented pathways to central hydrogen production. Chapter 6 includes a discussion of the results and implications of the viability of these pathways, and suggestions are made for future research opportunities.

CHAPTER 2

SYNTHETIC NATURAL GAS PRODUCTION PLANT

The natural gas distribution infrastructure is well developed, enabling the fuel to be transported long distances via pipelines and easily delivered throughout cities. Using the existing pipeline to transport renewably generated synthetic natural gas (SNG) can leverage the value of the product. This study aims to develop a plant design and evaluate the performance and economics of producing SNG by reacting renewably generated hydrogen with carbon dioxide. The carbon dioxide feedstock is assumed to be captured and scrubbed from an existing coal fired power plant at the city-gate, where the SNG plant is co-located. The economic analysis includes a sensitivity analysis of SNG production cost on the hydrogen feedstock cost and operating capacity factor. No large-scale carbon dioxide methanation plants have been modeled at present, and this study aims to characterize the performance and economics of SNG production from a renewable hydrogen pathway.

This chapter will present previous work in SNG production, followed by a description of the methanation process with equilibrium and kinetic (from literature) considerations. The methanation reaction analysis is used for the design of a large-scale fixed bed reactor with cooling. The process of the plant, including feedstock clean-up, reactor design, process integration, and chemical separation processes will be discussed. A discussion of the process simulation results and an economic analysis is then given.

2.1 History

Methanation has been a common practice for eliminating carbon monoxide and carbon dioxide in various chemical processes such as ammonia production and natural gas purification; for these processes, only small amounts (1-3% molar basis) of carbon oxides need to be converted to methane. A “bulk” methanation process is unique due to the high concentration of carbon oxides and hydrogen. In addition, the carbon dioxide is the only carbon source, and the reaction characteristics of carbon dioxide are much different than carbon monoxide.

In the late 1970’s and early 1980’s, there was a strong effort for the production of methane from the gasification of coal [12]-[15]. Studies were conducted to determine the design of such a process, and much insight was gained about reactor conditions and the gas processing required for the production of SNG. The gasification of coal produces a syngas which is composed mainly of hydrogen and carbon monoxide. The methanation process was commonly designed using a series of adiabatic reactors, and the reactor temperature rise was controlled with the use of recycle and inter-stage cooling [15]. The predominant catalyst chosen for the methanation reactors was supported nickel due to its high activity, high selectivity to methane, and relatively low cost [16].

The Dakota Gasification Company operates a coal gasification plant at the Great Plains Synfuels Plant (GPSP) in North Dakota, where the main product is SNG [17]. Pelleted supported nickel catalyst is used in a packed bed reactor with inter-stage cooling to produce high pressure steam. It was found that the process operated well if sulfur was removed prior to the reactor due to the sensitivity of the catalyst to sulfur poisoning. Panek et al. [17] stated that carbon dioxide hydrogenated to methane in the reactor, but the reaction was not as complete as carbon monoxide hydrogenation.

While the technologies required for methanation are in commercial phase, including sulfur removal units, fixed bed reactors, carbon dioxide separation units, and the required balance of plant components, there is no demonstrated industrial-scale bulk methanation process which reacts large concentrations of carbon dioxide with hydrogen to produce SNG. Because of this, there is much uncertainty about carbon dioxide reactivity and selectivity to methane. There are many studies which aim to characterize the kinetics of carbon dioxide methanation on a laboratory scale, and their results give insight into the desired operating conditions of the process. The details of several literature sources on carbon dioxide methanation kinetics and a proposed multi-tubular fixed bed reactor design are given later in this chapter.

2.2 Methanation

The process of reacting one mole of carbon dioxide (CO_2) with four moles of hydrogen (H_2) over a catalyst is termed the Sabatier process of methanation described by Equation (2.1).

$$CO_2 + 4H_2 \leftrightarrow CH_4 + 2H_2O \qquad \Delta H_{Rxn} = -165\ kJ \tag{2.1}$$

The reaction produces one mole of methane (CH_4) and two moles of water (H_2O). The reaction is highly exothermic and the number of moles decreases as the reaction proceeds to the right (forward). The forward direction of the Sabatier reaction is favored at lower temperatures due to its exothermicity and high pressures due to its stoichiometric molar contraction.

2.2.1 Equilibrium

The thermodynamic equilibrium trends for the methanation reaction are important for preliminary consideration of reactor operating conditions. Figure 2.1 illustrates the temperature dependence of the equilibrium composition at atmospheric pressure with a stoichiometric feed of hydrogen and carbon dioxide (4 to 1). The equilibrium compositions were calculated from a Gibbs free energy minimization solver.

At low temperatures, the equilibrium concentration of CO_2 is very small, which corresponds to a high degree of the reaction proceeding in the forward direction. The CH_4 concentration decreases as the temperature increases, and CO forms at temperatures greater than 450 °C due to the reverse of the water gas shift (WGS) reaction, shown in Equation (2.2).

$$CO + H_2O \leftrightarrow H_2 + CO_2 \qquad \Delta H_{Rxn} = -41\ kJ \tag{2.2}$$

The trends in Figure 2.1 are due to the competing methanation and WGS reactions. The maximum in CO_2 concentration (at 550 °C), is indicative of the WGS reaction beginning to proceed in reverse (consuming CO_2) at a similar rate as the reverse of the methanation reaction (forming CO_2). As the temperature exceeds 600 °C, the reverse of the WGS reaction dominates, producing equal amounts of CO and H_2O, while consuming H_2 and CO_2.

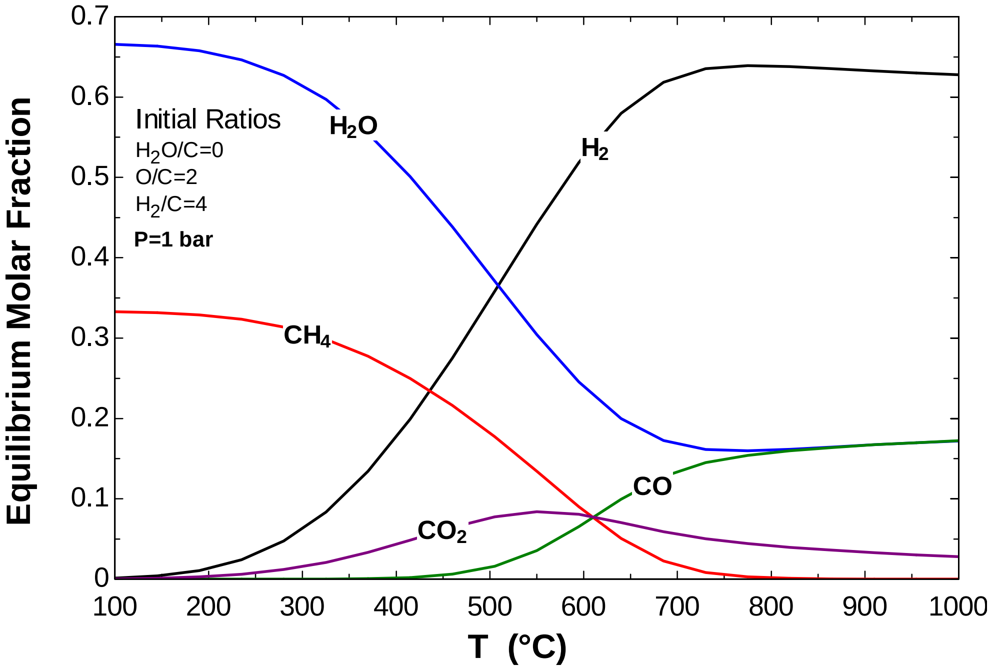

Figure 2.1 Temperature dependence of equilibrium molar composition at P=1atm and H_2:CO_2 feed ratio of 4:1

The pressure dependence on the CH_4 concentration can also be shown, as in Figure 2.2. The CH_4 concentration increases at higher pressure, but there is not significant increase in CH_4 concentration at pressures near 20 bar. The stoichiometric ratio for H_2:CO_2 of 4:1 results in the highest equilibrium concentration of CH_4. While similar amounts of CO_2 react to form CH_4 for a feed ratio of 4:1 and 5:1, the unreacted H_2 dilutes the concentration of the gas mixture, which lowers the concentration of CH_4.

Considering operation at high pressure, Figure 2.3 illustrates the temperature dependence of the equilibrium composition at 20 bar.

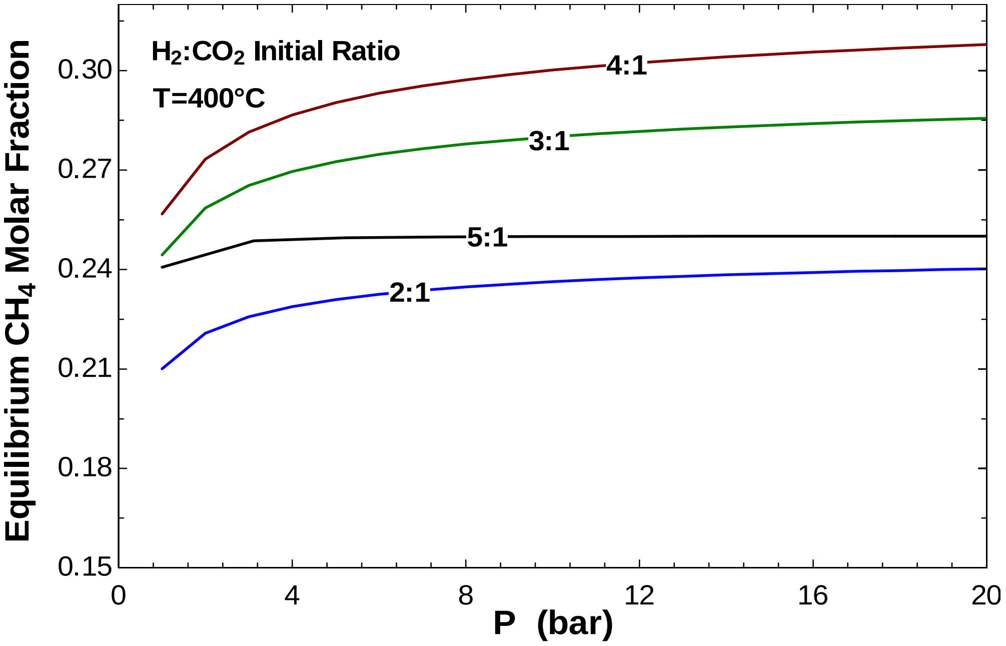

Figure 2.2 Pressure dependence of equilibrium CH_4 molar fraction at T=400 °C and various H_2:CO_2 feed ratios

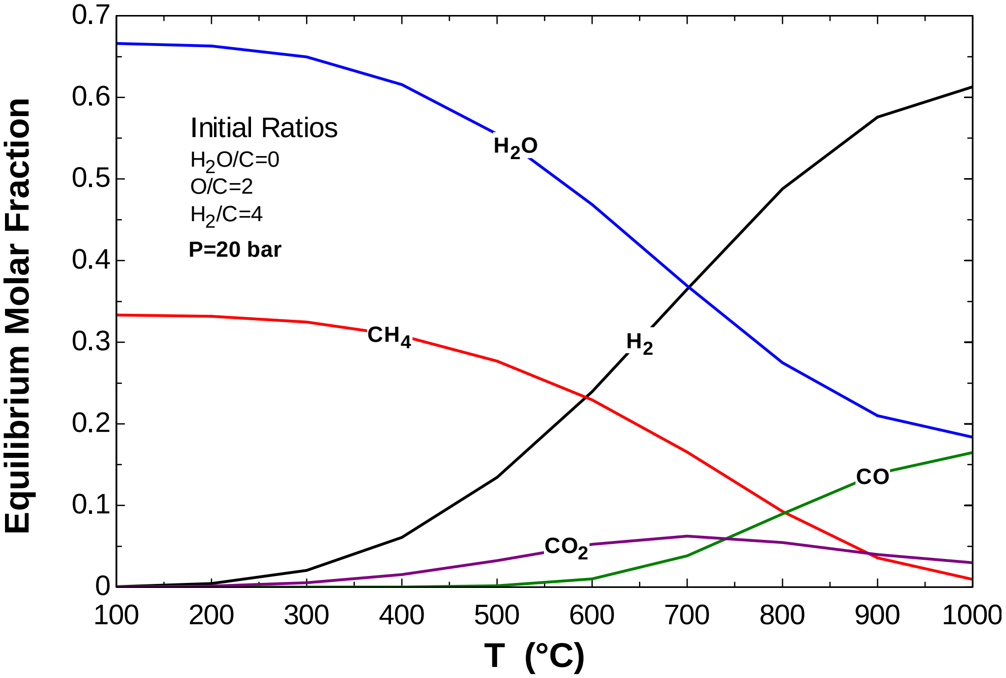

Figure 2.3 Temperature dependence of equilibrium molar composition at P=20 bar and H_2:CO_2 feed ratio of 4:1

At a pressure of 20 bar, there is only small decrease in CH_4 concentration operating at temperatures up to 400 °C. This is particularly beneficial for the kinetics of the catalytic reaction which are favored at temperatures of 300-400 °C, as will be discussed in the following section. The formation of CO does not occur until the temperature exceeds 550 °C (as opposed to 450 °C for atmospheric pressure).

2.2.2 Kinetics

The Sabatier reaction is thermodynamically favored, since the Gibbs free energy of the reaction is largely negative (-113.5 kJ). However, the reduction of carbon dioxide to methane requires a catalyst to promote the elemental steps of dissociation and formation required for the conversion [18]. The thermodynamic considerations are used while the necessary temperatures and pressures favorable for the reaction kinetics are determined. For supported nickel catalysts, activation requires temperatures of greater than 250 °C [19]. Catalysts suitable for methanation have high nickel content, and there is a temperature limit of around 600 °C to mitigate catalyst sintering [20]. For molar contracting reactions, such as methanation, high pressure is generally favorable for the reaction kinetics.

2.2.2.1 Rate Laws

Literature with experimental data is reviewed for the Sabatier reaction. Reaction rate laws for relevant feed concentrations of hydrogen and carbon dioxide were used to gain insight into conversion extents and limitations for appropriate reactor design parameters: geometry, catalyst loading, and cooling methods.

Two main forms of reaction rate equations are found in the literature and are discussed in this section: power law and Langmuir-Hinshelwood-Hougen-Watson (LHHW) models. Irreversible power law models based on partial pressure have the form of Equation (2.3).

$$r = k \prod_i P_i^{\nu_i} \tag{2.3}$$

$$k = Ae^{\left[\frac{-E_a}{RT}\right]} \tag{2.4}$$

In Equations (2.3) and (2.4), k is the rate constant, P_i is the partial pressure of species i, ν_i is the experimentally determined "order" with which the reaction depends on species i, A is the pre-exponential factor, E_a is the activation energy, and R is the universal gas constant. Irreversible rate laws with normal kinetics (positive reaction order with respect to the reactants) indicate that a reaction will proceed faster when operating at high temperatures and pressures. Other considerations such as catalyst activation temperature, catalyst sintering, and equilibrium must be made to ensure physical realization of these rate equations. Irreversible rate laws assume the condition of kinetic limitation of reaction extent (the equilibrium composition is not approached).

Chlang et al. [21] performed a kinetic study and derived an irreversible power law rate, shown in Equation (2.5).

$$r_{CH_4} = kP_{H_2}^{0.21}P_{CO_2}^{0.66} \tag{2.5}$$

The reactor temperature for the experiments ranged from 277 to 318 ^oC, and the reactor pressure ranged from 10.5 to 17 atm. The initial composition of carbon dioxide ranged from 17 to 33% with balanced hydrogen. The reaction was carried out over a differential tubular reactor with 58% nickel catalyst. The small operating temperature range carried out for this kinetic study limits the robustness of the rate equation. The reaction order is empirical (not based on certain reaction steps), as can be seen from the fractional powers for H_2 and CO_2 partial pressures. From Equation 2.5, it is implied that increasing the concentration of CO_2 has a larger effect on the reaction rate than increasing the concentration of H_2.

Saletore et al. [22] also derived an irreversible power law rate, shown in Equation (2.6).

$$r_{CH_4} = kP_{H_2}^{0.79}P_{CO_2}^{0.12}P_{H_2O}^{-0.62} \tag{2.6}$$

The rate constant k=0.725 gmol/(hr-gcat-atm$^{0.29}$) was shown to be independent of temperature if operated over 300 °C (the study operated at temperatures up to 400 °C. The reactor was operated at pressures up to 8 bar. The negative exponent for the water partial pressure indicates that water removal favors the kinetics of reaction. The validity of this reaction rate requires the following conditions: temperatures greater than 300 °C, high (> 10%) concentrations of CO_2, and large catalyst particles (>1.6mm diameter); it is apparent that these constraints on reactor conditions will be met by the reactor conditions in this study's SNG production plant. Contrary to Equation 2.5, Equation 2.6 indicates that the H_2 partial pressure has a greater effect on reaction rate than CO_2.

LHHW reaction rate models account for adsorption steps in the reaction mechanism which lowers the rate by a factor based on the adsorption (onto the catalyst) equilibrium limitations of the reacting species. The LHHW rates have the following form:

$$r = \frac{k\prod_i P_i^{\nu_i}}{\left[1 + \prod_i K_i P_i^{\nu_i}\right]^n} \tag{2.7}$$

K is the adsorption constant of species i. LHHW reaction rate laws inherently describe the reaction mechanism by describing the adsorption mechanism. The partial pressure terms in the denominator represent the species that go through adsorption steps in the reaction. These rate laws combine reaction mechanism theory with experimental fitting parameters such as the apparent activation energy (used to calculate *k*).

Seglin [16] presents a reversible LHHW rate law shown in Equation (2.8).

$$r_{CH_4} = \frac{C_1\left[P_{CO_2}P_{H_2}^2 - \dfrac{P_{CH_4}P_{H_2O}^2}{K_1 P_{H_2}^2}\right]}{\left[P_{H_2}^{1/2} + C_2 P_{CO_2} + C_3\right]^5} \tag{2.8}$$

C_1, C_2, and C_3 are experimentally determined parameters which are a function of temperature. The temperatures in this experimental study ranged from 260 to 399 ^{o}C, and the pressure was held constant at 1 bar. This rate equation infers that the adsorption of H_2 and CO_2 are limiting steps in the reaction. The reversible term in this rate equation indicates that the reaction can approach an equilibrium limited regime. The complexity of this equation along with the ambiguity of determining the temperature dependence from the reference makes it difficult to implement in an Aspen Plus™ kinetic reactor model for simulation. Also, the low pressure of operation could lead to invalid kinetic performance prediction when operating at elevated pressures.

Hoekman et al. [23] conducted an experimental study of the carbon dioxide methanation reaction in a tubular, packed-bed reactor. The study used a modern (2009), commercially available catalyst with a 20-25% nickel loading. The laboratory scale reactor was operated at various temperatures and feed compositions to determine the optimum operating conditions.

Hoekman et al. [23] found the highest carbon dioxide conversion, defined in Equation (2.9), of around 80% at H_2:CO_2 feed ratios of 6:1 (ratios tested were 2:1, 4:1, and 6:1). This operating point corresponded to a temperature of around 325 ^{o}C, as shown in Figure 2.4.

$$X_{CO_2} = \frac{CO_{2,in} - CO_{2,out}}{CO_{2,in}} \tag{2.9}$$

A near linear increase in conversion occurs at temperatures up to around 275 ^{o}C, and the maximum conversion was predicted at around 325 ^{o}C. The decline of conversion as temperatures exceed 325 °C was not explained, but this gives concern to operating the reactor temperature at excessively high temperatures. The proceeding of the reverse of the methanation reaction at higher temperatures could be the reason for this maximum.

The conversion efficiency, defined in Equation (2.10), was found to be the highest at the lowest tested H_2:CO_2 ratio of 2:1, meaning the reactor proportionally converted the most carbon dioxide relative to the hydrogen feed (Figure 2.5).

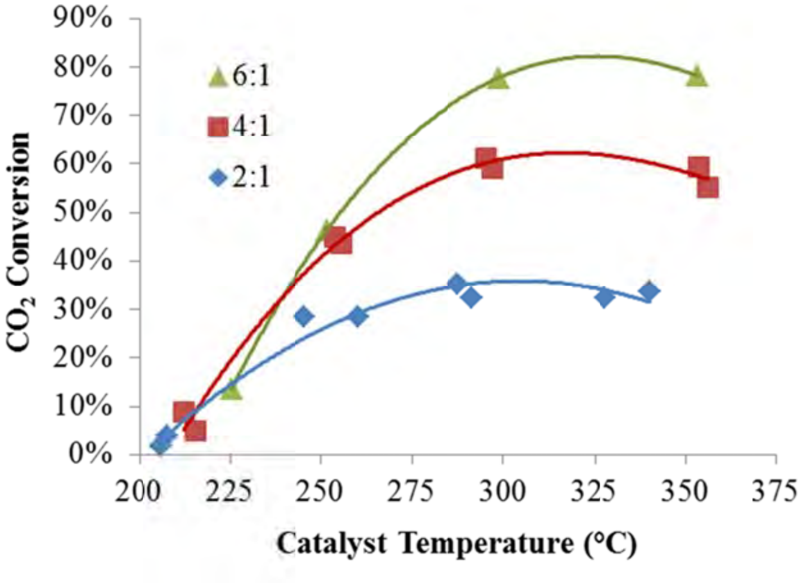

Figure 2.4 CO_2 conversion dependence on catalyst temperature; experimental data (symbols) from Hoekman et al. [23]

$$X_{efficiency} = \frac{CO_{2,in} - CO_{2,out}}{H_{2,in}} \tag{2.10}$$

The results suggest that the optimum molar ratio of hydrogen to carbon dioxide depends on the overall system process. If hydrogen is the limiting and most valued reactant, and there is no recycle employed, then the highest efficiency for each reactor pass is desired (H_2:CO_2 of 2:1). With a series of reactors and recycle employed, there is a trade-off between per pass conversion and the penalties for a separation process and recycle compression energy. There are limitations on acceptable levels of carbon dioxide and hydrogen in the delivered SNG product which are considered for these decisions.

The size of the reactor and amount of catalyst required for a certain conversion of carbon dioxide can be measured by the space velocity, which is the inverse of the residence time. The space velocity defines the amount of reactor volumes of reacting gas that can be treated per hour (expressed in units of hr^{-1}). As the space velocity increases, the residence time of the reactant molecules on the catalyst decreases, and it is expected that the conversion will consequently decrease. The effect of space velocity was experimentally determined from Hoekman et al. [23] at the operating condition of 300 °C with an H_2:CO_2 of 4:1, as shown in Figure 2.6.

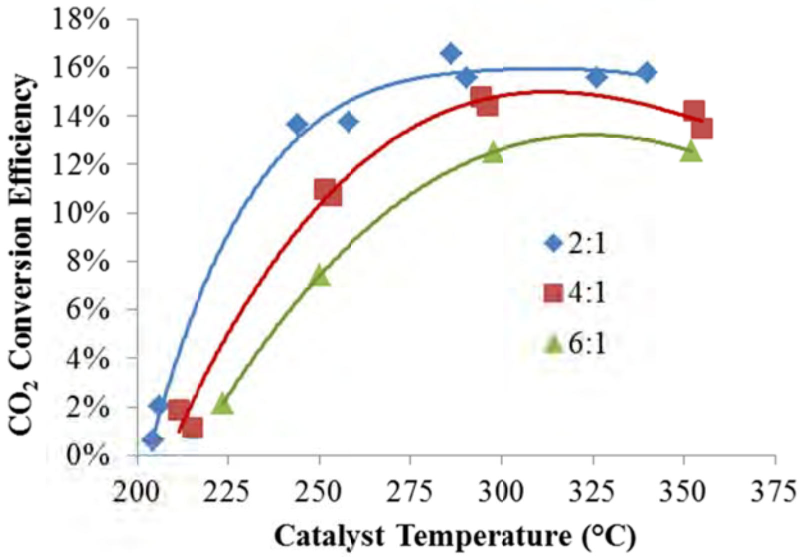

Figure 2.5 CO_2 conversion efficiency dependence on catalyst temperature for various H_2:CO_2 feed ratios; data from Hoekman et al. [23]

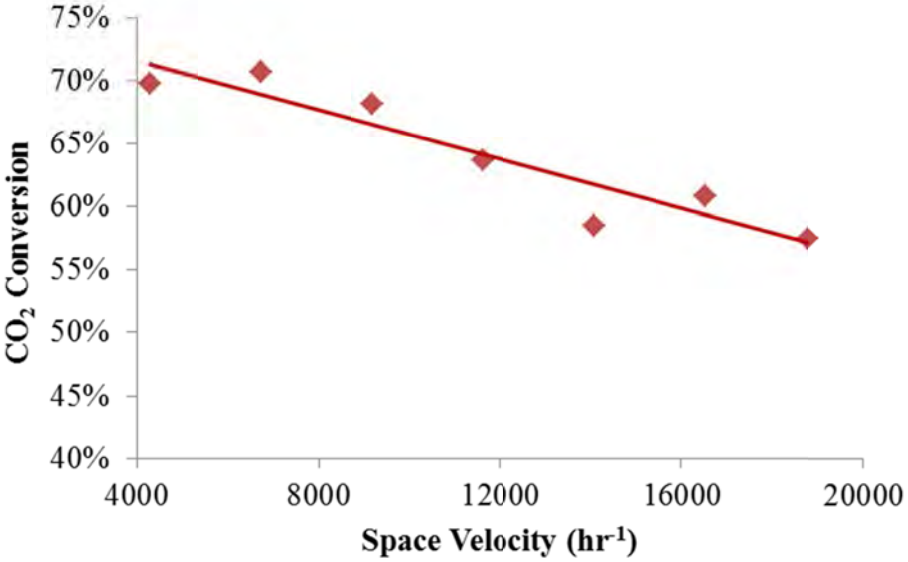

Figure 2.6 CO_2 conversion dependence on space velocity for a H_2:CO_2 feed ratio of 4:1; experimental data from Hoekman et al. [23]

The CO_2 conversion has a negative linear correlation with space velocity. Space velocity variations from 4000-18000 hr^{-1} result in conversions of 70-55%. This implies a trade-off between reactor capital and catalyst costs (high for low space velocities) and the desired per pass conversion (low for high space velocities).

2.2.2.2 Effects of Carbon dioxide, Carbon Monoxide, and Water Concentrations

Habazaki et al. [24] explored the relational effects of carbon dioxide and carbon monoxide in the methanation reaction. It was found that carbon monoxide preferentially hydrogenates before the carbon dioxide when both are present in the reactor. This suggests stronger adsorption of carbon monoxide than carbon dioxide on the catalyst surface. Compared to feeding carbon monoxide alone, the carbon monoxide methanation reaction increased when carbon dioxide was present in the feed. This was hypothesized to be due to resistance of carbon deposition because excess oxygen is present. There have been several studies confirming that carbon monoxide will inhibit carbon dioxide methanation until the carbon monoxide concentration is near equilibrium levels (e.g. Weatherbee et al. [26]). This supports the conclusion that negligible carbon monoxide will be present in the reactor effluent gas.

Habazaki et al. [24] also looked at the effect of water removal on the conversion of carbon dioxide to methane. By removing water in between reactor stages, the conversion of carbon dioxide increased drastically. Water removal effectively drives the water gas shift reaction (Equation (2.2)) to the left, so more carbon monoxide will form and subsequently hydrogenate to methane.

2.2.3 Methanation Reaction Conclusions

The variability in these kinetic studies on bulk methanation of carbon dioxide demonstrates the uncertainty for large scale reactor design. While the required catalyst volume and weight for a certain conversion can be determined from rate laws, the distribution of the catalyst in the reactor and the amount of time that the reactants “see” the active catalyst are determining factors for reactor design. The rate equations from

Section 2.2.2.1 can be used to calculate the required catalyst volume from a given inlet flow rate, composition, and conversion using Equation (2.11).

$$V_{cat} = \frac{F_{io}}{\rho_{cat}} \int_0^X \frac{dX}{-r_i} \tag{2.11}$$

V_{cat} is the required catalyst volume (m^3), F_{io} is the molar flow rate (mol/s) of the reacting species i, ρ_{cat} is the bulk catalyst density (kg/m^3), X is the specified conversion of species i, and r_i is the reaction rate (mol/s-kgcat) for species i. It is found that the resulting catalyst volume calculations from the rate equations differed greatly, and they underestimate the catalyst requirement in comparison to space velocity suggestions by Hoekman et al. [23], from which the reactor can also be sized using Equation (2.12).

$$SV = \frac{V_{rctr}}{\upsilon} \tag{2.12}$$

The volume of the reactor is calculated using υ, the standard volumetric flow rate of the feed gas (Sm^3/s), and SV (hr^{-1}), the chosen space velocity. As an example calculation, a volumetric flow of 7 Sm^3/s (similar to the flow rate for a methanation reactor in this study) and a chosen space velocity of 10,000 hr^{-1} results in a reactor volume of 2.5 m^3.

The author suggests that the rate equations given in *Section* 2.2.2.1 overestimate the rate of reaction, and the study from Hoekman et al. [23] is more reliable due to the modern experimental setup and commercial catalyst used. The underestimation of catalyst weight may have resulted from the ambiguity (and non-disclosure) of the catalyst support geometry (nickel distribution, effective surface area, etc.) from the kinetic studies in the literature and modern commercial nickel catalysts.

The rate equations given in this section are used to explore the possible reaction profiles in the reactor which is necessary to determine appropriate cooling methods. The kinetic based profile gives insight into the “hot spots” by identifying possible maximum temperature gradients in certain locations of the reactor. The Hoekman et al. [23] methanation study employing a modern commercial catalyst is used to estimate the conversion of carbon dioxide based on the feed gas composition and flow rate; the suggested space velocity required to accomplish the conversion is used for reactor sizing.

2.3 Methanation Reactor Design

The exothermic nature of bulk methanation is a concern for large-scale reactor temperature increase, and the design of reactor with cooling has multiple advantages over adiabatic reactors. While isothermal tubular reactors are nearly impossible to achieve in practice, cooling can be used to limit the temperature rise. One of the main considerations for the extent of the reaction is the temperature at which the catalyst is activated to achieve optimum kinetics. Governed by the catalyst type and the incorporation of the catalyst within the reactor bed, the temperature which maximizes the activity of the catalyst would be held constant in an isothermal reactor. The amount of reactor stages and catalyst required decreases when internal cooling is employed due to the increased allowable extent of reaction; this alleviates the concern of heating the reactor to temperatures which would sinter and deactivate the catalyst, while maintaining a temperature high enough for desired catalyst activation.

Another consequence of high temperatures is catalyst poisoning due to carbon deposition (coking). The latter concern is not as critical as sintering in this study because of the high oxygen content from carbon dioxide. Aspen Plus™ calculates the thermodynamic equilibrium for carbon deposition, and it is found to be negligible for the reactor conditions in this study (e.g. an atom composition of 7% C, 82% H, 11% O and temperatures of 250-400 °C).

A reactor design similar to a shell and tube heat exchanger, as shown in Figure 2.7, can be used to limit the temperature rise; the catalyst is packed in the tube side, while water flows through the shell to provide cooling. A co-flow arrangement is suitable for this design because the reaction is assumed to activate near the front of the reactor, and this allows for the largest temperature difference at that point.

The catalyst for the bulk methanation reaction was chosen based on the literature to have high nickel content. One potential catalyst, SNG1000, was suggested by an industry source [27] and has a composition of 56.6% Ni-6%MnO-5%Si-21%Al. The high nickel content is beneficial for the conversion of high concentrations of carbon dioxide in the reactant gas stream. The calculated volume for the catalyst in Equation 2.12 is the tube volume for the shell and tube heat exchanger.

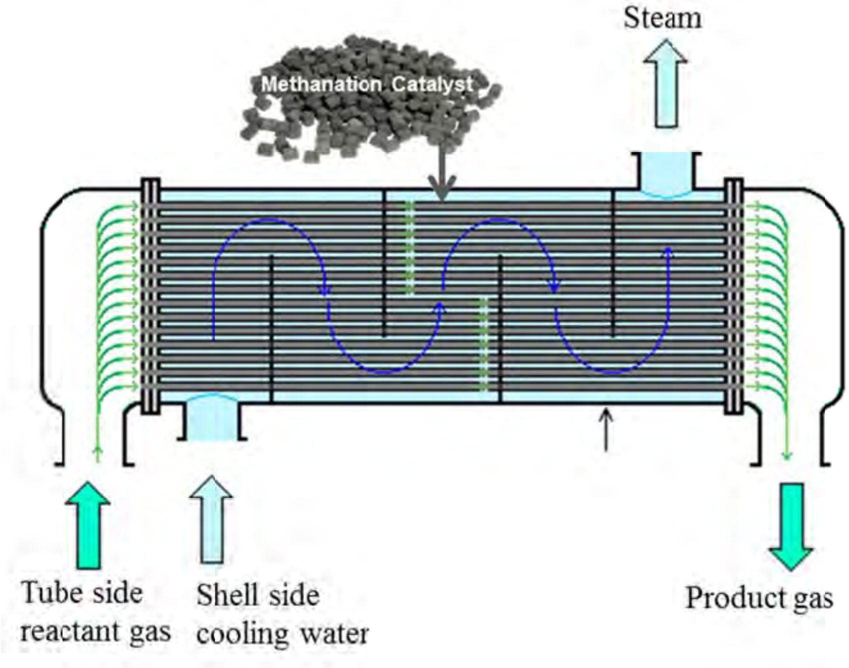

Figure 2.7 Reactor design concept: catalyst packed tubes in a shell and tube heat exchanger

While there are conflicting requirements for heat transfer area and reactor volume (determined by the space velocity) for the process gas, a reasonable approximation to satisfy both design parameters can be made. The packed bed tubes have unique heat transfer properties due to the two-phases of the reacting gases and the solid catalyst particles. Heat transfer phenomena include convection from the gas to the catalyst and the wall, and conduction between the catalyst particles and to the wall (radiation was neglected for simplification). The effective heat transfer coefficient is modeled differently depending on whether the bulk temperature inside a plug in the tube can be considered constant or variable with respect to the two phases. It is shown from Borkink et al. [28] that the temperatures of the packed particles and the surrounding fluid temperature are very similar for small tube diameters (less than 5 cm). Therefore, a homogenous model can be implemented to determine the heat transfer parameters of the tube and external coolant.

To determine the overall heat transfer coefficient, the conduction from the packed bed tube, along with a wall heat transfer coefficient, must be determined. Equations (2.13) through (2.15) [28] give heat transfer properties for a packed bed with alumina cylinder catalyst particles with effective diameter of 6 mm.

$$\lambda_r^* = \lambda_o^* + \frac{Pe_p}{Bo_{h,r}^{\infty}} \tag{2.13}$$

$$h_w^* = A_0 + aPe_p \tag{2.14}$$

$$\frac{1}{U_{ov}^*} = \frac{1}{h_w^*} + \frac{N}{\beta \lambda_r^*} \tag{2.15}$$

In Equations (2.13)-(2.15), λ_r^* is the dimensionless effective radial heat conductivity, λ_o^* is the dimensionless effective heat conductivity of the packed bed with a stagnant fluid, Pe_p is the molecular Peclet number based on the superficial velocity of the gas, $Bo_{h,r}^{\infty}$ is the Bodenstein number for heat at fully developed turbulent flow, h_w^* is the dimensionless wall heat transfer coefficient, A_0 and a are fitting parameters determined for the specified catalyst, β is a “lumped factor” determined to be 7.4, and N is the number of catalyst particles that can span the diameter of the tube. For the reactor conditions in this model, the resulting overall heat transfer coefficient is calculated to be 413 W/m^{2}K, and this value is used for catalyst packed tube-side reactor heat transfer coefficient.

For the reactor design, the kinetic reaction profile from the reaction rate found in Saletore et al. [22] is used based on its similarity in experimental reactor conditions to this study and because it captures the negative effect of water partial pressure on the reaction as was shown in Habazaki et al. [24]. The chosen space velocity, heat transfer coefficient, and maximum temperature specification will be used in Aspen Plus™ to design a shell and tube reactor for the methanation reaction. The dimensions and performance results of the methanation reactor are given in the next section based on the simulation results.

2.4 Supporting Plant Processes

The SNG production plant is modeled using Aspen Plus™ software, which simulates and integrates chemical reactors and balance of plant components (heat exchangers, compressors, pumps, etc.) from user defined performance specifications.

The key aspects of the plant are as follows:

- Carbon dioxide clean-up
- Methanation reactor stages (3)
  - Heat recovery between reactor stages with organic rankine cycle units and water condensing and purge
- Bulk gas, carbon dioxide, and hydrogen separation and recycle

Figure 2.8 illustrates the process flow for the SNG production plant. Three reactor stages are chosen for several reasons: i) multiple stages enable the purging of water which drives the reverse of the WGS reaction, ii) two or less reactors required excessive bulk recycle and over-strained the ability of the separation processes to limit the content of CO_2 in the product SNG, and iii) three (versus four or more) stages achieved a high enough overall conversion of CO_2 and H_2 to CH_4 while mitigating excessive capital costs for the reactor stage components.

2.4.1 Feedstock & Carbon Dioxide Clean-up

The size of the plant is based on an estimate of hydrogen that could potentially be produced from a large wind-powered electrolyzer at 40,000 kg/day. The hydrogen is fed into the plant at 20 bar, and it is assumed to be 100% pure. The feedstock streams are assumed to be transported to the SNG plant at a pressure higher than 20 bar, so no additional pressurization is required.

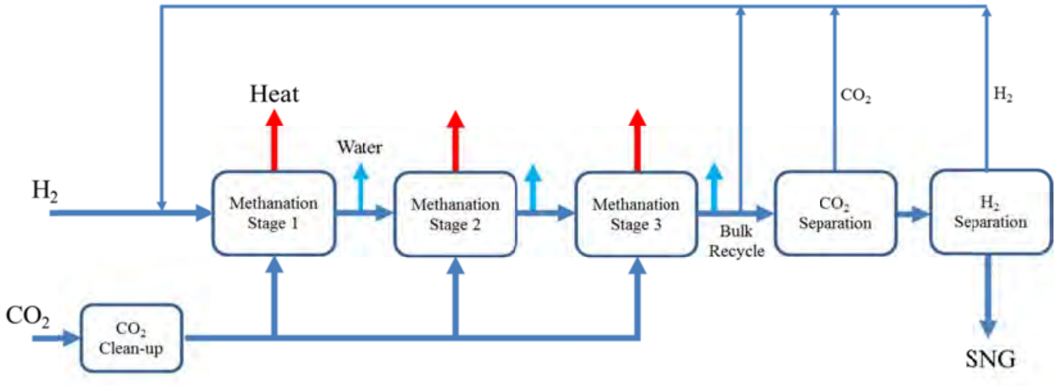

Figure 2.8 SNG production plant process flow diagram

The methanation reactor pressure of 20 bar is chosen based on the thermodynamic and kinetic favorability of the methanation reaction. The plant feed of CO_2 is chosen to be consistent with the 4:1 H_2:CO_2 molar ratio from the stoichiometry of the reaction; the resulting CO_2 feedstock amounts to about 80,000 tonne/yr which is equivalent to roughly 2% of the CO_2 produced from a 500 MW coal-fired power plant. The CO_2 is distributed to each reactor such that an H_2:CO_2 molar ratio of higher than 4:1 is maintained, as suggested by Hoekman et al. [23] for high conversion.

Many carbon dioxide capturing technologies simultaneously capture sulfur molecules such as hydrogen sulfide (H_2S), and this must be scrubbed to less than 1 ppmv to avoid nickel catalyst poisoning. This scrubbing process is accomplished by simulating the LO-CAT™ liquid oxidation process, which removes the bulk of the H_2S down to 10 ppmv [29]; this process uses an iron catalytic solution to promote the oxidation of H_2S to produce elemental sulfur, as shown in Equation (2.16).

$$H_2S + O_2 \rightarrow S + H_2O \tag{2.16}$$

The elemental sulfur is separated out of the gas stream. The LO-CAT™ process cannot remove enough H_2S to mitigate nickel catalyst poisoning, so a Zinc Oxide (ZnO) bed is used to purify the CO_2 gas to under 1 ppmv [29]. Figure 2.9 illustrates the H_2S removal process for the CO_2 feedstock.

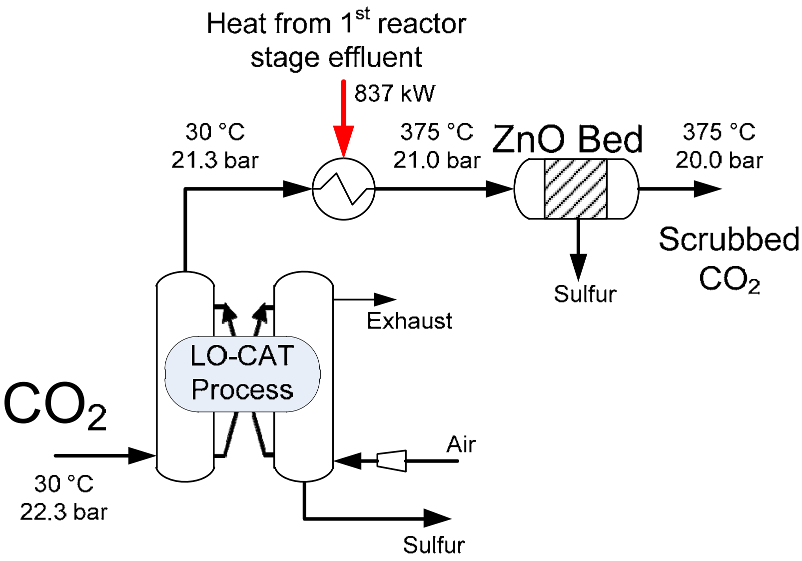

Figure 2.9 CO_2 feedstock clean-up: LO-CAT™ liquid oxidation followed by ZnO bed

Following the LO-CAT™ process, the gas must be heated to 375 °C for catalyst activation of the ZnO bed. This heating is supplied by the effluent of the first methanation reactor; the temperature of the first reactor effluent is 400 °C (350 °C for the other two reactors) to allow sufficient temperature difference for the ZnO bed feed gas heat exchanger. The ZnO bed is approximately isothermal due to the relatively small amount of H_2S removed.

2.4.2 Methanation Reactors

Based on the analysis of the methanation reaction and reactor design operation given in *Section* 2.2, the performance of each of the three methanation reactor stages is estimated. The first reactor has the highest reactant concentrations and pressure, and a carbon dioxide conversion of 80% is chosen. The second reactor has a slightly increased inert (methane) concentration and slightly decreased pressure (~17 bar, from upstream component pressure drops), so a carbon dioxide conversion of 70% is chosen. The third reactor has the greatest concentration of inert species and the lowest operating pressure (~14 bar), so a carbon dioxide conversion of 60% is chosen. These conversions are slightly more conservative than the findings in Hoekman et al. [23] based on the high hydrogen to carbon dioxide ratio (>6:1) and operating temperature of around 325 °C.

A detailed multi-tubular cooled plug flow reactor model based on the reaction rate from Saletore et al. [22] is simulated with the chosen reactor conditions and geometry requirements. The multi-tubular reactor sizing is used for more realistic cooling performance and cost analysis. The plug flow reactor geometry is designed to achieve the desired space velocity with a constraint on the tube diameter for adequate plug-flow assumptions. The heat transfer area is constrained by the volume and tube diameter requirements, but the co-flow coolant water flow rate through the shell is adjusted to accomplish the desired temperature control. Table 2.1 gives the design parameters for the first methanation reactor. The same process is used for each of the three reactors, and the resulting geometry is similar for all three.

Table 2.1 Methanation plug flow multi-tubular reactor design

	Value
Type	Shell-and-tube HX, 1 tube pass
Length	3 m
Inner Tube Diameter	0.05 m
Number of Tubes	424
Heat Transfer Area	200 m^2
Reaction Volume (inside tubes)	2.5 m^3

Coolant water is pressurized to 2.5 bar, enters the shell side at 50 °C, and boils for most of the length of the reactor at 130°C. The coolant flow is adjusted to provide cooling to the reactor such that the exit temperature of the process gas is 350 °C. This heated water can then be used for generating electricity via ORC units.

As seen from Figure 2.10, this reactor design and coolant flow enables the reaction to take place at a temperature of around 330 °C for the majority of the reactor length; this temperature approximately corresponds with the maximum conversion from which the reaction extent is based (Hoekman et al. [23]).

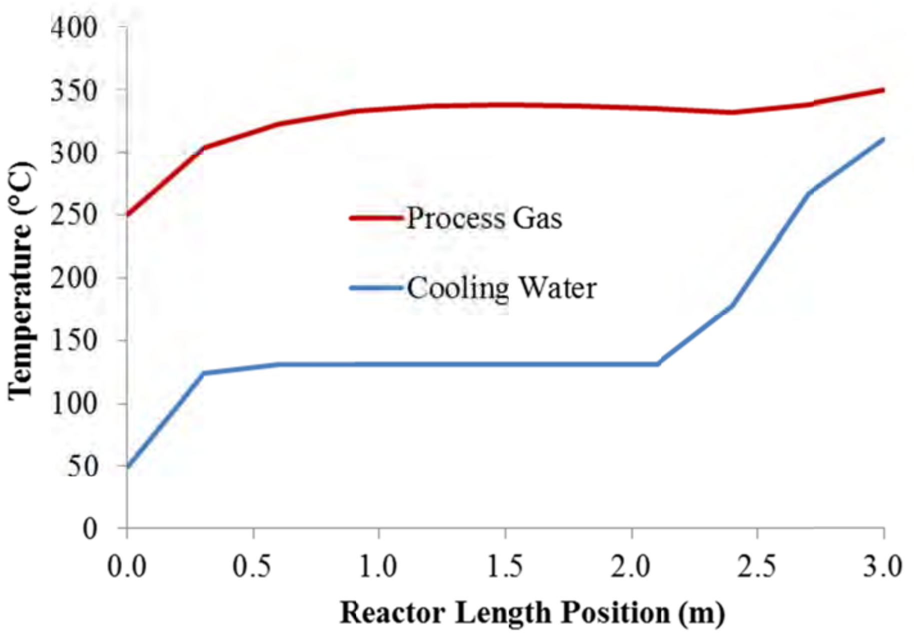

Figure 2.10 Temperature profile of methanation reactor process gas and coolant stream

2.4.3 Inter-stage Heat Recovery & Water Drain

The effluent of the methanation reactor is used in a gas to gas heat exchanger, which preheats the reactor feed gas stream. The feed-effluent heat exchanger heats the feed gas up to 250 °C for catalyst activation.

Figure 2.11 illustrates the second of three reactor stages with feed-effluent heat recuperation, heat recovery to an ORC unit, and water condensing. The temperature rise across the methanation reactor is limited to 100 °C by a coolant stream as described above. The hot effluent exchanges heat to the feed gas before supplying heat to a water loop for ORC power production. The gas exiting the ORC heat exchanger at 135 °C must be cooled down to 50 °C to condense and remove the water.

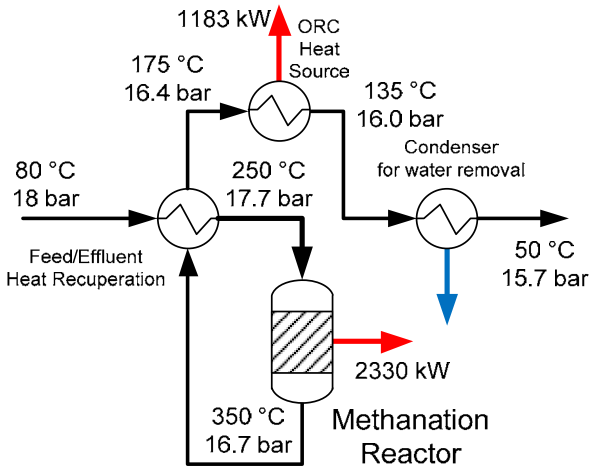

Figure 2.11 Methanation reactor stage with recuperation, heat recovery, and water condensing

The reactor effluent gases are hot enough to recover useful heat after recuperation to the feed gas stream. Utilization of an organic rankine cycle (ORC) is advantageous in this scenario because it requires only moderate temperatures for vaporization to produce electricity. The ORC water stream is heated to a temperature of 120 °C by the reactor effluent which is necessary for the operation of the ORC at an efficiency of 12% [30]. Each unit can produce 280 kWe, and the total recovered heat from the plant amounts to about 1010 kWe (supplies 82 kWe more than the required electricity for the plant). Figure 2.12 is the ORC flow diagram and the unit provided by Stone [30].

From the reaction mechanism, water removal favors the forward reaction to produce methane. Lower water content favors the reverse water gas shift reaction which enables the highly reactive carbon monoxide methanation reaction to take place. The condenser cooling source for removing the water out of the gas stream is a cooling tower water loop. The cooling tower also provides the cooling water for the ORC condenser. The water loss from the evaporative cooling is replaced with a water makeup source.

Heat exchanger coefficients are extrapolated from data in Peters et al. [31] for gas at pressure, liquid water, vaporization, and condensing. A pressure drop of 33 kPa across heat exchangers and 100 kPa across reactors is assumed throughout the process. These pressure drops represents a 1-1.5% pressure decrease for heat exchangers and 4-5% pressure decrease for reactors compared to the incoming gas stream pressure.

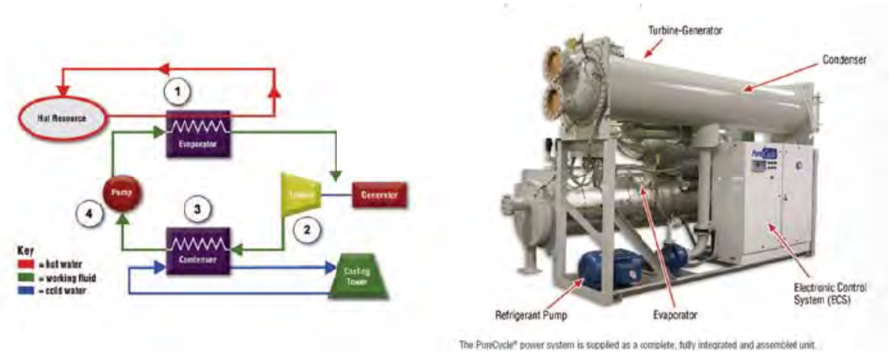

Figure 2.12 ORC unit from Stone [30]

2.4.4 Separation & Recycle

The product pipeline SNG must meet the energetic and compositional requirements set by the natural gas industry to be transported in the natural gas pipelines. The most stringent compositional requirement for this model is to achieve a product molar composition with less than 2% CO_2. The unconverted carbon dioxide must be separated and recycled to meet this requirement.

After the three methanation reactor stages, the product gases go through three recycle stages which are shown in Figure 2.13 and discussed in detail below:

- 40% bulk recycle (diverter)
- 90% CO_2 separation & recycle (MDEA absorption/stripping)
- 90% H_2 separation & recycle (polysolfone membrane)

2.4.4.1 Bulk Recycle

A bulk gas recycle of 40% is used to increase the overall reactant conversion. The extent to which the MDEA and hydrogen membrane units separate reactant species is limited, and the bulk recycle allows the plant to accomplish the required product gas composition while accounting for these limitations. The penalty for this recycle is mainly the compression of the recycle gas stream, including some of the desired product methane. This is the easiest separation process of the three, and it can be accomplished simply with a diverter valve.

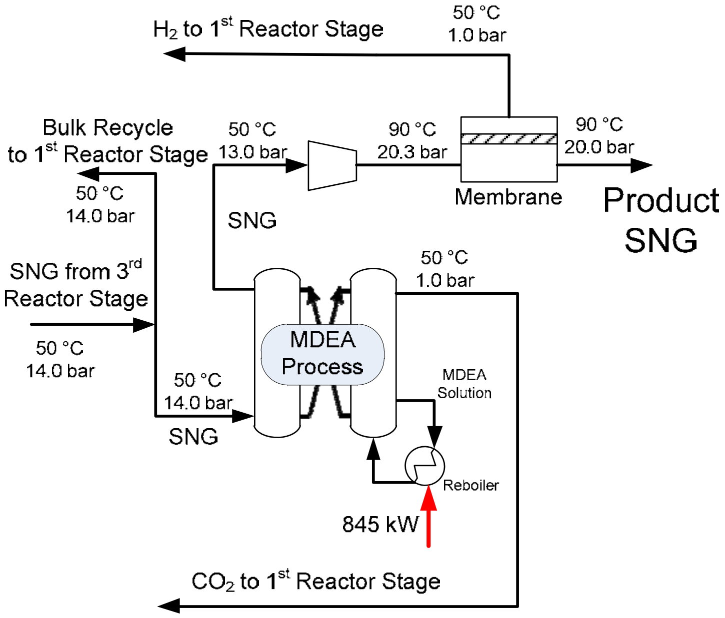

Figure 2.13 Bulk recycle, MDEA CO_2 separation and recycle, and polysolfone membrane H_2 separation and recycle

2.4.4.2 CO_2 Separation & Recycle

A process to remove CO_2 is necessary to control the amount of CO_2 in the product gas and increase its conversion to methane. In order to accomplish the separation and recycle of CO_2, processes from the literature and industry expert advice were evaluated. The chemical absorption process of Methyl diethanolamine (MDEA) was determined to be the best option for the model. It is a proven process with the ability to capture 90% of the CO_2 in a gas stream containing 15% CO_2 at relatively low pressures [33]. Additives such as Selexol make the MDEA solution more selective to CO_2 [34]. The main drawback to this process is the energy required for the regeneration of the MDEA in the CO_2 stripping column. The chemical reaction involved in the absorption of CO_2 into the MDEA is highly exothermic, so a significant amount of heat is required to reverse the reaction in the stripper (“reboiling”) [34].

A detailed analysis of an MDEA process for separating CO_2 and H_2S concludes a reboiler heat duty of 162 kJ/mol-CO_2 [34]. The resulting CO_2 separation process for the SNG plant amounts to a heat usage of about 850 kW, which is based on the modeled CO_2 separation rate of 90%. The temperature at which the reboiling process occurs is between 100-200 °C, and the quality of heat generated by the methanation reactor effluent gas (350 °C) is assumed to be sufficient for this process. There is also an electric power duty required for the absorbent circulation pumps, and this is supplied by the ORC-generated electricity.

2.4.4.3 H_2 Separation & Recycle

The gas must be removed of excess H_2 to maintain a high volumetric heating value and energy density for the product SNG. The molar percentage of H_2 in the CO_2-scrubbed gas stream is about 35%. This is well below the hydrogen composition of feed gas such as that from steam methane reforming (~75% hydrogen) used for many hydrogen separation processes. Pressure swing adsorption (PSA) is a common method for hydrogen separation, but the process becomes ineffective and uneconomical with less than 70% H_2 in the feed stream [29] because of the large amount of adsorbent area required to separate the non-hydrogen gas molecules.

Membrane technology for hydrogen separation is well established in industry, and it is especially suitable for scenarios in which the permeate does not require high purity [35]. While the separation process should aim to minimize the amount of product methane in the permeate stream, any additional separation of carbon dioxide from a membrane process would benefit the product composition. Although carbon monoxide is not considered a significant product of the methanation reaction in this study, a membrane separation process could also remove carbon monoxide from the product stream.

Another advantage of using a membrane for hydrogen separation is that the bulk of the product gas experiences minimal pressure drop (as opposed to a PSA process). In the model, the feed gas is pressurized slightly above the desired SNG product pressure (to account for a small pressure drop of the retenate), and no further compression is needed for the SNG product. The molar flux through a membrane is driven by the pressure difference of the separable molecule, i, as shown by Equation (2.17).

$$J_i = \frac{\rho_i \left(P_{i,feed} - P_{i,permeate}\right)}{\delta} \tag{2.17}$$

J_i is the molar flux (mol/m^2-s), ρ_i is the permeability constant (a function of the permeability of a certain molecule through a certain membrane), P_i is the partial pressure of molecule i in the feed and permeate gas streams, and δ is the thickness of the membrane. For a certain membrane, Equation (2.17) can be used to determine the size of the membrane required to achieve a rate of hydrogen flux. The relative amount of hydrogen separated along with methane and carbon dioxide is also a performance characteristic of the chosen membrane that must be accounted for to determine the selectivity to hydrogen (permeate purity).

The membrane performance can be approximated by the literature values for commercial hydrogen permeable membranes. Polysolfone-based membranes have been in use for years with proven durability, permeability, and selectivity [36]. The estimated normalized permeability constant of 100 (10^{-6} Scm^3/cm^2-s-cmHg) based on polysolfone membranes is used to determine the size of the membrane required to achieve a 90% hydrogen separation.

2.4.5 SNG Product

The SNG product composition achieved through sequential stages of reactant conversion and separation is shown in Figure 2.14.

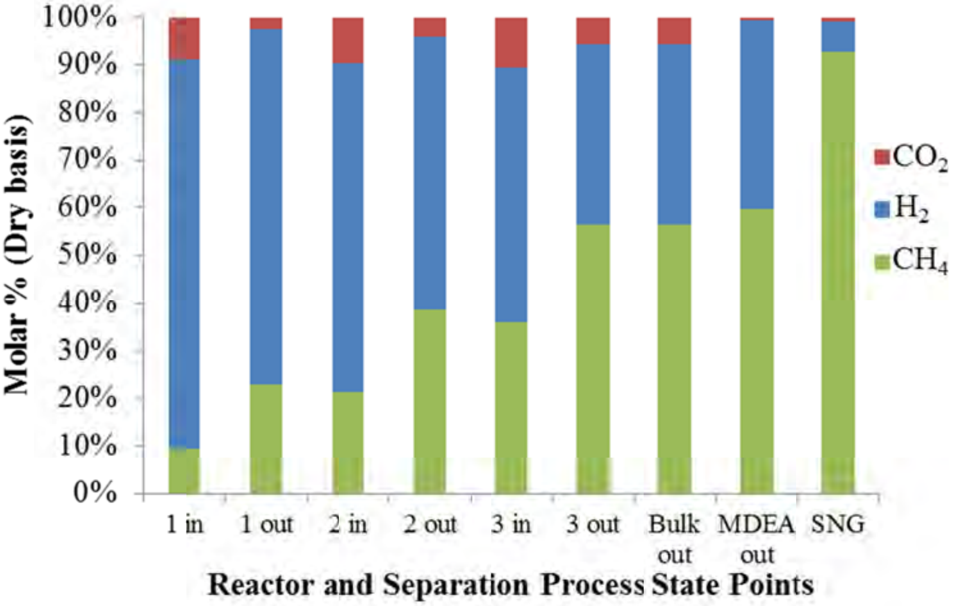

Figure 2.14 Molar gas composition at various reactor and recycle streams. Numbers indicate methanation reactor inlet and outlet streams.

The final gas composition is 92.7% CH_4, 6.3% H_2, and 1.0% CO_2. The SNG is produced at 20 bar for transport in the pipeline.

The heating value must be suitable for end-use applications. The heating value in the natural gas industry is quantified by the Wobbe index, shown in Equation (2.18).

$$Wobbe\ Index = \frac{HHV_{SNG}}{\sqrt{\frac{\rho_{SNG}}{\rho_{air}}}} \tag{2.18}$$

HHV_{SNG} is the higher heating value of the SNG, and ρ_{SNG} and ρ_{air} are the density of the product SNG and air respectively at STP. The importance of the Wobbe Index resides in the end-use standardization of burner units; for a given orifice size through which the gas mixture passes, gas mixtures with the same Wobbe Index will deliver the same amount of heat. The Wobbe index for the product SNG is calculated to be 47.5 MJ/Sm^3 which is slightly below the normal index of natural gas of around 48 MJ/Sm^3, but it is not low enough to significantly impact burning performance. The SNG is slightly lower in volumetric energy density based on the Wobbe Index because of the low volumetric energy density of hydrogen, and natural gas typically contains up to 10% ethane (C_2H_6), 5% propane (C_3H_8), 2% butane (C_4H_{10}), and 0.5% pentane or heavier (C_{5+}) by volume [32]; these heavier hydrocarbons increase the volumetric heating value of the natural gas. On a weight basis the heating value of the SNG is higher than typical natural gas streams (54.6 MJ/kg versus 52.2 MJ/kg).

Studies have been conducted on issues concerning hydrogen mixing with natural gas (e.g., Haeseldockx et al. [37]). Potential problems associated with having a partial amount of H_2 in the SNG composition have been evaluated and deemed acceptable with H_2 concentrations up to 17%. Pipeline embrittlement caused by H_2 is an issue that requires further intensive study to evaluate the long term effects on the pipeline material. Leakage issues are negligible with the predominant use of polyethylene pipelines in the existing infrastructure [37]. Although the physical limitations for H_2 in the pipelines is 17%, natural gas companies will allow less than this due to heating value requirements and safety standards. The 6% H_2 composition was determined to be acceptable for heating value and pipeline transport quality [38].

2.5 System Design

Figure 2.16 illustrates the system design. The H_2 feed is assumed to be piped into the plant, and CO_2 is delivered locally from a power plant or piped from an existing pipeline. Both feedstock molecules are assumed to be pressurized such that no additional compression is necessary to achieve a pressure of 20 bar.

The CO_2 goes through a purification stage at state-point (1) before being distributed to each reactor. Three reactor stages are chosen which start at state-point (8), (15) and (21); separate reactor stages allow for water condensing (e.g. Condenser 1) and purge after heat recovery. The recovered heat from the methanation reactor and effluent gas stream drives an organic rankine cycle (e.g. ORC 1) for power generation. Not shown in this diagram, a cooling tower is modeled to supply the cooling for the condensers, the ORC heat sink, and compressor intercooling.

After three stages of methanation reactors, 40% of the gas at state-point (26) is recycled (Bulk Recycle). The CO_2 from the remaining gas stream at state-point (29) is then separated with an amine (MDEA) absorption process and fed back to the first methanation reactor stage. The remaining gas stream at state-point (35) is compressed to 20 bar (to make up for pressure drops in the system) before being fed into a hydrogen permeable membrane process for separation and recycle. The retenate of the membrane process (state-point (40)) contains the final product SNG for pipeline transport.

2.6 SNG Plant Performance Results

The following is the overall power and material flow of the SNG production plant:

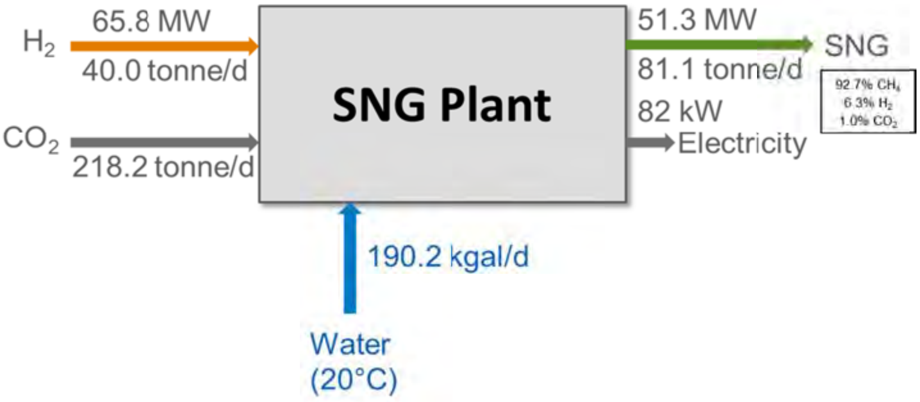

Figure 2.15 Methanation plant input/output summary (HHV basis)

The overall plant efficiency on an HHV basis is calculated from Equation (2.19) to be 78.0% HHV. The plant loses 22.0% of the heating content of the hydrogen by the conversion to SNG.

$$\eta_{plant} = \frac{HHV_{SNG} + \dot{W}_{elect}}{HHV_{H_2}} = 78.0\% \tag{2.19}$$

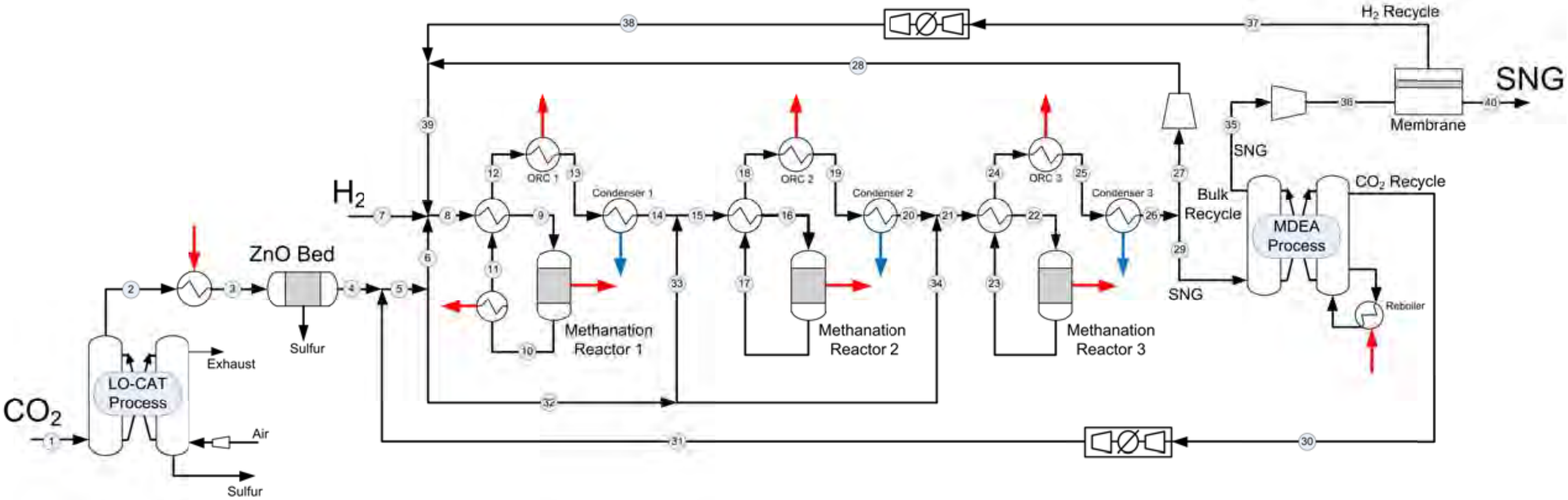

	1	2	3	4	5	6	7	8	9	10	11	12	13	14	15	16	17	18	19	20
T (℃)	25	40	375	375	320	320	25	78	250	400	322	161	135	50	83	250	350	176	135	50
P (kPa)	2171	2137	2102	2068	2068	2068	2068	2068	2033	1930	1895	1861	1861	1826	1826	1792	1689	1654	1654	1620
($\dot{m}$ kg/s)	2.522	2.51	2.51	2.51	2.738	0.228	0.463	2.467	2.467	2.467	2.467	2.467	2.467	1.573	2.452	2.452	2.452	2.452	2.452	1.791

	21	22	23	24	25	26	27	28	29	30	31	32	33	34	35	36	37	38	39	40
T (℃)	79	250	350	178	135	50	50	91	50	50	70	320	320	320	50	92	25	105	95	92
P (kPa)	1620	1585	1482	1447	1447	1413	1413	2068	1413	103	2068	2068	2068	2068	1413	2102	103	2068	2068	2068
($\dot{m}$ kg/s)	2.419	2.419	2.419	2.419	2.419	1.94	0.679	0.679	1.261	0.228	0.228	1.505	0.878	0.627	1.034	1.034	0.093	0.093	0.772	0.94

Figure 2.15 SNG plant system design and state-points

The overall plant efficiency on an LHV basis results in 83.2%.

$$\eta_{plant} = \frac{LHV_{SNG} + \dot{W}_{elect}}{LHV_{H_2}} = 83.2\% \tag{2.20}$$

Table 2.2 gives the energy balance summary for the SNG production plant. The energy inputs, internal power use for each component, energy outputs, and efficiencies are stated here.

Table 2.2 Energy balance summary

	Value
Plant Inputs	
Hydrogen (kg/s)	0.463
Hydrogen LHV (MJ/kg)	120.2
Hydrogen HHV (MJ/kg)	142.2
Carbon Dioxide (kg/s)	2.522
Cooling Water (gpm)	169
Internal Power Use (kW)	
Bulk Recycle Compressor	88
CO_2 Recycle Compressor	65
H_2 Recycle Compressor	417
Membrane Compressor	146
MDEA Unit	29
Cooling Tower	125
Organic Rankine Cycle Units	-952
Total Internal Power Use	-82
Plant Outputs	
SNG (kg/s)	0.939
SNG LHV (MJ/kg)	49.2
SNG HHV (MJ/kg)	54.6
SNG Wobbe Index	47.5
Total Output LHV (MW)	46.2
Total Output HHV (MW)	51.3
Efficiency	
ORC Efficiency	12.0%
Plant Efficiency LHV	83.2%
Plant Efficiency HHV	78.0%

The hydrogen feedstock contains 66 MW of power on an HHV basis, and this is necessary to produce about 51 MW of SNG fuel. All of the internal power usage required by the compressors, the MDEA unit, and the cooling tower is supplied by the ORC units, and an additional 82 kW of power is produced. The largest internal power load of 417 kW is demanded by the H_2 Recycle Compressor. The Membrane Compressor is used for pressurizing the gas to increase the pressure difference across the membrane while simultaneously achieving the desired pressure for the product SNG; this compressor has the second largest electric demand of 146 kW.

The SNG production efficiency can also be described by a 2nd law analysis; the availability ($\dot{A}$), or exergy, of the input and output gas streams is calculated by:

$$\dot{A} = \dot{m}[h - h_o - T_o(s - s_o)] - \sum_i \mu_i \dot{n}_i \tag{2.21}$$

where $\dot{m}$ is the total mass flow rate of the gas, h and s are the enthalpy and entropy of the gas, respectively, h_o and s_o are the reference enthalpy and entropy, μ_i is the molar specific chemical potential of species i, and $\dot{n}_i$ is the molar flow rate of species i in the gas flow.

The 2nd law efficiency for the SNG production plant results in 84.1%. This efficiency is similar to that of the LHV efficiency from Equation 2.20, and it is slightly higher because the potential work done by the pressurized SNG is proportionally more than that of the H_2 and CO_2 feedstock; the pressure of the feedstock and products are not taken into account in the energy efficiency definition from Equation 2.20.

$$\eta_{SOEC,II} = \frac{\dot{A}_{SNG} + \dot{W}_{net}}{\dot{A}_{H_2} + \dot{A}_{CO_2}} \tag{2.22}$$

The model for the SNG production plant was reviewed by industry experts, and the methodology and performance results were approved [38]. Feedback from the reviewers was taken into consideration and slight adjustments were made to the plant at their request (all suggested modifications are incorporated into the described model).

2.7 SNG Plant Economics

The economics of producing SNG from renewable hydrogen are determined by first evaluating the capital investment of the plant. Operating costs are estimated from the plant components, and a life cycle cost analysis is used to determine the levelized cost of SNG. The effects of hydrogen feedstock cost and operating capacity factors are explored to determine the potential SNG production cost range.

2.7.1 Capital Investment

The capital costing of the plant utilizes quotes from industry, literature references, and AspenTech *Economic Analyzer*™ software for conventional plant components. Several of the components use a scaling method to determine the installed cost; the cost of each scaling unit (*S)* is based on the reference scaling unit (S_o) and base cost (C_0). The cost is then adjusted for the time-dependent equipment cost changes by using the Chemical Engineering Plant Cost Index (CEPCI). The installed cost (*IC*) is then calculated by using an installation factor (*IF*), which accounts for various costs associated with installing the component; the installation factor is only necessary if the referenced base cost does not include installation. Equation (2.23) is used to calculate the installed cost based on the given parameters.

$$IC = C_0 \left(\frac{S}{S_0}\right)^n \left(\frac{CEPCI}{CEPCI_0}\right) IF \tag{2.23}$$

The superscript *n* is the scaling factor which accounts for the economy of scale of a particular item. A detailed explanation of the cost estimation for each component is given as a footnote of Table 2.3. It should be noted that the level of capital cost analysis conducted for this study achieves an estimated accuracy of ± 30% [31].

The installation factor of 2.47 is based on Spath et al. [29], and the allocation of various costs associated with installation is given in Table 2.4. This factor is used only when the reference for capital cost does not include installation; the *Economic Analyzer*™ software includes a detailed installation calculation, so no factor is used for those components.

Table 2.3 Component capital costs in k$\$_{2009}$

	Base cost (C_o)[a]	Base Scale (S_o)[b]	Scaling Factor (n)[c]	Installation Factor (IF)[d]	Installed Cost (IC)[e]
LO-CAT™[f]	1319	22.6 kg/s	0.65	2.47	783
ZnO Bed[f]	49	22.6 kg/s	0.56	2.47	35
Heat Exchangers[g]		-	-	-	1,957
Reactors[g]	-	-	-	-	2,919
Catalyst[h]	1.2	1 ft^3	-	-	318
Compressors[g]	-	-	-	-	5,126
MDEA Unit[i]	1049	1 unit	-	2.47	2,591
Membrane Unit[j]	263	1 unit	-	2.47	650
ORC Units[k]	275	1 unit	-	2.47	2,717
Pumps[g]	-	-	-	-	214
Cooling Tower[g]	-	-	-	-	555
Total Installed Cost[l]	-	-	-	-	17,864
Total Direct Costs[m]	-	-	-	-	26,796

[a] These base costs have been scaled from the original cost index (CEPCI$_o$) to the 2009 CEPCI (521.9).

[b] The base scale is the unit for the referenced parameter. Many of these component costs are estimated from AspenTech *Economic Analyzer*™ which generates the installed cost directly.

[c] The scaling factor is not used for the components which were evaluated in AspenTech *Economic Analyzer*™ or discretely sized to the proper scale (e.g. the MDEA Unit).

[d] The installation factor is only used if the base cost does not include installation (otherwise its value is 1).

[e] The installed cost is calculated using Equation (2.23) or obtained directly from AspenTech *Economic Analyzer*™.

[f] Spath et al. [29] uses the scaling method from Eqn. (2.23).

[g] AspenTech *Economic Analyzer*™ software is used to calculate the installed cost of floating head shell and tube heat exchangers based on heat transfer area (heat transfer coefficients calculated from Peters et al. [31] and materials suitable for the operating temperature and pressure. Reactors were designed based on the given methodology described earlier. Stainless steel is used do mitigate corrosion from the catalyst packed bed. Each reactor was about 1 MM$\$_{2009}$. Several centrifugal compressors were installed including two multi-stage centrifugal compressors with intercooling based on number of stages, pressure ratio and cooling requirements. Centrifugal pumps are used for the ORC heating water source; six pumps are required for methanation reactor cooling and the interstage heat recovery. Cooling tower is sized based on water flow rate and temperature approach to wet bulb.

[h] Catalyst priced from industry quote [16] for SNG 1000 nickel supported catalyst.

[i] MDEA system cost calculated from industry software [39]. The specified separation of CO_2 resulted in a 55 gpm absorbant flow and a system of 60 gpm was matched to supply the separation.

Table 2.3: continued

[j] Peters et al. [31]: cost based on spiral wound membrane fibers for polysulfone based membrane. The upper end of the cost range of 100$$_{2002}$/ft^3 was used.
[k] Industrial quote [30] at $375,000 uninstalled. Four units are needed to utilize all of the available heat from the plant. A 2.47 installation factor was applied based on the method described below.
[l] This is the total calculated installed (TIC) cost of the plant components.
[m] A factor of 30% of TIC is used for high pressure (20 bar) piping installation based on Peters et al. [31]. A factor of 20% of TIC is used for buildings and structures of the plant. These costs are added to the TIC to determine the total direct costs (TDC) of the plant (TIC + 8.93 MM$).

Table 2.4 Installation factor cost allocation based on Spath et al. [29].

	% of TPEC
Total Purchased Equipment Cost (TPEC)	100
Purchased equipment installation	39
Instrumentation and controls	26
Piping	31
Electrical systems	10
Buildings (including services)	29
Yard improvements	12
Total Installed Cost (TIC)	247

The indirect costs associated with the plant are determined as a percentage of the TDC based on Spath et al. [29], and the allocation of various costs that contribute to the indirect costs of the plant are given in Table 2.5.

Table 2.5 Indirect costs allocated as a percentage of the TDC and actual value in MM$.

	% of TDC	MM$
Engineering	13	3.5
Construction	14	3.8
Legal and contractors fees	9	2.4
Project contingency	15	4.1
Total Indirect Costs	51	13.8

The total capital investment (direct plus indirect costs) for the plant is 40.9 MM$$_{2009}$. While slightly less detailed than the method used here to determine the capital investment, Lang Factors can also be used to calculate the total capital investment from the purchased (uninstalled) capital costs. Peters et al. [31] estimates an overall Lang Factor for chemical processing plants to be between 4.7 and 6.0. The equivalent Lang Factor for this plant can be determined by assuming an overall installation factor of 2.47 (only different for AspenTech Economic Analyzer™), and dividing total capital investment by the purchased equipment cost. For this plant, an overall Lang Factor is calculated to be 5.6, which is well within the range of that given by Peters et al. [31].

2.7.2 Operating Costs

The plant operating costs are determined by replacement cost estimations for the major plant components and by estimating unplanned maintenance and replacement as a fraction of the TDC as given by Table 2.6.

Table 2.6 Operating costs for major plant components

	Annual k$_{2009}$
LOCAT™[a]	62
ZnO Bed[b]	34
Methanation Catalyst[c]	159
MDEA[d]	68
Membrane[e]	130
Cooling Tower[f]	28
Total[g]	482

[a] Spath et al. [29]: 150 $_{2002}$/tonne sulfur removed
[b] Spath et al. [29]: reactor sizing from 4,000 GHSV with 4.67 $_{2002}$/lb-cat. Assumed catalyst density of 1200 kg/m^3
[c] Methanation catalyst replaced every 2 years
[d] Nextant [34]: operating costs scaled from 160 gpm to 60 gpm (this plant) MDEA flow rate using a 0.7 scaling factor. This includes make-up MDEA solution.
[e] Membrane replacement every 5 years.
[f] 5% of installed cost for water chemicals and pump maintenance.
[g] In addition to this annual O&M total, the ORC units must be replaced after 20 years.

In addition to these operating costs, other operating costs include staff and labor (12 staff members with a combined annual salary of 1.39 MM$), property tax and insurance (2% of TCI), and an unplanned O&M and materials replacement factor of 1% TCI. These estimations are consistent with the H2A analysis tool default values and H2A analysis case studies for similar sized fuel production plants [42]. The total annual O&M costs amount to 3.45 MM$ (14.2% of TDC, 8.4% of TCI).

2.7.3 Feedstock Costs

The feedstock to the SNG plant includes hydrogen, carbon dioxide, and water. The water consumption of the plant consists of cooling tower water make-up at 169 gpm, and this cost represents a very small fraction (0.01%) of the total feedstock cost. The cost of the carbon dioxide feedstock is estimated based on capture from a coal-fired power plant from Rubin et al. [40] to be 40 $/tonne, and this represents 7.4% of the total feedstock cost. The hydrogen feedstock cost is the most significant input with regards to the cost of SNG production. Several analyses have been conducted on hydrogen production from various renewable sources, and the hydrogen costs associated with production and transport (0.87 \$/kg-H_2 for a 100 mile pipeline delivery [41]) are given in Table 2.7.

Table 2.7 Hydrogen feedstock costs from various renewable sources [41]

	$/kg	$/MMBTU (HHV)
Current central wind farm electrolysis	6.71	49.8
Future central wind farm electrolysis	2.88	21.4
Current central biomass gasification	2.48	18.4
Future central biomass gasification	2.34	17.4

From Table 2.7, it is clear that the hydrogen source has a large impact on the cost of SNG. Even if the SNG production plant had a 100% energetic efficiency, no capital investment costs, and used the future scenario for hydrogen production from central biomass gasification (2.34 \$/kg-H_2), the resulting SNG would cost 19.4 $/MMBTU, which is just under double the rate that residential customers pay in the continental United States.

2.7.4 H2A Life Cycle Cost Analysis Tool

The total capital investment (direct plus indirect costs) and operating costs for the plant are inputs to the H2A life cycle cost analysis tool, which is used to generate a levelized cost of SNG fuel. The H2A tool accounts for the capital investment, fixed and variable operating costs, feedstock and utilities consumption rates, and the time span in which the plant operates [42]. Various economic parameters specified for the H2A program are given in Table 2.8.

Table 2.8 Economic parameter inputs to the H2A tool

	Value
Constant dollar value	2005
Internal rate of return (after-tax)	10%
Debt/Equity	0%/100%
Plant life	40 years
Depreciation	MACRS
Depreciation Recovery period	20 years
Construction period	2 years
1st year	75%
2nd year	25%
Start-up time	12 months
Revenues	50%
Variable costs	75%
Fixed costs	100%
Working capital	15% of total capital investment
Inflation rate	1.90%
Total taxes	38.90%
Decommissioning costs	10% of depreciable capital
Salvage value	10% of total capital investment
CO_2 feedstock cost	\$40/tonne
Hydrogen feedstock cost	Varied
Plant capacity factor	Varied

The dollar value of 2005 is used for the H2A analysis tool, so all of the plant costs reported in this chapter (and thesis) were adjusted from 2009 to 2005 using the CEPCI. Due to the variability of fuel and electricity escalation rates, the production costs for SNG were not adjusted from the output value of the H2A program, which are in 2005 dollars, but inflation was taken into account for the lifetime of the plant. It is assumed that the increase in *fuel* cost from inflation is negligible compared to the fluctuating cost of fuels, which don't necessarily coincide with the time-value of money.

2.7.5 Economic Results and Feedstock Cost Sensitivity

The economics of SNG production rely heavily on the hydrogen feedstock cost, and to a lesser extent, the plant operating capacity factor (the percentage of time that the plant operates at full capacity). The breakdown of cost contributions toward SNG production cost is given in Figure 2.17 at various hydrogen feedstock costs and a capacity factor of 90%.

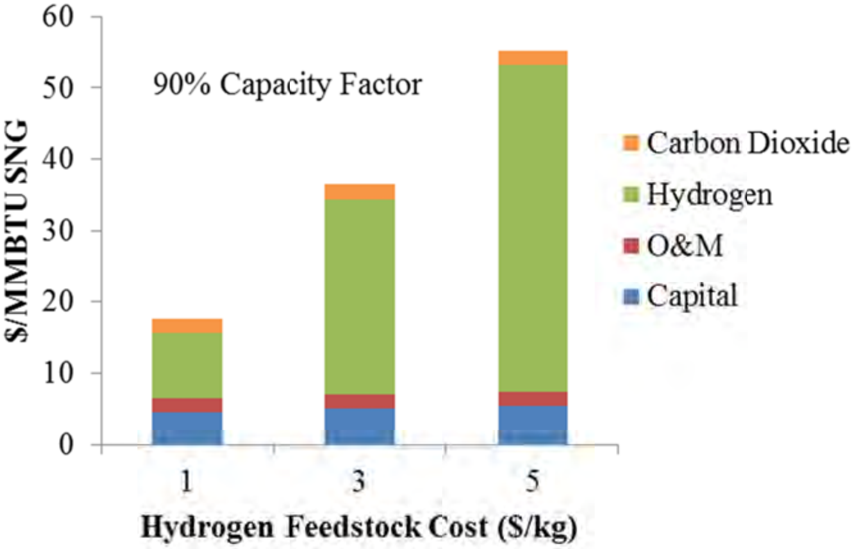

Figure 2.17 Cost contribution for SNG production at three different hydrogen feedstock costs and a 90% capacity factor

The hydrogen feedstock cost dominates the contribution distribution, especially for costs greater than 3 $/kg. Even at the very low hydrogen feedstock cost of 1 $/kg, it represents about half of the total SNG production cost. For a 3$/kg hydrogen feedstock cost, the hydrogen, capital, and O&M costs represent about 27, 5 and 2 $/MMBTU, respectively. The carbon dioxide feedstock cost represents 2 $/MMBTU.

Figure 2.18 is a similar chart showing how the cost contributions shift at various capacity factors with a hydrogen feedstock cost of 3 $/kg. At low capacity factors (40%), the contribution of capital and O&M costs become more significant; however, the hydrogen feedstock cost contribution is still greater than 50% at 3 $/kg, representing 27.4 $/MMBTU.

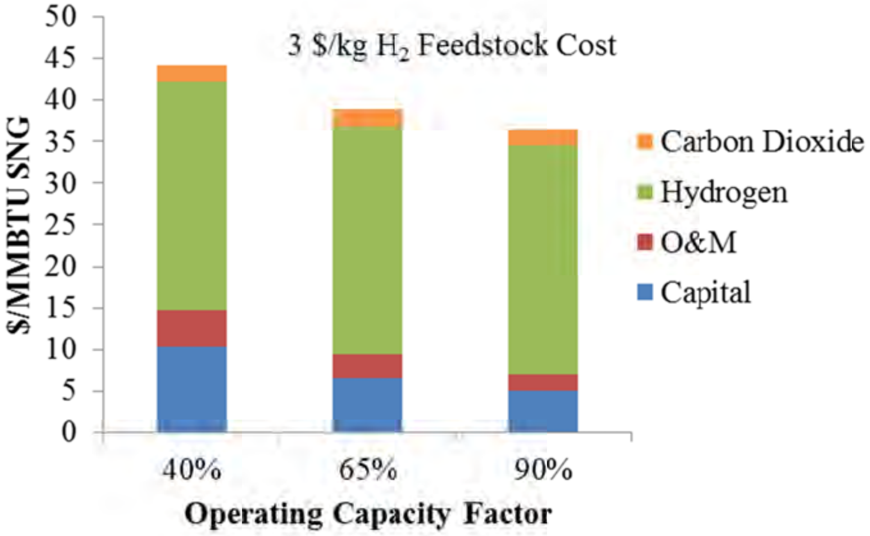

Figure 2.18 Cost contribution for SNG production at three different capacity factors and a 3 $/kg hydrogen feedstock cost

A range of hydrogen feedstock costs was given in Table 2.7, and the effects of this range on SNG production cost are explored in Figure 2.19.

The steep slope on the plotted lines of Figure 2.19 indicates the importance of obtaining a cheap source of hydrogen for producing economically competitive SNG. The range of costs for SNG production is 8.2 $/MMBTU with free hydrogen (and free delivery) and a 90% capacity factor, to 81.8 $/MMBTU with 7 $/kg-$H_2$ and a 40% capacity factor. For each 1 $/kg of hydrogen feedstock cost, the SNG production cost increases 9.4 $/MMBTU. The DOE cost target for large central hydrogen production by 2017 is about 2.2 $/kg; using this feedstock cost results in an SNG production cost of 28.6 $/MMBTU. The Energy Information Agency (EIA) states that the average cost of natural gas at the city-gate in the continental U.S. is approximately 5.5 \$/MMBTU, which is less than the SNG production cost using free hydrogen.

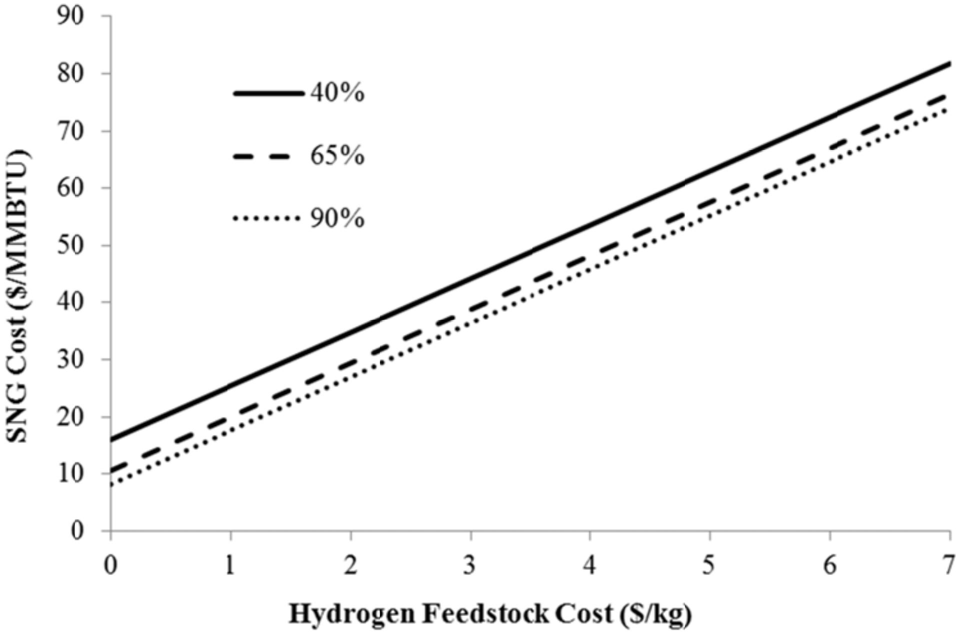

Figure 2.19 Effects of hydrogen feedstock cost on SNG production cost for various capacity factors

The effects of overall plant capacity factor on the SNG production costs are shown in more detail in Figure 2.20. While the operating capacity factor greatly increases the SNG production costs if lower than 50%, the effect is relatively small at larger capacity factors. The capital cost contribution increase is the main reason for this effect, and since it represents a relatively small fraction of the total cost, there are small SNG cost decreases for capacity factors greater than 60%. The SNG production costs decrease 50% by increasing the capacity factor from 20% to 60% and there is only a 12% cost decrease by increasing the capacity factor from 60% to 100%.

Despite the relatively small benefits from operating 90% of the time (e.g. versus 60%), every economic advantage must by sought. Hydrogen storage at the producer's site would enable high hydrogen feedstock availability, and this is important for continuous operation (assuming the wind farm electrolysis plant produces more than the maximum capacity of the SNG plant). The capacity factor should ideally be limited by general maintenance and replacements.

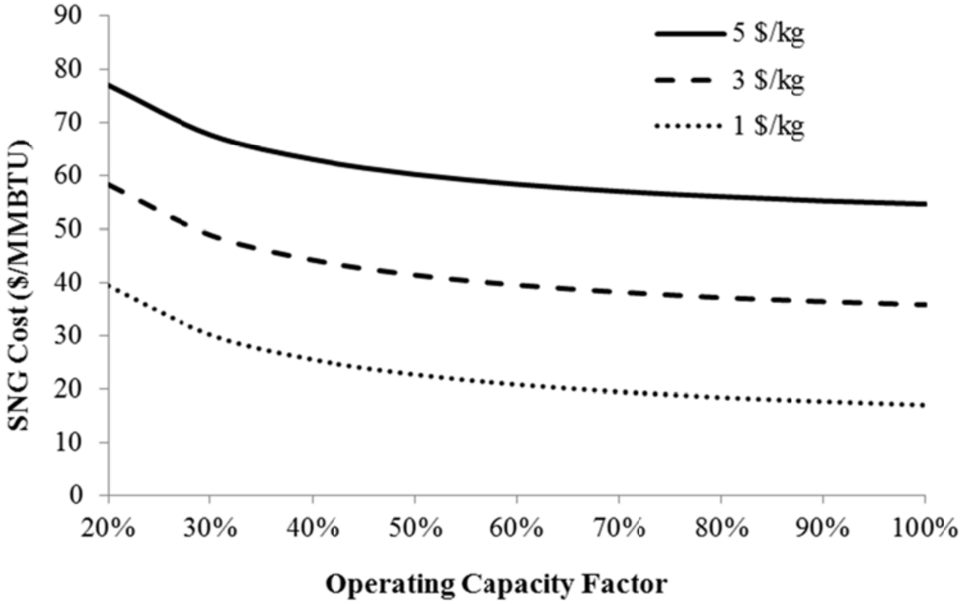

Figure 2.20 Effects of operating capacity factor on SNG production costs for various hydrogen feedstock costs

The range of hydrogen feedstock cost for this sensitivity analysis does not include large-scale hydrogen storage by the electrolysis plant, so it should be assumed that a capacity factor in the range of 40-50% can be achieved using this feedstock cost range. A capacity factor of 40-50% is slightly above that of a wind farm capacity factor, but since the plant is assumed to be under-sized compared to the wind-farm, a higher capacity factor can be achieved.

2.8 Summary & Conclusions

Thermodynamic and kinetic considerations of the methanation reaction were explored to model and simulate a system of reactors for the conversion of hydrogen and carbon dioxide to SNG. The carbon dioxide is assumed to be supplied by a power plant utilizing CC&S, and a clean-up process for the gas is necessary to remove sulfur molecules. Multiple reactor stages are used to increase temperature control of the reactor and drain water to promote the forward direction of the methanation reaction. Heat recuperation and recovery using ORC units for electricity generation utilizes the heat produced from the methanation reaction. Bulk recycle is used to increase the overall reactant conversion while allowing a satisfactorily high methane content SNG product with the limited extent to which the MDEA and hydrogen membrane units separate reactant species. The MDEA unit separates carbon dioxide for recycle to limit the undesired molecule content in the product gas. The hydrogen membrane separates hydrogen for recycle to increase the Wobbe index of the product SNG by increasing the methane content. The product SNG has a Wobbe index of 47.5 MJ/Sm^3 which is acceptable for natural gas pipeline transport and end-use appliances in the existing infrastructure. The overall plant efficiency is 78.1% HHV and 83.2% LHV.

The cost of the SNG product is highly dependent on the hydrogen feedstock cost. The range of costs for SNG production is 8.2 \$/MMBTU with free hydrogen (and free delivery) and a 90% capacity factor, to 81.8 \$/MMBTU with 7 \$/kg-H_2 and a 40% capacity factor. For each 1 \$/kg of hydrogen feedstock cost, the SNG production cost increases 9.4 \$/MMBTU.

CHAPTER 3

GASOLINE AND DIESEL PRODUCTION BY CO-ELECTROLYSIS AND FISCHER-TROPSCH SYNTHESIS

In a process similar to steam electrolysis for hydrogen production, a high temperature solid oxide electrolytic cell (SOEC) can be used to convert steam and carbon dioxide to syngas, which is composed primarily of hydrogen and carbon monoxide. Syngas can be used to generate liquid fuels in the Fischer-Tropsch (F-T) process, and this process has been proven in industrial plants (e.g., Sasol). For the GPSP scenario described in Chapter 1, the combination of large amounts of wind power and a carbon dioxide pipeline, a syngas producing co-electrolysis process followed by conversion to liquid fuels is well suited.

3.1 Prior Work

There are several studies that focus on producing syngas from co-electrolysis with the goal to produce liquid fuels. O'Brien et al. [43] modeled a process for large-scale (300 MWe) syngas production via solid oxide co-electrolysis (SOEC) coupled with nuclear reactor electricity and heat. The model used high pressure (35 bar) SOEC operation and a syngas product H_2:CO ratio of 2.1:1 based on the desired operating conditions of a cobalt catalyst Fischer-Tropsch reactor. The electrochemical model on which the SOEC was based did not take into account the methanation reaction, and this is an unrealistic assumption based on such high pressure operation with a nickel-based electrode used in the SOEC. The nuclear reactor process supplied the necessary heat for steam generation and feed gas preheat, which is an energy intensive process. Supplying the necessary heat without the use of a nuclear reactor is an important aspect of the co-electrolysis process that will need to be addressed for stand-alone applications. Since O'Brien et al. [43] did not model the actual production of liquid fuels, the synergies between the two subsystems were not addressed.

The biomass route to liquid fuel has been modeled by several studies (e.g. [9],[44][45]). A process for the production of syngas via biomass gasification followed by F-T liquid fuels production was modeled in Hamelinck et al. [44]. Through the use of a water gas shift reactor following the biomass gasification, the syngas has an H_2:CO ratio of around 2:1 for an F-T process. The F-T liquid fuels production cost of 2.44 \$/GGE (GGE is gallon of gasoline equivalent) was found. Using biomass gasification to produce useable fuel is a heavily researched topic, and the various processes involved depend on the desired product (electricity, hydrogen, liquid fuels, etc.). For electricity generation, the gaseous fuel would just need to be suitable for combustion in a gas turbine. Fuel production, whether hydrogen or hydrocarbon liquid fuels, requires several processing steps downstream of the syngas synthesis, including catalytic conversion, separation and purification.

A techno-economic study by Graves et al. [10] analyzed various non-biological pathways (thermolysis, electrolysis, photo-electrolysis) for syngas production and found that high temperature SOEC units are the most promising, which could then be used for liquid fuel synthesis. The performance assessment for the SOEC feed gas heating and electrochemical reactions, F-T conversion, and product upgrading did not give insight into the synergies between the subsystems. The study made optimistic assumptions to achieve an overall “electricity-to-fuel” efficiency of 70%. An electricity supply price of 4-5 ¢/kWh was used to achieve a gasoline production cost of about 3 \$/GGE; these costs are based on assumptions of 100% operating capacity, large scale manufacturing, and a high degree of technology maturity for all processes. Further investigation must be made to determine the true conversion efficiency from electricity to F-T liquid fuels and the economics of such a process.

3.2 Objectives

This chapter aims to (i) model a co-electrolysis syngas production system with a Fischer-Tropsch synthesis and upgrading process, (ii) explore the effect of SOEC operating conditions on syngas composition and performance, and (iii) conduct a techno-economic analysis that provides an estimate of the production costs of the liquid fuel products and its sensitivity to economic parameters, such as electrical energy feedstock cost and plant capacity factor.

The unique aspect of this study is the integration of the SOEC and F-T processes and the identification of the benefits and challenges of the entire pathway from electricity to liquid fuels. The level of detail included in this model allows for the determination of energy and cost intensive processes that need improvement for the viability of this renewable route to fuels. The scale of the plant is chosen to be 50 MW, and this is consistent with the size of a power generation system based on the capabilities of a wind farm, as discussed in Chapter 1.

A description of co-electrolysis is given along with a model for the reaction mechanisms and electrochemical performance. The co-electrolysis is modeled for SOEC technology, and operating parameters are chosen based on optimal conditions for producing a syngas feedstock for a F-T process. The F-T reactions and products are presented with emphasis on reactor operating conditions necessary to produce the desired hydrocarbons. The upgrading of F-T products is also modeled for the production of gasoline and diesel fuels. The overall liquid fuels production plant design is described, exploring the various synergies between the main subsystems. The model results of the process are then given, including a breakdown of the component energy requirements, the liquid fuels production quantity and several subsystem efficiencies. A scenario of operating the SOEC at elevated pressure (5 bar) is explored, and a comparison of the performance to the lower pressure operation is given. The economics of this process are evaluated for various electricity feedstock costs and operating capacity factors to explore the effects of producing liquid fuels from renewable sources of energy.

3.3 Solid Oxide Co-electrolysis

High temperature co-electrolysis modules electrochemically reduce water and carbon dioxide at high temperatures (650-1000 °C) to produce a syngas fuel by using electricity to drive the reactions. These reactions are shown in Equations. (3.1) and (3.2).

$$H_2O + 2e^- \rightarrow H_2 + O^{2-} \tag{3.1}$$

$$CO_2 + 2e^- \rightarrow CO + O^{2-} \tag{3.2}$$

Steam (water must be preheated) and CO_2 are fed to the cathode electrode, where electrons deriving from the applied voltage reduce the reactants to H_2 and CO, and each reaction produces an oxygen ion (O^{2-}). The O^{2-} diffuses through the electrolyte to the anode electrode, where it oxidizes to O_2 and releases two electrons. Although not necessary for the electrochemical reactions, air is fed to the anode electrode; the reasoning for this is given later in this section. There is an associated voltage with the current flow through the load, and this is dependent on the performance characteristic of the SOEC which determines the amount of total electric power ($P=iV$) that is required to produce an amount of syngas. This process is shown in Figure 3.1. The details of the SOEC performance model are given later in this chapter.

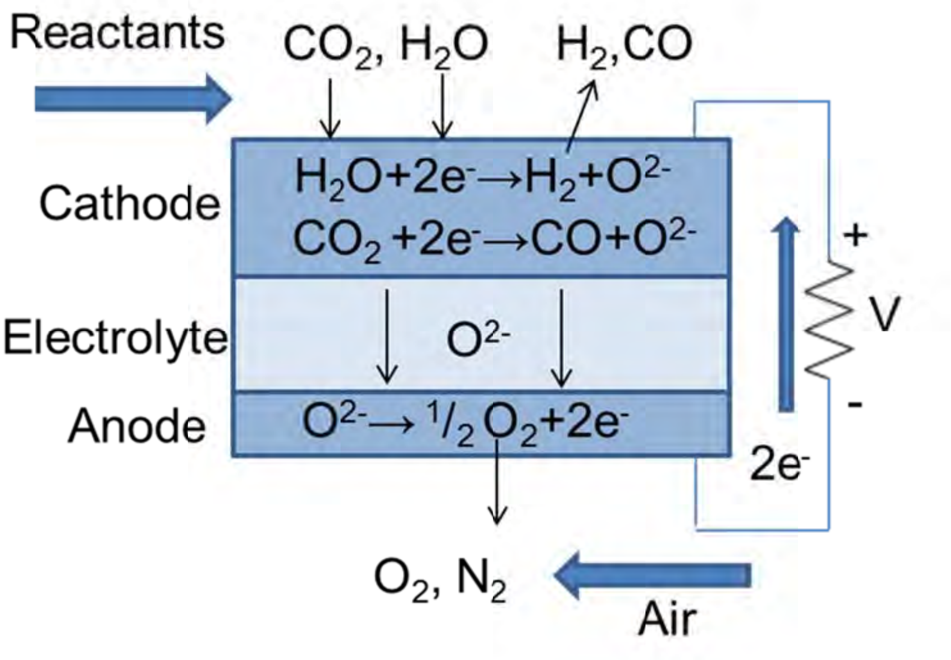

Figure 3.1 SOEC co-electrolysis operation schematic

It should be noted that SOEC technology is current under development, and it is in the laboratory testing phase. Several government and commercial institutions are giving this technology a great deal of financial investment and research due to its promising performance potential. The Idaho National Laboratory (INL) is working with modules developed by Ceramatec™ to test the durability and performance of these solid oxide cells. Other institutions working on the development of SOEC technology include Denmark's Risø National Laboratory and Versa Power Systems™. Although the technology is currently at a small-scale, laboratory tested level of maturity, the performance of laboratory testing is extrapolated to larger-scale systems to estimate the performance of mature SOEC technology.

The SOEC co-electrolysis process model was derived from Stoots et al. [46] and it incorporates both the electrochemical reduction of steam and carbon dioxide and the water-gas shift (WGS) reaction (Equation (3.3)).

$$CO + H_2O \leftrightarrow H_2 + CO_2 \tag{3.3}$$

The model outlined by Stoots et al. [46] simulates the co-electrolysis process by the following: (i) the gas first comes to equilibrium with respect to the WGS reaction, then (ii) the electrochemical reduction of water and carbon dioxide occurs, and finally (iii) the gas stream comes into WGS equilibrium again before it exits the SOEC. In reality, there are simultaneous electrochemical and catalytic reactions occurring down the length of the cell, but this zero-dimensional model adequately characterizes the SOEC performance (see Figure 3.2). The reverse of the WGS reaction is mildly endothermic and thermodynamically favorable at 800 °C, and the leftward reaction direction is further enhanced by the electrochemical conversion of steam to hydrogen.

While Stoots et al. [46] accounts only for the water gas shift reaction, the nickel-based electrode could also promote the methanation of carbon monoxide as given by Equation (3.4).

$$CO + 3H_2 \leftrightarrow CH_4 + H_2O \tag{3.4}$$

The methanation reaction of Equation (3.4) is exothermic, so it is not thermodynamically favored at high temperatures, but high pressures could promote this reaction. The model shown in Figure 3.2 accounts for both the WGS and the carbon monoxide methanation reactions, and it demonstrates that methane formation is negligible at atmospheric pressure. The model employed in this study matches the experimental data of cathode effluent composition of the SOEC as a function of the stack operating current, as shown in Figure 3.2.

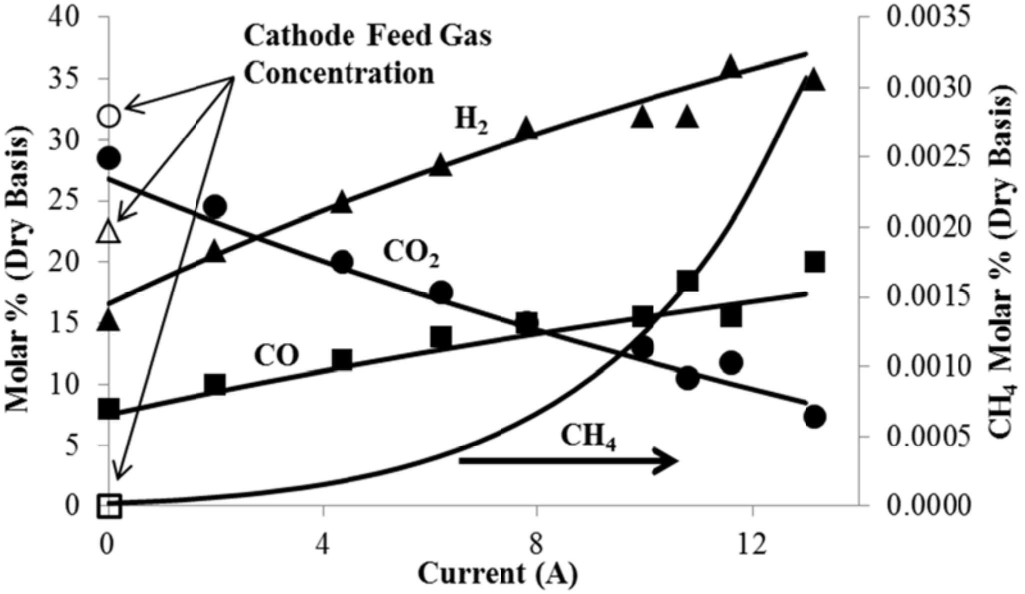

Figure 3.2 SOEC co-electrolysis model (lines) and experimental data (symbols) from Stoots et al. [46] for the cathode effluent composition at 800 °C and atmospheric pressure

Figure 3.2 shows a difference in composition between cathode feed gas and cathode exit gas for the open circuit condition (0 Amps). It is apparent from this difference that WGS equilibration occurs in the cathode compartment in the presence of the nickel-based electrode. It is well-known within the solid oxide fuel cell literature that WGS equilibration occurs very rapidly at these operating conditions and it is widely accepted that the fuel gas sustains WGS equilibrium over the entire electrode surface. Thus, the data given in Figure 3.2 supports the assumption of WGS equilibrium.

The effect of SOEC operating pressure on the equilibrium-based model with and without accounting for the methanation reaction is illustrated in Figure 3.3. The significant increase in methane formation at 20 bar operation lowers the hydrogen and carbon monoxide content of the cathode effluent by about 10%. The extent of the methanation reaction increases with higher CO_2 and H_2O content in the feed gas and with higher oxygen utilizations (higher current). The model results from Figure 3.3 has an equivalent feed gas composition and oxygen utilization as Figure 3.2 to show the model deviation for comparison, but it should be noted that the oxygen utilization (and subsequently the methanation reaction), will be much higher for the present study.

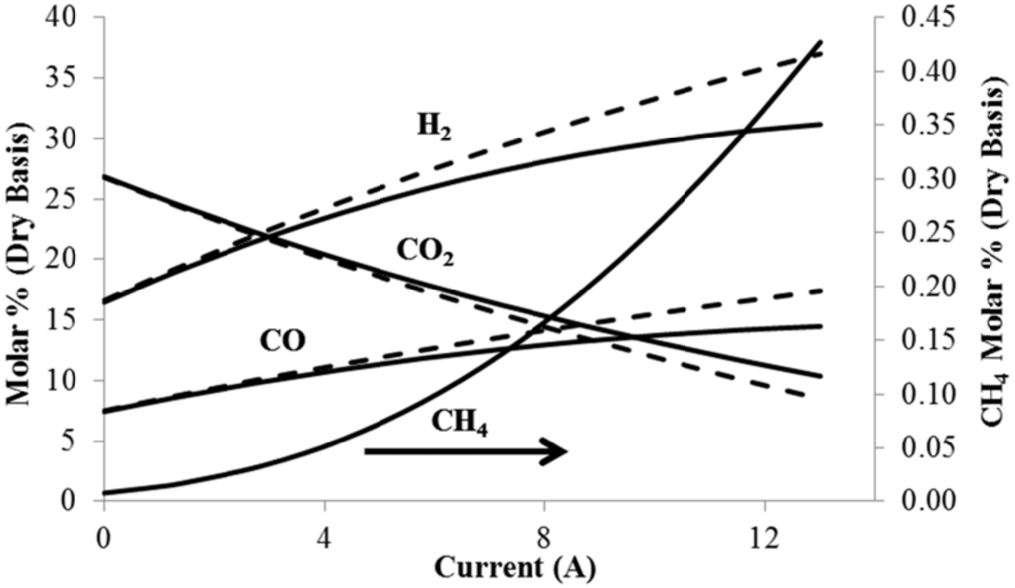

Figure 3.3 SOEC co-electrolysis model with (solid) and without (dashed) accounting for methanation reaction of the cathode effluent composition at 800 °C and 20 bar

The performance of the SOEC unit can be characterized by the Nernst potential, E_N, and the area specific resistance (ASR) given in Equations (3.5) and (3.6).

$$E_N = \frac{-\Delta G_{f,H_2O}(T)}{2F} + \frac{R_u T}{2F} ln\left[\frac{P_{H_2}P_{O_2}^{0.5}}{P_{H_2O}P_{atm}^{0.5}}\right] \tag{3.5}$$

$$ASR(T) = \frac{V_{op} - E_N}{j} \tag{3.6}$$

$\Delta G_{f,H_2O}(T)$ in Equation (3.5) is the gibbs energy of formation of water, and it becomes less negative with increasing temperature, effectively lowering the Nernst potential. The partial pressure terms in Equation (3.5) are calculated based on the average of the initial and final WGS equilibrium states for a zero-dimensional model. Equations (3.5) and (3.6) give a relationship between operating voltage, V_{op} (V), and current density, j (A/cm^2). The ASR value accounts for the total loss mechanisms in the operating cell, and it is assumed to follow an Arrhenius relationship to temperature, shown in Equation (3.7) [43].

$$ASR(T) = ASR_{1100K} - 0.463 + 3.973 * 10^{-5} exp\left(\frac{10300}{T(K)}\right) \tag{3.7}$$

The value of ASR_{1100K} is estimated to be 1.25 Ω-cm^2 for existing technology from O'Brien et al. [43]. Operating at 800 °C brings the ASR up to 1.37 Ω-cm^2.

The required size of the SOEC to provide a certain electrochemical conversion of steam and carbon dioxide can be calculated using the current density as shown in Equations (3.8), (3.9), and (3.10).

$$\dot{n}_O = \xi_{H_2O,e/c} + \xi_{CO_2,e/c} \tag{3.8}$$

$$I_{tot} = 2F\dot{n}_O \tag{3.9}$$

$$A_{tot} = \frac{I_{tot}}{j} \tag{3.10}$$

In Equations (3.8), (3.9) and (3.10), $\dot{n}_O$ is the molar flow rate of oxygen ions diffusing through the electrolyte, $\xi_{e/c}$ is the extent of reaction, in moles per second, of the electrochemical reduction of steam and carbon dioxide (Equations (3.1) and (3.2)), I_{tot} is the total current of the SOEC, and A_{tot} is the total active area required by the SOEC. The total DC power required by the SOEC is calculated from Equation (3.11).

$$P_{SOEC,DC} = V_{cell} I_{tot} \tag{3.11}$$

The electrochemical conversion of steam and carbon dioxide is specified such that the molar fraction of syngas (H_2 plus CO) leaving the SOEC unit is 0.9 (dry basis). This justifies the product syngas to be fed into the F-T reactor without the need for carbon dioxide separation. This is a constant oxygen utilization operation and results in an overall conversion of 76.6% H_2O and 76.9% CO_2 (molar basis). The definition of overall conversion for H_2O is shown in Equation (3.12).

$$X_{H_2O} = \frac{\dot{n}_{H_2O,cath\,in} - \dot{n}_{H_2O,cath\,out}}{\dot{n}_{H_2O,cath\,in}} \tag{3.12}$$

The relative electrochemical reduction of H_2O and CO_2 does not affect the overall conversion in this model due to the equilibrium calculation following the electrochemical reduction. The reduction of H_2O drives the WGS reaction to the left (Equation (3.3)), but the attendant reduction of CO_2 drives the reaction to the right. The steam is hypothesized to reduce much faster than the carbon dioxide due to the similarity in values of cell ASR between co-electrolysis and pure steam electrolysis and because the ASR value for pure steam electrolysis is approximately a factor of 3 less than that of pure carbon dioxide electrolysis [46], but this uncertainty does not affect the outlet cathode gas composition.

3.3.1 Methanation Equilibrium

This section aims to validate the assumption of equilibration of the methanation reaction in the SOEC cathode. Although the effects of the methanation reaction were not considered in the model developed by Stoots et al. [46], an experimental kinetic study on internal reforming of methane (the reverse of the methanation reaction) for a Ni/YSZ anode supported SOFC was conducted to derive a reversible rate equation (Equation (3.13)) for temperatures in the range of 600-850 °C [47].

$$r_{ref} = -k(T)P_{CH_4,s}\left(1 - \frac{P_{H_2,s}^3 P_{CO,s}}{K_{ref}P_{H_2O,s}P_{CH_4,s}}\right) \quad (3.13)$$

r_{ref} (mol/s-m^2) is the rate of methane reforming per unit reaction area, *k(T)* is the temperature dependent rate constant, $P_{i,s}$ is the partial pressure of species *i* at the reaction surface, and K_{ref} is the equilibrium constant. This rate equation is used with the reaction area of the SOEC stack to determine the composition at the outlet of the cathode. A combination of high pressure, low CH_4 and H_2O content, and high H_2 and CO content drives the reaction towards the formation of methane. It is confirmed from Timmermann et al. [47] and using Equation (3.13) with the stack area calculation from S*ection 3.3*, that the gas comes to equilibrium at 800 °C and 1 bar; this is shown in Figure 3.4.

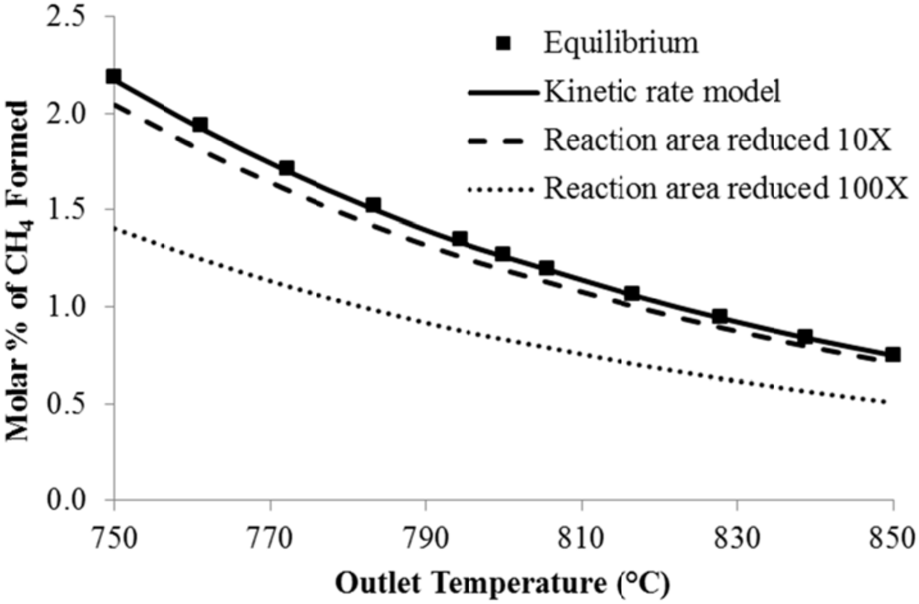

Figure 3.4 Temperature dependence comparison of methanation equilibrium and kinetic rate composition prediction from Equation 3.13 at 1 bar. The effects of reducing the reaction area in the kinetic rate calculation by factors of 10 and 100 are shown

There is uncertainty in estimating the reaction area which is used to determine the reaction rate (Equation (3.13)). A conservative estimate is to approximate the porous fuel cell electrode area as equivalent to the triple phase boundary area of the cell, which is calculated from Equation (3.10). This estimation is conservative because there is additional reaction area from the extended surface area of the porous electrode membrane. To show that the use of a much *smaller* reaction area than the *conservative* estimation given (possibly due to operating at a higher current density), Figure 3.4 also shows the rate calculation using reaction areas reduced by factors of 10 and 100; equilibrium of the cathode gas stream is closely approached for a factor of 10 reduction in active area, and there is just a 25% reduction in methane produced using a factor of 100 reduction.

Although Timmermann et al. [47] did not elevate the pressure of the SOFC gases to determine more accurate pressure dependence of this rate equation, it is assumed that equilibrium is obtained for higher pressures for this study.

3.3.2 SOEC operating conditions sensitivity

While there are not extensive studies optimizing the operating conditions of solid oxide co-electrolysis units, there have been studies on the operation of high temperature steam electrolysis using SOEC modules. Gopalan et al. [48] conducted a modeling study on the effects of operating conditions on the overall efficiency (including heat recuperation, air blowers, etc.) of an SOEC module. It was found that for large stacks, operating at the thermal neutral voltage achieved the highest overall efficiency.

The effects of operating the SOEC unit at elevated pressures are now discussed in relation to synergies with the product syngas going to an F-T reactor, which operates at high pressure (~40 bar). Although a relatively small effect, high pressure increases the Nernst potential from Equation (3.5) which lowers the current density for a given operating voltage; this will increase the size and capital costs of the SOEC stack. Operating the SOEC at 20 bar under conditions of high reactant (steam and CO_2) concentration and high oxygen utilization produces significant methane (~10% molar) from Equation (3.4), and there is an exotherm associated with this reaction.

The cathode outlet compositions at various SOEC operating pressures are given in Figure 3.5; the inlet concentrations were adjusted to achieve the necessary 2.1:1 H_2 to CO ratio in the syngas. As the pressure increases from 1 bar to 20 bar, Figure 3.5 shows the formation of CH_4 is favored over H_2 and CO. A CH_4 content of 12% (dry molar basis) is present in the cathode gas stream when operating at 20 bar. The H_2 and CO content decrease 20% from operation at 1 bar to 20 bar. This trend is consistent with Le Chatlier's Principle for the effects of an increase in pressure on non-equimolar reactions.

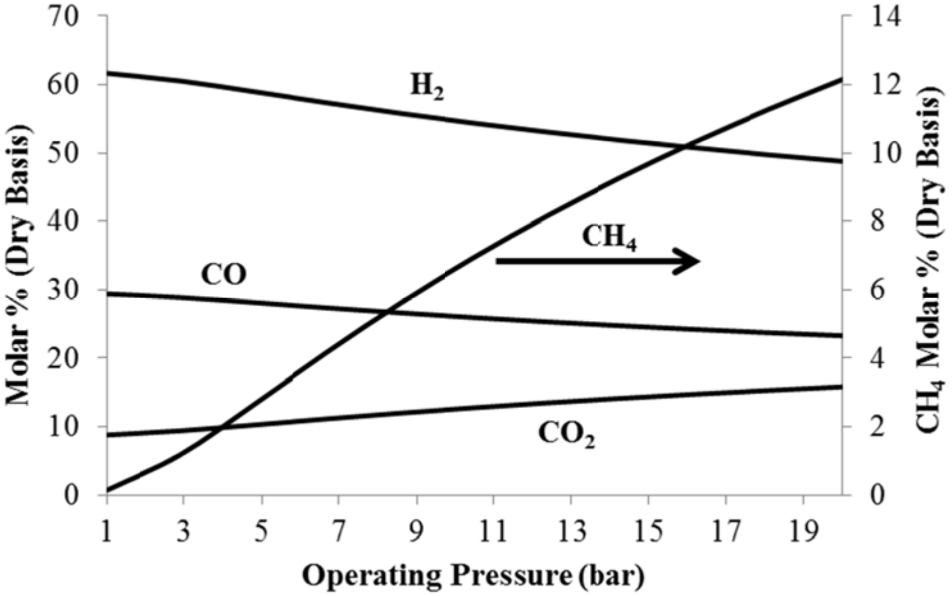

Figure 3.5 Molar composition of cathode effluent dependence on operating pressure at an operating temperature of 800 °C (isothermal). A constraint of achieving a 2.1:1 ratio of H_2 to CO is used

There is also a trade-off between operating the SOEC at the thermal neutral voltage, where the irreversibility of the electrochemical reactions supply the heat for isothermal operation, and operating below the thermal neutral voltage, which will lower the temperature of the product gas, decrease the extent of the reverse WGS reaction, and increase the extent of the methanation reaction. Although high voltage will increase the reverse WGS reaction and decrease the methanation reaction, higher voltage increases the power consumed by the SOEC, which lowers the efficiency.

Figure 3.6 illustrates the effect of allowing a temperature depression for the SOEC on the composition of the cathode effluent. Allowing a 100 °C temperature depression (from 800 °C to 700 °C) increases the CH_4 content to about 3.3% at a pressure of 1.6; the increase of CH_4 is much greater if operating at elevated pressures. The H_2 and CO content decrease by 9% from operation at 800 °C to 700 °C, and this represents a significant loss in reactants for the F-T reactor.

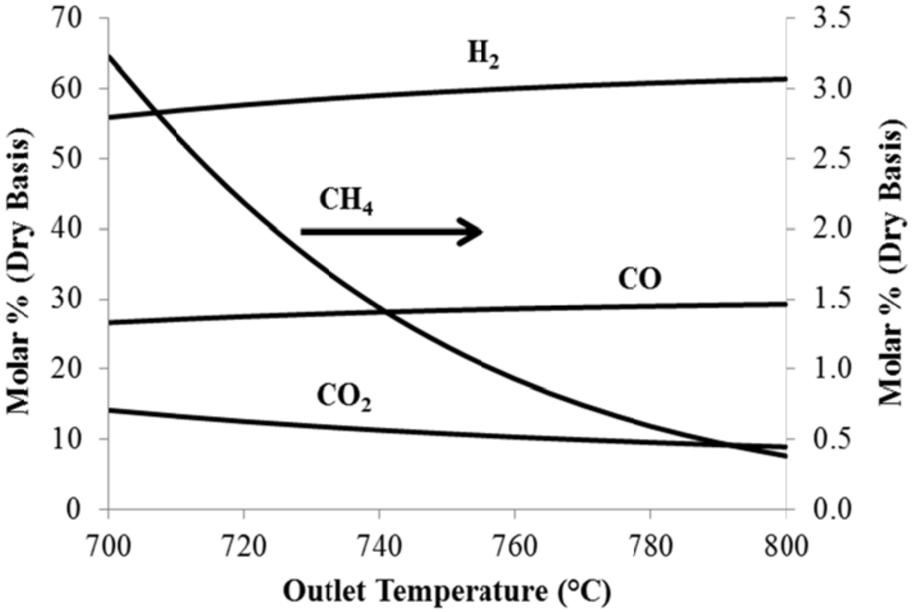

Figure 3.6 Molar composition (dry) of cathode effluent dependence on outlet temperature at a pressure of 1.6 bar with a cathode inlet temperature of 800 °C

The heat from the exothermic methanation reaction results in a lower voltage requirement to operate the stack isothermally or to control the cathode outlet temperature (e.g. 750 °C or 700 °C); the voltage requirement for a given cathode outlet temperature is given in Figure 3.7. The operating voltage decreases significantly as the pressure increases and the temperature decreases. While this lowers the power requirement of the SOEC, the product syngas will contain over 17% inert molecules (CO_2 and CH_4) when allowing a 100 °C depression at atmospheric pressure which significantly lowers the convertible reactants for the F-T reactor. Operating at the thermal neutral voltage to maintain isothermal operation at 800 °C achieves a syngas with about 10% inert molecules, and the benefits of increased reactant concentration for the F-T reactor outweigh the decrease in electric power consumption from an overall plant efficiency standpoint.

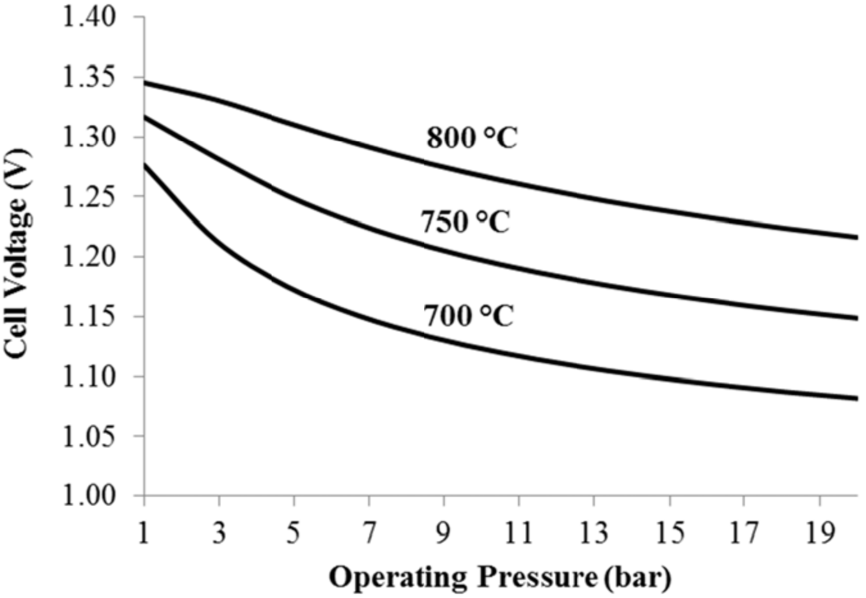

Figure 3.7 Effect of operating pressure on lowering the required voltage to maintain a certain cathode gas outlet temperature for an inlet temperature of 800 °C

The excess heat from the anode sweep air (enters at 800 °C) is also used to moderate the temperature depression in the stack; the anode effectively acts as a heat source for the endothermic cathode reactions. The gas at the anode outlet is assumed to have the same temperature as the cathode outlet; this is a reasonable assumption for an SOEC in a co-flow arrangement, which is a beneficial flow geometry for the providing the most heat to the fast endothermic reverse WGS reaction. Although the SOEC operates at a lower voltage (less power required) for high pressure, increased compression energy will be required for both the cathode and anode gas streams.

The polarization curve based on the temperature dependent ASR value (Equation (3.7)) at two different cathode operating pressures and outlet temperatures is given in Figure 3.8. The temperature has a large impact on performance because of the ASR's dependence, but the pressure also increases the voltage due to the increase in Nernst potential (Equation 3.5). A high temperature and low pressure operating condition results in the highest current density for a given voltage, and this is favorable for the economics because a smaller stack size is required for the chosen power input. The performance model for the cell ASR is only dependent on temperature, but in reality, the pressure could affect the ASR. The ASR of an SOEC is expected to decrease with increasing pressure due to the favorable impact on concentration polarizations, but such potentially beneficial impacts on the ASR, which are predicted to be relatively small, are not capture in this model.

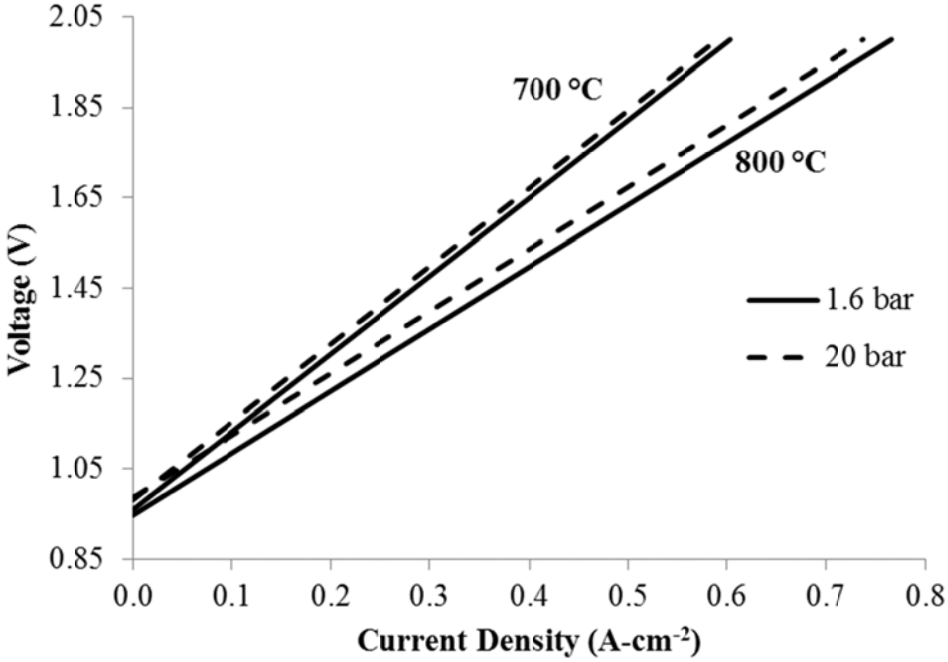

Figure 3.8 Polarization curve based on Equations (3.5)-(3.7) at various temperatures and pressures. The composition is fixed from constant oxygen utilization and desired cathode outlet ratio for H_2:CO of 2.1 to 1

There is much uncertainty in the ability of solid oxide electrochemical stacks to operate at elevated pressure due to material strength concerns (particularly from gas pressure differences across the cell) and the gas leakage effects. Although the methanation reaction occurring at high pressure allows for a lower thermal neutral voltage, CH_4 is an inert, undesired product for the F-T synthesis reactor. In order to achieve the highest content of syngas at an H_2:CO ratio of 2.1 to 1, operation at lower pressures (1-2 bar) would be more beneficial. Although there is more of a compression penalty for pressurizing the syngas downstream, the increased content of H_2 and CO in the F-T synthesis reactor allows a higher per pass conversion and selectivity toward desired products.

Considering the effects of operating at various pressures and temperatures, this study chooses to operate the SOEC at a modest pressurization of 1.6 bar and isothermally at 800°C for the baseline case. This allows for a high percentage (~90%) of H_2 and CO in the product syngas, and it increases the current density compared to higher pressure and lower temperature. The scenario of operating the SOEC at 5 bar is also presented later in this chapter for comparison, and the various system level effects are explained.

3.4 Fischer-Tropsch Synthesis

The syngas produced from the SOEC is supplied to an F-T reactor for conversion to hydrocarbons. The product distribution can be described by the Anderson-Schulz-Flory (ASF) model shown in Eqn. (3.14).

$$C_n = \alpha^{n-1}(1-\alpha) \tag{3.14}$$

C_n is the molar fraction of hydrocarbons having length n (carbon number), and α is the chain growth probability factor. The value for α depends on reactor type and operating conditions such as partial pressures of H_2 and CO, catalyst type, and temperature. Higher values will lead to an increased longer chain hydrocarbon yield. With advances in reactor design and catalyst preparation, alpha values between 0.8 and 0.94 can be achieved [49]. The product distribution was determined using the ASF distribution with an alpha value of 0.9 along with an adjustment to the lower carbon number yields (C_{4-}) based on Hamelinck et al. [44]; this accounts for the deviation of the ASF model with what is commonly seen in practice (e.g. a higher than predicted CH_4 (C_1) yield with lower C_{2-4} yields for cobalt catalyst reactors). Figure 3.9 illustrates the mole and mass distribution which results from the model.

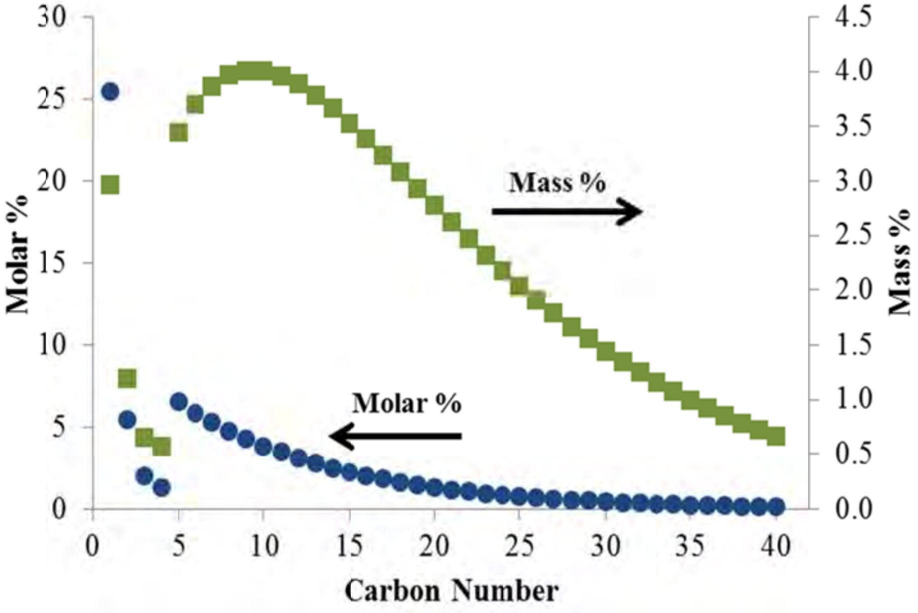

Figure 3.9 ASF distribution with α=0.9 and $C_{1\text{-}4}$ redistribution

The distribution was taken up to a carbon number of 100, although this is not shown in the Figure 3.9; the mass fractions of C_{40+} molecules are significant to the wax yield. Oxygenates and aromatics production from the F-T reactor is assumed to be negligible in this study; the presence of these molecule types are typically small for low-temperature (220-260 °C) F-T synthesis [50]. Although not addressed in the model, any amount of oxygenates, which are water soluble, would necessitate a water treatment process before the water is re-used or purged to the environment.

Certain ranges of carbon number molecules are classified based on their boiling points and combustion properties. The LFG (C_{4-}) are useful only for burning for heat recovery, since they are not directly convertible to liquid fuels. The C_5/C_6 gases are able to be blended with the gasoline stock by using an isomerization process, described below. The $C_{7\text{-}10}$ gases are called naphtha, and they are the main components in the gasoline blending stock. The $C_{11\text{-}19}$ gases are called middle distillates, and they are the products for diesel fuels. The C_{20+} gases are called wax, and these can be selectively cracked down to lower carbon ranges for either gasoline or diesel production.

Figure 3.10 shows the distribution of relevant ranges of hydrocarbons determined from the model.

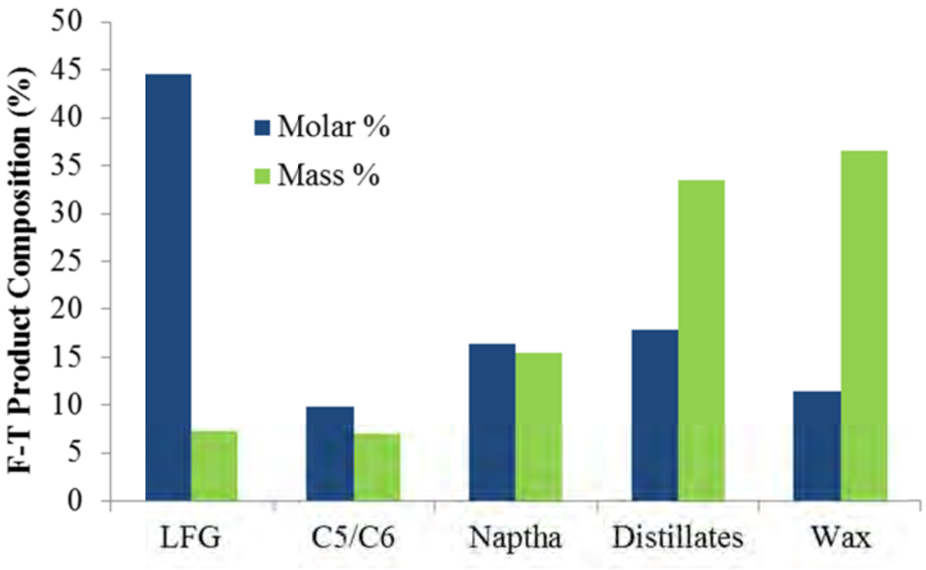

Figure 3.10 F-T product composition grouped by hydrocarbon range from ASF distribution

The yield of paraffins (C_nH_{2n+2}) versus olefins (C_nH_{2n}) in the product distribution from Equation (3.12) must also be determined. It has been shown that cobalt catalysts saturate the hydrocarbons at a faster rate than iron catalysts, thus producing mainly paraffins [51]. An estimated yield of paraffins based on findings of Leckel [52] of 80% (molar basis) of each carbon number is used; in reality the relative paraffin yield would differ depending on hydrocarbon number, but this approximates the overall yield.

In order to simplify the system model with respect to the types of hydrocarbon molecules, it was necessary to represent certain ranges of carbon lengths with a fewer number of molecules. In particular, the $C_{1\text{-}4}$ molecules were kept in detail, while $C_{5\text{-}6}$ were modeled as C_6, $C_{7\text{-}10}$ were modeled as C_8, $C_{11\text{-}19}$ were modeled as C_{16}, and C_{20+} were modeled as a combination of C_{24} and C_{32}. The distribution was normalized to achieve an atom balance in the product yield ranges. The translation from the ASF distribution described earlier to the representative molecular distribution achieves an accurate approximation for the heating value of the liquid fuel products to within 1%.

The conversion extent must be specified to determine the amount of hydrocarbons to allocate to the ASF distribution. The reaction shown in Equation (3.15) is the most basic reaction that takes place in the F-T reactor.

$$CO + 2H_2 \leftrightarrow -CH_2- +H_2O \tag{3.15}$$

The $-CH_2-$ is the chain growth molecule on which higher hydrocarbons build, and the conversion from CO and H_2 to this growth molecule is a necessary step to determine the amount of hydrocarbons formed.

A Langmuir-Hinshelwood-Hougen-Watson (LHHW) rate equation for carbon monoxide was developed by Yates et al. [53] as shown in Eqn. (3.16).

$$-R_{CO} = \frac{aP_{CO}P_{H_2}}{(1 + bP_{CO})^2} \tag{3.16}$$

The kinetic rate constant, *a* (0.013 mol/skg$_{cat}$), and the CO adsorption constant, *b* (1.62 bar^{-1}), were determined based on a slurry bubble column reactor (SBCR) operating at a temperature of 240 °C. While this rate equation fit well to experimental data, it was later found that it did not capture an accurate pressure dependence of the reaction due to the small range of operating pressures studied (0.5-1.5 MPa). A more recent study (Espinoza et al. [54]) performed a rigorous kinetic analysis for a cobalt catalyst SBCR to determine the CO adsorption constant and reaction order in the LHHW rate equation (Equation (3.17)) by using a wide range of pressures (5-40 bar) and H_2/CO ratios (1.6-3.2) . The catalyst had been previously used, and it was considered a good approximation for a lifetime average activity.

$$-R_{CO} = \frac{aP_{H_2}^{0.75}P_{CO}^{0.5}}{(1 + bP_{CO}^{0.5})^2} \tag{3.17}$$

The value for the CO adsorption constant (*b*) at 230 °C was found to be 1.55 bar$^{-0.5}$, which is very close to the value that Yates et al. [53] found at 240°C. While Botes et al.

[54] did not vary the operating temperature for determination of the rate constant *a*, the rate constant from Yates et al. [53] could be substituted because it used the same reactor operating temperature.

The partial pressures in Equation (3.17) are at calculated at the outlet of the reactor for SBCR designs. Cobalt-based catalysts have been shown to perform well under high per-pass conversion regimes, especially operating at high pressure (40 bar) compared to iron catalyst reactors [55]. Per pass conversions of 80% can be achieved in SBCR reactors. Since there is a trade-off between per-pass conversion and selectivity to higher hydrocarbons, a slightly lower conversion than 80% should be used when operating for a higher alpha value (0.9 in this study). The once-through conversion of carbon monoxide is chosen to be 70% (designates the hydrogen conversion at about 75%). Equation 3.17 allows for the calculation of catalyst weight which can then be used to size and cost the reactor. The conversion from catalyst weight to reactor volume assumes a 30% catalyst solution by volume, which equates to 600 kg-cat/m^3. The SBCR for F-T synthesis also produces steam from its water-fed cooling coils. The chosen reactor temperature and pressure are 240 °C and 40 bar based on achieving the performance estimation for conversion and selectivity described above.

3.5 Supporting Plant Processes

Various other subsystems are required for the liquid fuels production plant: carbon dioxide clean-up, feedstock mixing and heat recovery, product upgrading, and hydrogen production (for product upgrading and the SOEC). Figure 3.11 shows a high-level plant diagram, including the various subsystems.

3.5.1 Carbon Dioxide Clean-up

The carbon dioxide feedstock to the SOEC is assumed to be supplied from a coal gasification plant (e.g. GPSP). Most absorption-based carbon capture technologies, such as monoethanolamine or rectisol sorptive processes capture a significant fraction of the hydrogen sulfide (H_2S) in addition to carbon dioxide contained within the gas. While employment of these technologies for simultaneous removal of CO_2 and H_2S would be acceptable for an enhanced oil recovery process, such as the GPSP in North Dakota, the H_2S content is unsuitable for the SOEC and the F-T catalytic reactor. The GPSP facility uses a rectisol process to capture CO_2 from gasified coal at the plant, and the captured gas stream contains 0.9% H_2S on a molar basis [56]. This high content of sulfur must be reduced down to less than 1 ppmv to avoid poisoning both the electrocatalysts within the SOEC unit and F-T catalysts. The LO-CAT™ process is chosen for bulk H_2S removal, which is capable of reducing the H_2S concentration down to ~10 ppmv where a ZnO bed can then polish the gas to the required 1 ppmv or lower level [29]. These technologies are proven effective, and the main energy requirement is the cathode gas preheat prior to the ZnO bed, which operates at 375 °C.

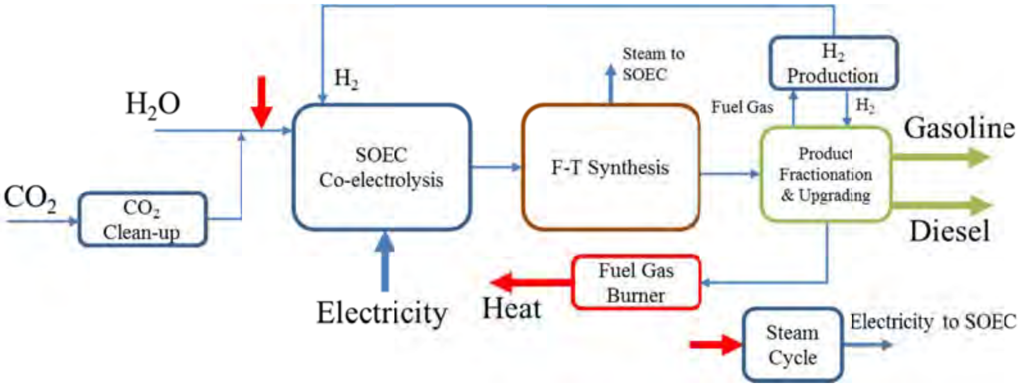

Figure 3.11 Co-electrolysis syngas to F-T liquid fuels production plant block diagram

3.5.2 Feedstock Mixing & Preheat

The amount of carbon dioxide fed into the SOEC unit is determined by the scale of the plant, which is chosen to be about 50 MW (AC power in). The amount of steam addition to the SOEC cathode is then adjusted to achieve a 2.1:1 molar ratio of H_2 to CO in the product syngas. The resulting CO_2 feedstock amounts to about 120,000 tonne/yr which is equivalent to roughly 3% of the CO_2 produced from a 500 MW coal fired power plant. The heat source for the steam required by the SOEC unit is mainly supplied by the F-T synthesis reactor (exothermic reactions heat the water-fed cooling coils) along with additional heat from recuperation of the cathode effluent gas stream. This ratio is chosen based on the stoichiometric conversion of syngas to hydrocarbons in a cobalt-based catalytic F-T reactor. The presence of hydrogen at the cathode inlet of the SOEC unit is necessary to prevent the oxidation of the nickel-based electrode. The scrubbed carbon dioxide is then mixed with the steam and hydrogen before being heated to 800 °C by the burner effluent. The fuel for the burner is the LFG produced from the F-T synthesis island.

Sweep air for the anode is fed into the system at a rate which produces an anode effluent with a molar fraction of 50% oxygen. Sweep air is used because of the chemical reactivity of pure oxygen at elevated temperatures. Sweep air also allows for better temperature control over the stack if operation is not isothermal. There are other technical issues such as hydrogen leakage that could potentially be harmful to the performance if no sweep air is present. The sweep air must be heated to 800 °C pressurized to 2 bar to account for pressure losses downstream.

After supplying the necessary heat for various processes in the plant, the burner effluent heat is used as the heat source (~700 °C) for a steam rankine cycle. The cycle is assumed to operate at 25% net thermal efficiency; the supply heat is extracted from lowering the cathode effluent and combustor effluent down to 100 °C. This is a simplified assessment of a steam cycle, but the performance estimation is adequate for this model.

3.5.3 Product Upgrading

Upgrading of the F-T synthesis products is necessary to generate high quality gasoline and diesel fuels. The processes for upgrading the F-T synthesis reactor products to gasoline and diesel fuels are similar to that which is used for conventional crude oil refining, but there are several differences in operating parameters between crude oil refining and F-T product ("syncrude") upgrading [50] which are described later. There are seven major unit operations carried out for F-T product upgrading: fractionation (distillation), hydrogen production, wax (C_{20+}) hydrocracking, naphtha (C_{5-10}) hydrotreating, middle distillate (C_{11-19}) hydrotreating, C_5/C_6 isomerization, and catalytic reforming (for C_{7-10}). These processes are described in terms of the model assumptions and performance characteristics. The product yields and utilities consumption for several unit operations are based on Bechtel [45].

3.5.3.1 Hydrogen Production

Hydrogen production is necessary for several upgrading processes, and hydrogen is also required as a feed gas to the SOEC, as described earlier. Following the F-T synthesis reactor, the syngas is cooled by heat exchange to cooling water and depressurized from 40 bar to 26 bar in a flash drum, allowing unreacted syngas, LFG, and inert gases to evaporate and separate from the heavier (C_{5+}) hydrocarbons. This allows for a pressurized, hydrogen rich stream to be fed into a hydrogen recovery subsystem, which first goes into a WGS reactor to increase the hydrogen partial pressure before being fed into a PSA unit, which separates hydrogen. A small fraction (2%) of the F-T reactor feed syngas is also diverted to this unit to increase the content of hydrogen entering the PSA to 70% (molar basis) which is necessary for adequate PSA performance (85% hydrogen separation) [29].

3.5.3.2 Product Fractionation

A distillation tower is needed to fractionate the products into naphtha, middle distillates, waxes and additional LFG. The fractionation occurs at atmospheric pressure by heating the feed gas to a temperature of about 400 °C to vaporize all but the heaviest hydrocarbons. A simplified explanation of the distillation process is as follows: the difference in boiling points of the hydrocarbons and the use of perforated trays to condense and trap lower boiling point molecules allows for product separation as the gases cool while traveling up the distillation column. There are steam addition stages, heat exchangers, and reflux drum separation processes that occur during distillation [57], but these details are not explicitly modeled.

3.5.3.3 Naphtha & Distillate Hydrotreating

The naphtha and middle distillate fractions go to their respective hydrotreating plant, where hydrogen is fed with the hydrocarbons to a metal-oxide catalytic reactor. The reactor operates at around 350 °C where the olefins are hydrogenated to paraffins (saturation) to increase the heating value and octane rating of the gas stream. An example of a saturation reaction is shown in Eqn. (3.18).

$$C_8H_{16} + H_2 \leftrightarrow C_8H_{18} \tag{3.18}$$

In comparison to conventional crude oil refinery hydrotreating processes, the hydrogen demand for F-T hydrotreating is much less due to the high content of paraffins and the lack of sulfur and oxygenate molecules; this also results in a nearly isothermal reactor operation [50].

3.5.3.4 Wax Hydrocracking

The wax fractions are sent to a hydrocracking plant to break the heavy wax content down to useful naphtha and middle distillates for gasoline and diesel blending. The hydrocracking simultaneously saturates the olefins to produce paraffins. Similar to F-T hydrotreating, the hydrocracking process requires less hydrogen than conventional crude oil refinery hydrocracking. F-T hydrocracking can also operate at lower temperatures (300 °C) and pressures (3-5 MPa) than crude oil hydrocracking. The reactor is nearly isothermal due to the balancing of the endothermic cracking reactions and the exothermic hydrogenation reactions [50]. An example of a hydrocracking reaction is shown in Eqn. (3.19).

$$C_{32}H_{66} + H_2 \leftrightarrow 2C_{16}H_{34} \tag{3.19}$$

3.5.3.5 C_5/C_6 Isomerization

The C_5/C_6 yields from the naphtha hydrotreater and wax hydrocracker are sent to a catalytic isomerization reactor, which rearranges the molecular structure of the C_5/C_6

hydrocarbons to convert normal pentanes and hexanes (straight chain molecules) into iso-pentane and iso-hexane (branched molecules) to increase its octane number. The reactor operates at approximately 200 °C and 20 bar. The octane rating (OR) is the average of the motor octane number (MON) and research octane number (RON); the isomerization unit increases the OR of the feed stream to about 82 (from ~60), and the product isomerate can then be used in the gasoline blending stock.

3.5.3.6 Naphtha Reforming

The C_{7-10} hydrocarbons from the naphtha hydrotreater and wax hydrocracker are sent to the catalytic reformer in a similar process as isomerization by rearranging the molecular structure of the hydrocarbons, which increases the OR to 90-95. The main reforming reactions are endothermic, and the feed gas is heated to around 480 °C and pressurized to 4 MPa for this reactor [57]. The product of the catalytic reformer, called reformate, has the highest octane rating, and it represents the majority of the gasoline blending stock.

3.5.3.7 Upgrading Quality & Yield

The overall target OR for gasoline of 87-88 can be achieved by these processes. The quality of the diesel blending stock is quantified in terms of the cetane index, which is measure of the ignition speed of the fuel. While the true cetane index is experimentally determined, the product diesel is assumed to have a much higher cetane index than that of conventional diesel, which implies that it has a high product value because it can be used to increase the quality of low grade diesel [45]. Table 3.1 illustrates the yields from these unit operations based on Bechtel [45].

The model in this study uses the yields in Table 3.1 to determine the yield of gasoline and diesel blending stocks. The yields from Bechtel [45] are consistent with the experimentally determined yields from similar processes in conventional oil refineries given in Gary et al. [57]. The LFG produced from these processes is essentially a conversion penalty for increasing the octane and cetane rating to generate high quality liquid fuels. The utilities are also calculated based on Bechtel [45], and these calculations are used to estimate the heat, power, steam, and cooling water required by these processes. The LFG produced from the upgrading processes is used for SOEC feed preheat and supplying utility heat for the upgrading processes themselves. The F-T synthesis reactor produces high pressure (25 bar) steam, and this satisfies the steam requirements for the upgrading processes and contributes a significant amount of steam to the SOEC. Cooling water is provided by a cooling tower water loop.

Table 3.1 Product upgrading yields (molar %) based on Bechtel [45]

	LFG	C_5/C_6	$C_{7\text{-}10}$	$C_{11\text{-}19}$	Isomerate	Reformate
Wax Hydrocracker	6	5	25	65	0	0
Naphtha Hydrotreater	7.9	14.2	77.9	0	0	0
Distillate Hydrotreater	2.5	0	0	97.5	0	0
C_5/C_6 Isomerization	2.0	0	0	0	98.0	0
Catalytic Reformer	14.2	0	0	0	0	85.8

3.6 System Design

Figure 3.12 illustrates the process for syngas generation via co-electrolysis. The CO_2 enters at state-point (1) and is scrubbed of the bulk of the H_2S by a LO-CAT™ oxidation process before being heated and sent to a zinc oxide (ZnO) bed, where it is purified to less than 1 ppm H_2S. The scrubbed CO_2 then mixes with steam and H_2 at state-point (8). This gas mixture is heated to 800 °C by the LFG burner effluent gas stream at state-point (24) before being sent to the cathode of the SOEC unit. Sweep air (16) is first compressed and then heated to about 770°C with the anode effluent in HX-02. The air is then heated to the SOEC operating temperature of 800 °C in HX-03. The SOEC converts the steam and CO_2 into a syngas-rich stream which exits the cathode at state-point (10). Electricity is converted from three-phase AC to DC electric power in the rectifier, thereby providing the dc current that drives the electrochemical reactions in the SOEC.

The main supply of steam for the SOEC at state-point (31) comes from the steam generated in the F-T reactor shown in Figure 3.13. The remaining steam is supplied by water that enters the plant and is heated by cathode effluent recuperation in HX-05. The hydrogen is supplied from excess production downstream by a PSA unit in the F-T synthesis island shown in Figure 3.13. The LFG Burner effluent is used for the following heat exchange processes, in order: cathode pre-heat (HX-04), anode pre-heat (HX-03), ZnO bed pre-heat (HX-01), F-T pre-heat (HX-06), F-T upgrading heat and steam rankine cycle (SRC) supply heat for electricity generation. The cathode effluent is also used as a heat source for the SRC, and the gas is then cooled further for condensing the water out. The syngas is then compressed in a multi-stage compressor to 40 bar and heated in preparation for the F-T reactor.

Figure 3.13 illustrates the process for F-T synthesis and product upgrading to gasoline and diesel fuel products. The distillation and upgrading processes are treated as a black-box for this model; the heating, cooling, and pressurization requirements by these processes are determined by calculating the utilities (electric power, steam, heating fuel, and cooling water) which are scaled from the process results of Bechtel [45]. A small fraction (2%) of the SOEC produced syngas at (1) in Figure 3.13 is diverted to increase the hydrogen content in the PSA feed stream (5). The pressurized and heated syngas is fed to the F-T synthesis reactor, where the syngas is converted to heavier hydrocarbons (C_xH_y) which serve as the primary liquid fuel molecular building blocks.

Nearly all of the fuel refining and upgrading processes downstream of the F-T synthesis reactor produce byproduct LFG. A flash drum reduces the pressure of the cooled F-T reactor effluent at 4000 kPa down to 2600 kPa, which evaporates the majority of the LFG (C_{4-}) for separation from the heavier (C_{5+}) hydrocarbons while maintaining a pressure high enough for the PSA unit. The separated syngas and LFG are first sent to a WGS reactor to convert the majority of the CO (and H_2O) to H_2 for better PSA separation performance. The remaining F-T products are fractionated in an atmospheric distillation tower to separate the remaining light gas (C_{1-4}), naphtha (C_{5-9}), middle distillates (C_{10-19}), and waxes (C_{20+}). The latter three products are fed into the naphtha hydrotreater, the distillate hydrotreater, and the wax hydrocracker, respectively.

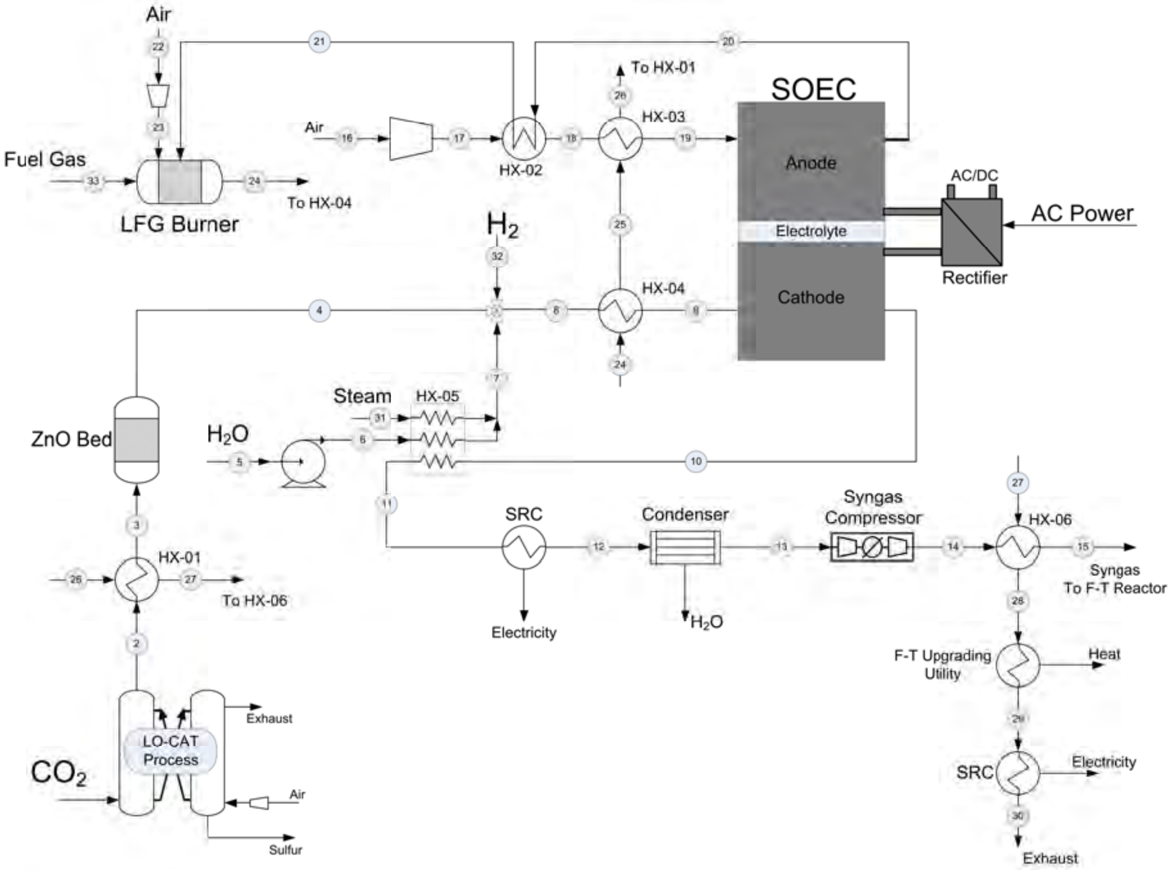

	T (°C)	P (kPa)	$\dot{m}$ (kg/s)
1	20	200	3.88
2	20	190	3.85
3	375	180	3.85
4	375	170	3.85
5	30	100	0.63
6	30	180	0.63
7	600	170	3.02
8	495	170	6.89
9	800	160	6.89
10	800	150	3.75
11	338	140	3.75
12	100	130	3.75
13	30	120	3.05
14	125	4000	3.05
15	240	3990	3.05
16	20	100	4.57
17	97	200	4.57
18	772	190	4.57
19	800	180	4.57
20	800	170	7.71
21	400	160	7.71
22	20	100	7.21
23	75	160	7.21
24	1074	160	16.64
25	902	150	16.64
26	895	140	16.64
27	829	130	16.64
28	790	120	16.64
29	732	110	16.64
30	100	100	16.64
31	225	180	2.38
32	40	170	0.03
33	53	160	1.71

Figure 3.12 Process flow diagram for solid oxide co-electrolysis syngas production

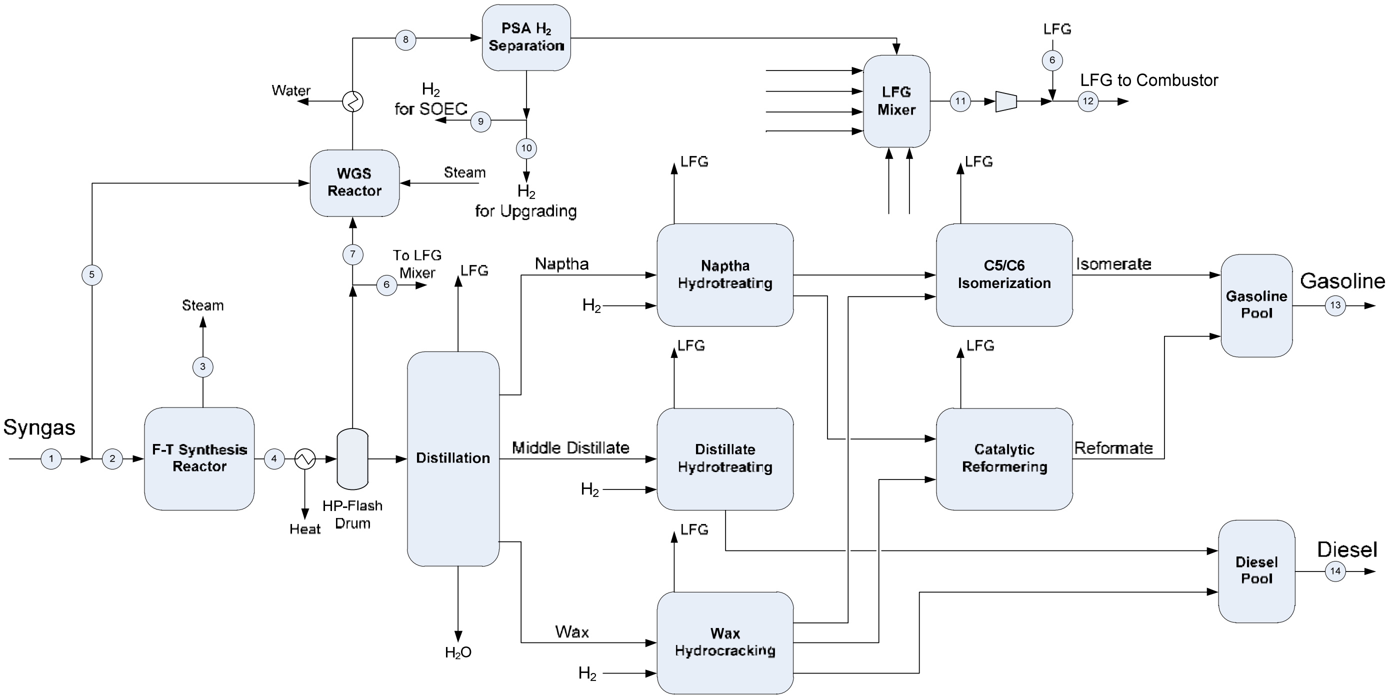

	T (°C)	P (kPa)	$\dot{m}$ (kg/s)
1	240	3990	3.05
2	240	3990	2.99
3	225	2500	2.38
4	240	3890	2.99
5	240	3990	0.06
6	40	2600	1.07
7	40	2600	0.46
8	40	2480	0.73
9	40	2420	0.02
10	40	2420	0.01
11	40	100	0.64
12	53	160	1.71
13	25	100	0.18
14	25	100	0.39

Figure 3.13 Process flow diagram of Fischer-Tropsch synthesis and upgrading island

The lighter naphtha components (C_5/C_6) from the naphtha hydrotreater and the wax hydrocracker are sent to the C_5/C_6 isomerization unit. The heavier naphtha components ($C_{7\text{-}9}$) from these units are sent to the catalytic reformer. The isomerization unit and the catalytic reformer are used to increase the octane number of their hydrocarbon feeds; the products of these two processes are blended in the gasoline pool. The products of the distillate hydrotreater and the middle distillates ($C_{10\text{-}19}$) from the wax hydrocracker are sent directly to the diesel pool. The LFG generated from each of these processes, along with the PSA tail gas, are combined to be combusted for process heating requirements at state-point (34) in Figure 3.12.

3.7 Model Performance Results

Figure 3.14 gives an overview of the net inputs and outputs of the plant. The main energetic input into the plant is about 50 MW of AC electric power. Carbon dioxide is fed into the plant from a pipeline. Process water is required for consumption in SOEC, and cooling water make-up for the cooling tower is also input into the plant.

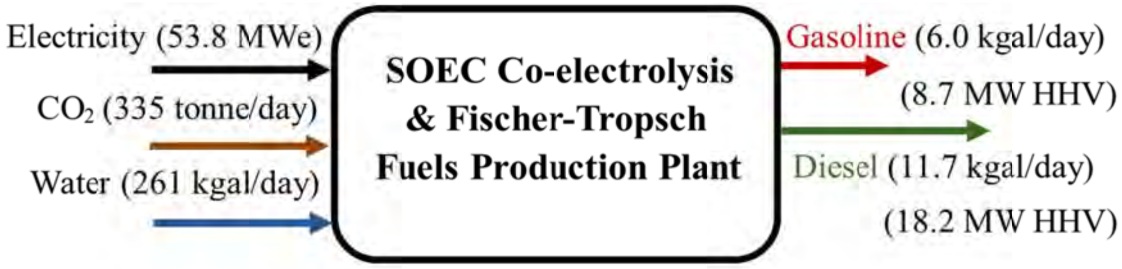

Figure 3.14 Overall plant inputs and outputs

Table 3.2 summarizes the energy balance and liquid fuels production of the plant, including efficiencies of various subsystems. Two operational cases were explored: the SOEC design pressure of 1.6 bar and 5 bar. The results are first discussed in terms of the baseline case of 1.6 bar SOEC operation. The higher pressure case is then discussed relative to the baseline case.

Table 3.2 Energy balance summary

	1.6 Bar	5 Bar
Plant Inputs		
Electricity AC in (kW)	53770	50847
Carbon dioxide (kg/s)	3.88	3.88
Process water (gpm)	48	48
Cooling water (gpm)	133	95
Internal power use (kW)		
SOEC (DC)	50787	49454
Sweep air blower	408	1130
Syngas compressor	3224	1805
Burner air blower	420	547
Other blowers & pumps	110	97
F-T utility	126	117
Steam cycle	-3456	-4337
Total internal power use	51620	48813
Burner heating use (kW)		
Heat loss	500	500
ZnO bed pre-heat	1351	1351
SOEC gas pre-heat	3767	3869
F-T utility	1967	2033
Steam cycle	13822	17348
Plant outputs		
Gasoline (gal/day)	5958	5305
Gasoline HHV (kW)	8686	7735
Diesel (gal/day)	11661	10372
Diesel HHV (kW)	18256	16372
Total output LHV (kW)	24917	22296
Total output HHV (kW)	26942	24107
Efficiency		
SOEC efficiency HHV	110.1%	110.2%
F-T efficiency HHV	45.2%	41.5%
Steam cycle efficiency	25.0%	25.0%
Plant efficiency LHV	46.3%	43.8%
Plant efficiency HHV	50.1%	47.4%

About a third of the LFG produced in the F-T reactor, including unreacted CO and H_2, is needed for the hydrogen production process which serves the hydrotreating and hydrocracking units in the F-T synthesis island and the SOEC cathode feed gas. The remaining LFG, including that which is produced from the upgrading processes, mixes with the hydrogen-depleted PSA effluent and is fed into the burner to supply the pre-heating needs of the SOEC and other processes quantified in Table 3.2. The SOEC feed gas requires about 4 MW of heat, and the temperature at which the burner supplies heat transfer must be above 810 °C to preheat both the cathode and anode feed gases to 800 °C. This high temperature requirement hinders the ability to extract energy from the high pressure LFG flashed from the F-T reactor effluent in a gas turbine; using a gas turbine would lower the temperature too much to adequately supply the pre-heating requirements. The potential benefit of using a gas turbine in this plant is an increased electrical efficiency compared to the steam cycle used for heat recovery power production.

While the F-T upgrading heat utility temperature requirement was not specified by Bechtel [45], it was conservatively assumed that this heating power utility could be satisfied at a temperature of around 750 °C (oil refinery upgrading processes do not typically exceed 500 °C [57]). The large amount of remaining heat (~14MW) was supplied to the steam cycle at about 700 °C.

The plant produces about 6,000 gal/day (~8.7 MW HHV) of gasoline and about 11,700 gal/day (~18.3 MW HHV) of diesel. The plant produces a little over twice as much diesel as gasoline with a total production of about 17,700 gal/day (27 MW HHV). The SOEC efficiency (Equation (3.20)) takes into account the change of the cathode gas heating value on an HHV basis and the electricity requirement for driving the electrochemical reactions.

$$\eta_{SOEC} = \frac{HHV_{syngas} - HHV_{cath,in}}{P_{SOEC,DC}} \tag{3.20}$$

The resulting efficiency is 110% because the reverse WGS reaction raises the heating value of the product syngas (a byproduct of the energy input into heating the gases to 800

°C) in addition to the electrochemical conversion. The heating value of the cathode feed gas is from its hydrogen content.

Alternatively, the SOEC efficiency can be described by a 2nd law analysis; the 2nd law efficiency for the SOEC (Equation (3.21)) results in 88.6%. This efficiency is much lower because it captures the available work potential from the high temperatures of the feed gas, which is not accounted for in the energetic efficiency from Equation 3.20.

$$\eta_{SOEC,II} = \frac{\dot{A}_{syngas} - \dot{A}_{cath,in}}{P_{SOEC,DC}} \tag{3.21}$$

The F-T efficiency (Equation (3.23)) takes into account the heating value of the liquid fuels on a HHV basis and the syngas that feeds the F-T synthesis reactor.

$$\eta_{F-T} = \frac{HHV_{liquid\,fuels}}{HHV_{syngas}} \tag{3.22}$$

The definitions of the two major subsystem efficiencies (Equations (3.20) and (3.22)) do not take into account the LFG produced from the F-T process, which is used for SOEC feed gas heating; this inherently decreases the F-T efficiency and increases the SOEC efficiency. The subsystem efficiency definitions will allow for a comparison of the relative performances of the two cases presented (low versus high pressure).

Table 3.3 gives the breakdown of the utilities calculations for the F-T synthesis and upgrading processes. The power requirement for these processes consists of small compressors, blowers, and pumps, and this is a relatively small contribution to the total electric power needs of the plant. The F-T synthesis reactor produces a large quantity of 25 bar steam at 225 °C which satisfies the other process steam requirements and supplies 75% of the SOEC steam needed for co-electrolysis. The heating load calculations are consistent with the conventional operating conditions of each process, described earlier. The majority of the cooling water requirement is for cooling the F-T effluent down to 40 °C to flash out the light gases.

Table 3.3 F-T synthesis and upgrading utilities consumption

	Power	Steam[a]	Heat[b]	Cooling Water
Units	kW	klb/hr	kW	gpm
F-T Pre-heat	0	0	798	0
F-T Synthesis Reactor	47	-22.3	299	14.3
F-T Product Flash HX	0	0	0	906.0
Distillation	4	0	106	5.0
H_2 Production	0	1.8	0	64.3
Wax Hydrocracker	14	1.9	179	1.5
Distillate Hydrotreater	21	0	66	3.6
Naphtha Hydrotreater	8	0	183	31.2
Catalytic Reformer	31	-0.2	330	7.7
C_5/C_6 Isomerization	1	0.03	6	0.4
Total	126	-18.9	1967	1033.9

[a] Steam produced and consumed at 225 °C and 24 bar

[b] Temperature of heat source varies, but all processes are conservatively assumed to be satisfied by a heat source of greater than 700°C.

The steam cycle efficiency (Equation (3.23)) accounts for the electricity generation and the heat extracted from lowering the cathode effluent and burner gas stream from 700 °C to 100 °C.

$$\eta_{steam\ cycle} = \frac{P_{steam\ cycle}}{Heat_{in}} \tag{3.23}$$

The steam cycle efficiency is estimated to be 25%, so this designates the electricity produced based on the heat input. It should be noted that the heat recovery calculation from lowering the gas stream temperature to 100 °C is optimistic for producing steam. Lowering the gas down to 135 °C is a more conservative value, and this would lead to a 220 kW decrease in SRC power production (drop of 0.2% in overall efficiency). The SRC efficiency would have to increase to 26.5% to make up for the difference in available heat.

The total plant efficiency (Equation (3.24)) accounts for the only energetic input and output of the plant: the net power required and the heating value of the liquid fuels on an HHV basis.

$$\eta_{plant} = \frac{HHV_{liquid\,fuels}}{P_{in}} \tag{3.24}$$

The total plant efficiency is 46.3% based on the LHV and 50.1% based on the HHV of the liquid fuels.

The plant was then run with an SOEC operating pressure of 5 bar. Several minor adjustments to the plant were made to maintain various constraints on the system (e.g. increased burner air intake to limit the exhaust temperature due to the increased heating value of the LFG), but no other major operational changes were made. The higher pressure operation case demonstrates the various synergies between the syngas production and F-T liquid fuels production subsystems. The net electricity consumption drops significantly (~3MW) from the baseline case for several reasons. The required SOEC voltage for thermal neutral operation decreases from 1.34 to 1.31; this equates to about a 1.5 MW reduction for the same oxygen utilization. The lower thermal neutral voltage is caused by the additional exotherm from a higher extent of the methanation reaction (Equation (3.4)); while this increases the electrical efficiency of the SOEC, the methane is not a desired product for an F-T synthesis reactor.

There are various trade-offs in compression power for the high pressure SOEC case: while the syngas compression is lower, the anode sweep air and burner air compression increase. There is more recoverable heat for the steam cycle which produces about 1 MW of additional power. The net result is an additional 1.5 MW of electric power savings (along with the 1.5 MW reduction for the SOEC) over the baseline case.

The decrease in electric power consumption for the high pressure case is offset by the decrease in liquid fuel production. The high pressure case produces 2.8 MW (HHV) less liquid fuels than the baseline case due to the presence of additional methane in the syngas, which detracts from the convertible syngas content. The SOEC efficiency is slightly higher for the 5 bar operation mainly because of the decrease in operating voltage for isothermal operation. The 2nd law efficiency for the SOEC operating at 5 bar is 89.2%, and this is a 0.6% increase from the low pressure operation. The F-T efficiency is much lower (41.5% versus 45.2%) due to the decrease in convertible syngas feeding the

F-T reactor. The overall plant efficiency is lower for the 5 bar operation by 2.7%; the lower F-T conversion efficiency over-compensates for the slightly higher SOEC efficiency.

3.8 Economics

The economics of liquid fuels production plant is evaluated to determine the value of the liquid fuel products. The capital investment of the plant must first be determined. The subsystems of the plant include carbon dioxide clean-up, syngas production via SOEC co-electrolysis, heat recovery, balance-of-plant including air blowers, water pumps and a cooling tower, syngas compression, F-T synthesis, hydrogen recovery, and product upgrading.

3.8.1 Capital Investment

The same cost scaling method from Chapter 2 is used for many of the plant components, and AspenTech *Economic Analyzer*™ is used for others. In comparison to large crude oil refineries, the liquid fuels plant in this study is quite small; many of the referenced base costs for F-T synthesis and upgrading components are much larger than the size of this plant, and the economics are less favorable due to the scaling factor. Table 3.4 gives the component cost breakdown of the plant. It is noted that this costing methodology results in an accuracy of ±30%.

It is convenient to compare the total capital investment to an equivalent Lang Factor (e.g. 4.7-5.9 for chemical processing plants [31]) which is an order-of-magnitude plant cost estimation using the ratio of TCI to total purchased (uninstalled) equipment cost (TPEC) of the plant components. Assuming a single installation factor of 2.47 from Spath et al. [29] to backtrack the TPEC from the TIC in Table 3.4, the resulting Lang Factor is 4.2. Because of the variety of references used to determine the direct capital investment and the differing methods that were used by these references to determine the costs, it is difficult to know the TPEC exactly. The main reason for the calculated Lang Factor being less than that of conventional chemical processing plants is the high cost of the SOEC. Since the Lang Factor method assumes a plant cost from conventional TPEC, a high TPEC will result in a relatively low Lang Factor.

Table 3.4 Cost of system components in MM$\$_{2009}$

	C_o[a]	S_o	n	IF[b]	BOP[c]	TIC[d]
CO_2 Clean-up						
LO-CAT™[e]	1.32	22.6 kg/s	0.65	2.47	-	1.04
ZnO Bed[e]	0.049	22.6 kg/s	0.56	2.47	-	0.04
Syngas Production						
SOEC & Rectifier[f]	0.00053	\$/kW	-	1.42	-	38.68
Heat Recovery						
Burner[g]	-	-	-	-	-	4.99
Heat Exchangers[g]	-	-	-	-	-	4.24
Steam Cycle[h]	6.85	10.30 MW	0.7	2	-	3.28
Balance of Plant						
Blowers & Pumps[g]	-	-	-	-	-	1.36
Cooling Tower[g]	-	-	-	-	-	0.43
F-T Synthesis						
Syngas Compressor[g]	-	-	-	-	-	3.78
F-T Reactor[h]	42.37	362 m^3	0.72	-	-	2.90
H_2 Recovery						
WGS Reactor[h]	14.12	245 mol-H_2/s	0.65	1.81	-	1.11
PSA[i]	0.84	0.24 m^3/s	0.7	-	0.27	1.37
Product Upgrading						
Distillation[i]	0.73	1.82 kg/s	0.7	-	0.09	0.45
Wax Hydrocracker[i]	9.37	1.13 kg/s	0.7	-	0.84	4.18
Distillate Hydrotreater[i]	2.51	0.36 kg/s	0.7	-	0.47	2.34
Naphtha Hydrotreater[i]	0.75	0.26 kg/s	0.7	-	0.12	0.62
Catalytic Reformer[i]	5.22	0.43 kg/s	0.7	-	0.68	3.42
C_5/C_6 Isomerization[i]	0.96	0.15 kg/s	0.7	-	0.11	0.54
Total Installed Cost[j]						74.78
Total Direct Cost[k]						83.76

[a] These base costs have been scaled from the original cost index ($CEPCI_o$) to the 2009 CEPCI (521.9)

[b] The installed factor (IF) is only used if the base cost (C_0) does not include installation (otherwise it's 1).

[c] An additional balance of plant (BOP) cost of 25% of the installed cost is used for the F-T synthesis and upgrading components from Larson et al. [9].

[d] The total installed cost (TIC) is the sum of the IC and the BOP (where applicable).

[e] Spath et al. [29]: an installation factor of 2.47 is referenced.

[f] Gerdes et al. [58]: the cost of SOEC module of 400 $\$_{2002}$/kW uninstalled is based on DOE cost target for SOFC systems including rectifier and controls; this amounts to 750 $\$_{2009}$/kW installed. An installation factor of 1.42 is also referenced.

Table 3.4: continued

[g] AspenTech *Economic Analyzer*™ software is used to calculate the installed cost of a high temperature burner based on heating duty and flow rate, floating head shell and tube heat exchangers based on heat transfer area (heat transfer coefficients calculated from Peters et al. [31]) and materials suitable for the operating temperature (inconel was used for high temperature (>700 °C) operation), blowers and pumps based on flow rates and design pressure, cooling tower based on water flow rate and temperature approach to wet bulb, and a multi-stage centrifugal compressor with intercooling based on number of stages, pressure ratio and cooling requirements.

[h] Hamelinck et al. [44]: the steam cycle includes steam turbine, condenser, cooling, and system BOP. The size of system is based on turbine power. The F-T reactor volume was determined from Equation 17.

[i] Cost estimate based on Larson et al. [9] does not include balance of plant for the individual processes; a BOP cost of 25% of the initial IC was added to determine the TIC of these components.

[j] The TIC of the plant components is not inclusive of buildings and service facilities for the entire plant

[k] A factor of 12% (8.97 MM$) of the TIC is added to account for these attributes referenced from Spath et al. [29]. This addition makes the total direct costs (TDC) equal to 83.76 MM$.

In addition to direct costs, the indirect costs shown in Table 3.5 include engineering and design, plant construction, legal and contractors fees, and project contingencies; these costs were estimated to be 51% (42.7 MM$) of the direct capital costs, bringing the total capital investment up to 126.5 MM$$_{2009}$.

Table 3.5 Indirect costs allocated as a percentage of TDC from Spath et al. [29] and actual costs for this plant

	% of TDC	MM$
Engineering & design	13	10.9
Construction	14	11.7
Legal and contractors fees	9	7.5
Project contingency	15	12.6
Total Indirect Costs	51	42.7

3.8.2 Operating & Maintenance Costs

The operating costs for the plant were estimated in two ways: the SOEC operating, maintenance, and replacement costs were estimated based on Gerdes et al. [58]

to be 0.22 ¢/kWh, and the remaining operating and maintenance costs were estimated to be 5% of the direct capital costs, excluding the SOEC unit; the latter costs account for catalyst replacement for the reactors and general maintenance of all plant components. The annual labor and overhead costs include two plant operations workers and a supervisor for each shift (3 shifts in a day), and this amounts to 1.25 MM$. Property tax and insurance are estimated to be 2% of the TCI (2.53 MM$). These estimations are consistent with the H2A analysis tool default values and H2A analysis case studies for similar sized electrolysis plants [42]. The total operating and maintenance costs amount to 5.89 MM$ (8.8% of the TIC) per year.

3.8.3 H2A Life Cycle Analysis

The total capital investment (direct and indirect) for the plant is an input for the H2A life cycle analysis tool [42], which is used to generate a levelized cost of liquid fuels. The Various economic parameters specified for the H2A program are summarized in Table 3.6.

3.8.4 Feedstock Costs

In addition to electricity required by the plant, the carbon dioxide must also be purchased from a supplier. In the case of the Weyburn Project for EOR, the GPSP captures carbon dioxide and sells it for approximately 15 $/tonne [59]. This value is used as the CO_2 feedstock cost for this study. The electricity feedstock cost and the plant operating capacity factor are varied to determine the effects of renewable sources of electricity on the liquid fuels production costs.

3.8.5 Liquid Fuels Production Cost Sensitivity

A breakdown of cost contributions to the total cost of the liquid fuel produced by the plant, based on gallon of gasoline equivalent (GGE) with a higher heating value of 131.2 MJ/gal, is given in Figure 3.15. Since the plant produces gasoline and diesel fuels, the combined power flow (MW) of the fuels was converted to the GGE of conventional gasoline for comparison the market competition.

Table 3.6 Economic inputs to the H2A tool

	Value
Constant dollar value	2005
Internal rate of return (after-tax)	10%
Debt/Equity	0%/100%
Plant life	40 years
Depreciation	MACRS
Depreciation Recovery period	20 years
Construction period	2 years
1st year	75%
2nd year	25%
Start-up time	12 months
Revenues	50%
Variable costs	75%
Fixed costs	100%
Working capital	15% of total capital investment
Inflation rate	1.90%
Total taxes	38.90%
Decommissioning costs	10% of depreciable capital
Salvage value	10% of total capital investment
CO_2 feedstock cost	\$15/tonne
Electricity feedstock cost	Varied
Plant capacity factor	Varied

The operating capacity factor is defined as the percentage of time the plant operates at its maximum capacity. This value depends largely on the source of the electricity, and the effects of this factor on the production cost gives insight into the challenges of powering the plant using an intermittent source of electricity, such as wind. The electricity feedstock has the largest cost contribution for high capacity factors, representing 49% and 33% of the total cost for capacity factors of 90% and 40%, respectively. The capital costs become the most significant as the plant capacity factor decreases, representing 52% and 36% for capacity factors of 40% and 90% respectively. It should be noted that using electricity feedstock costs of greater than 0.06 \$/kWh, the electricity cost contribution can represent a larger fraction of the total cost than the capital costs, even at low capacity factors. The O&M costs contribute about 12% to the total cost, and it decreases proportionally with capacity factor because the SOEC stacks will not have to be replaced as often. The carbon dioxide feedstock cost is constant at 15 $/tonne (or 0.30 $/GGE), representing just 3% of the total cost, and its purchase price is assumed to not have a quantity or volume basis.

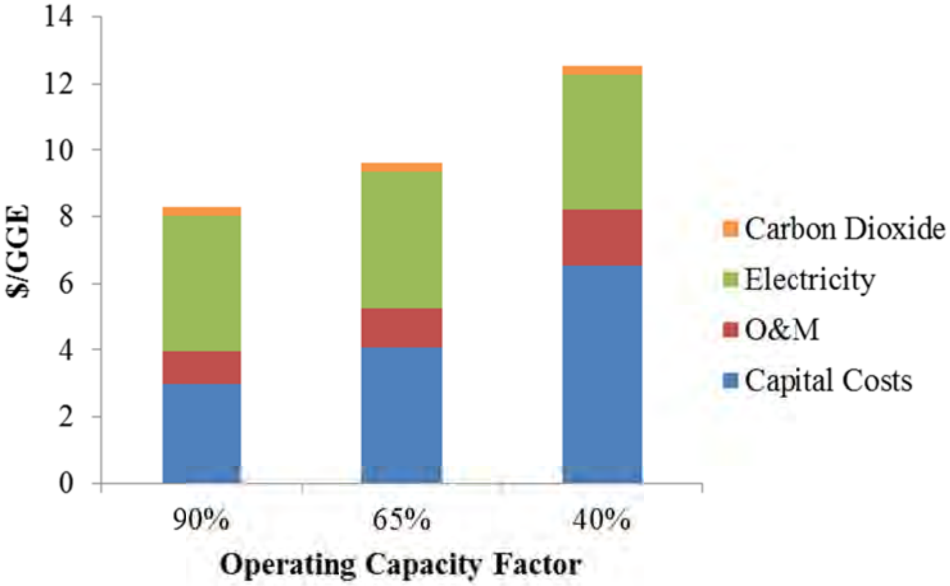

Figure 3.15 Cost contribution to liquid fuels production for an electricity feedstock cost of 0.06 $/kWh at various capacity factors

The cost of liquid fuels is linearly dependent on the electricity feedstock cost, as shown in Figure 3.16. The most optimistic capacity factor of 90% results in a fuel cost of 5.5 $/GGE for the very low electricity cost of 0.02 $/kWh. For a capacity factor of 40%, the fuel cost is 9.8 $/GGE for the electricity rate of 0.02 $/kWh. For a more realistic goal of renewably generated electricity at a cost of 0.08 $/kWh, the liquid fuel cost ranges from 9.7 $/GGE to 14.0 $/GGE for a capacity factor of 90% and 40%, respectively. For every 0.01 $/kWh of electricity feedstock cost, the cost of liquid fuels production increases about 0.7 $/GGE.

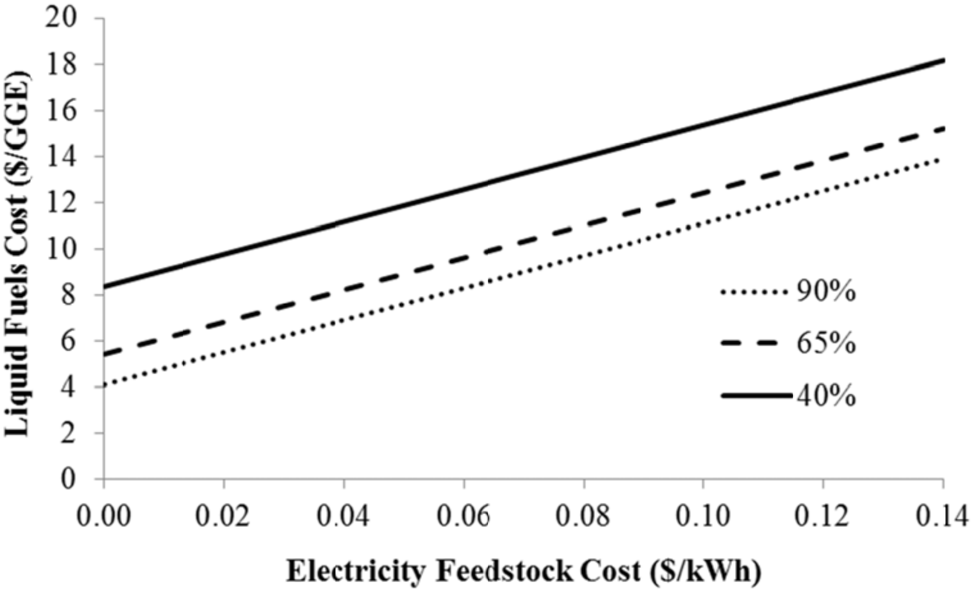

Figure 3.16 Cost of GGE production dependency on electricity feedstock cost for various capacity factors

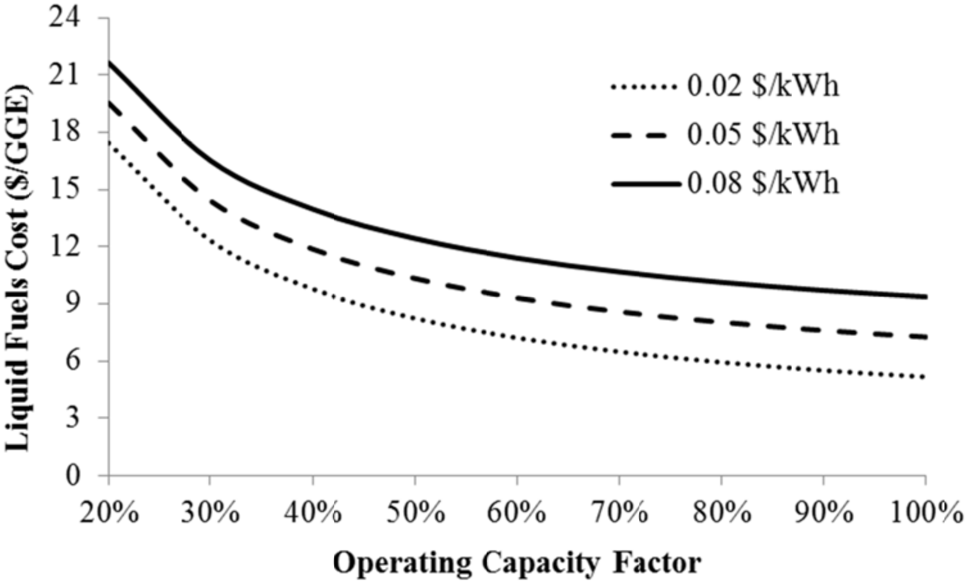

Figure 3.17 Cost of GGE production dependency on capacity factor for various electricity feedstock costs

The cost of liquid fuels is non-linear with respect to operating capacity, and the cost quickly rises below a capacity of 50%, as shown in Figure 3.17. Operating capacity clearly has a large influence on the cost of liquid fuels production, and this parameter will be affected by how the system is sized in relation to the electricity available. Assuming the power is generated from wind, the capacity factor would be higher if the wind farm maximum capacity was much larger than the production plant. Although the local weather conditions would affect all of the wind turbines, a wind farm which spans a large geographic area could supply the fuels production plant with its maximum electricity feedstock capacity. Alternatively, having multiple local sources of renewable electricity (wind, solar, geothermal, hydro, etc.) could provide a continuous supply.

If the plant is only being supplied electricity from a wind farm, the capacity factor would be around 40-50% for the same reasons given in Chapter 2. The capacity factor has a larger impact on fuel production cost than the SNG plant because the capital investment is proportionally higher; this emphasizes the importance of obtaining a relatively constant source of electricity, and it exemplifies the disadvantage of relying on an intermittent source of electricity, such as wind power.

3.9 Summary & Conclusions

A thermochemical model for the conversion of SOEC derived syngas to liquid fuels via F-T synthesis and upgrading was presented. The model gives insight into the synergies between the syngas production and liquid fuel synthesis subsystems. The performance model for the SOEC co-electrolysis process was based on experimental data from Stoots et al. [46], and the model was extended to account for the methanation reaction at elevated operating pressures based on findings from Timmermann et al [47]. The F-T synthesis reactor operating conditions, reactant conversion, and product yield distribution represent realistic industrial scale performance. The upgrading process yields and conversions for the various unit operations agree well with multiple sources, including experimental correlations. The plant produces about 6,000 gal/day (~8.7 MW HHV) of gasoline and about 11,700 gal/day (~18.3 MW HHV) of diesel. The system model results in an overall electricity-to-liquid fuels efficiency of 50.1% HHV (46.3%

LHV). This efficiency is significantly lower than the 70% estimated by Graves et al. [10], but the model in this study is representative of a more detailed and complete fuel production process. The scenario of operating the SOEC at 5 bar results in an overall efficiency that is 2.7% lower than operation at 1.6 bar.

The economics of this process were evaluated for various electricity feedstock costs and operating capacity factors, which is important to explore the effects of producing liquid fuels from renewable sources of energy. The liquid fuels production costs range from 5.8 $/GGE to 18.2 $/GGE for an electricity feedstock price of 0.02 $/kWh to 0.14$/kWh and a capacity factor of 90% to 40%, respectively. For every 0.01 $/kWh of electricity feedstock cost, the cost of liquid fuels production increases about 0.7 $/GGE. It is crucial for the economics of liquid fuels production to have the highest operating capacity possible, and this will be a major challenge to using renewable technologies such as wind and solar

CHAPTER 4

HYDROGEN PRODUCTION FROM SOLID OXIDE FUEL CELL POLYGENERATION

Distributed energy generation improves the integration of renewable and higher efficiency generators into the energy infrastructure. Solid oxide fuel cell (SOFC) systems can be fueled by natural gas to produce electric power, and they exhibit high overall efficiency when co-generation is used. Co-generation studies have typically focused on electricity and heat; pure hydrogen gas can also be generated in these systems as an energy co-product resulting in the combined production of heat, hydrogen, and power (CHHP).

Co-locating a distributed generation SOFC CHHP plant with hydrogen fueling stations for fuel cell vehicles enables use of lower-scale (~250 kg/day) hydrogen production and leverages the capital investment across all co-products, which lowers the unit cost of hydrogen and offers a potentially promising transition pathway for the FCV market.

With respect to carbon dioxide emissions from fossil fuels, natural gas is one of the cleanest to combust. At present, the resource most readily available for fueling an SOFC system is natural gas; this fuel, modeled as pure methane, is chosen for the SOFC fuel in this study.

4.1 Prior Work

There are several studies which have examined the co-production of hydrogen in addition to power and heat from SOFC systems. Mitlitsky [60] performed a study integrating an SOFC module with an electrochemical hydrogen separation (EHS) unit. Although this study employed a smaller-scale system (25 kWe AC SOFC with a maximum hydrogen production of 19 kg/day) than the system in the present study, the

EHS units are scalable in the same manner as fuel cells. In fact, the EHS performance is predicted to improve with increased size [60]. The product hydrogen gas is intended for use in low-temperature PEM fuel cells, so the limit of CO in the hydrogen stream is in the range of 1-2 ppmv. The EHS unit in Mitlitsky [60] demonstrated a 2600:1 reduction of CO in the product stream, which would purify the hydrogen from a feed CO content of 0.5% down to 1-2 ppmv.

Perdikaris et al. [61] examined the tri-generation of heat, hydrogen and power by using a combination of an SOFC and a solid oxide electrolyzer cell (SOEC). The methane-fueled SOFC provided electricity and heat to the SOEC for hydrogen production, and the SOFC tail-gas was combusted with the oxygen-enriched sweep gas of the SOEC for heat recovery. The operation and control of such a system would be difficult due to the inherent feedback and dependence between the two subsystems.

Colella et al. [62] studied an SOFC CHHP system using a PSA unit for hydrogen recovery. It was found that 1 MW systems could produce from 150 to 450 kg/day of hydrogen, and the quantity was found to be sensitive to heat integration of the SOFC system. Heat recuperation of the SOFC tail gas to the inlet gas streams is important for minimizing the required heat duty from burning the tail gas, which lowers the available hydrogen for recovery. The PSA unit was assumed to accomplish 85% separation of the hydrogen in the SOFC tail gas which contains 34% hydrogen after use of a water gas shift reactor; this assumption is found to be invalid for economical operation of the PSA unit due to the low hydrogen composition [29]. The actual cost of hydrogen produced from the SOFC CHHP system was not analyzed.

In this chapter, the SOFC system performance and operation is described. The two technologies for hydrogen separation are then explained and their relative performance in relation to the SOFC tail-gas is compared. The system design, inclusive of the remaining balance of plant operation and performance, is next described. The model results and discussion are given for two design concepts which are differentiated by the method in which they purify the SOFC tail-gas: (1) SOFC integrated with EHS and (2) SOFC integrated with PSA. An operational variation of producing excess hydrogen for both concepts is then presented. The economics of producing hydrogen from the recommended system concept are given with a sensitivity analysis of the hydrogen production cost dependence on the methane feedstock and the electricity credit price.

4.2 Solid Oxide Fuel Cells

SOFC modules electrochemically combust fuel at high temperatures (650-1000 °C) to generate electric power. Hydrogen is the reacting fuel for the SOFC anode electrode, but the hydrogen can be produced by reforming natural gas (mainly methane). This reforming can take place external to the SOFC or inside of the anode; the high temperature operation allows the endothermic reforming reaction to readily occur inside the stack. Air is fed through the cathode electrode, from which oxygen electrochemically reduces to O^{2-} and is transported through the electrolyte to the anode. This process is shown in Figure 4.1. The O^{2-} oxidizes a hydrogen molecule at the anode, which releases electrons for current flow. There is an associated voltage with the current flow through the load (shown as a resistor in Figure 4.1), and this is dependent on the performance characteristic of the SOFC which determines the amount of total electric power that is produced for an amount of fuel that is consumed. The details of the SOFC performance model are given later in this chapter.

The SOFC is modeled as a black-box component (zero-dimensional model) and designed to operate at a chosen temperature, voltage and fuel utilization. Modeling parameters for the SOFC performance are chosen from the literature (model modified from Lisbona et al. [63]). The fuel cell operating conditions are modeled based on the average temperature and fuel composition of the inlet and outlet. The nominal operating temperature of the stack is about 725 °C with a per-pass fuel utilization of 62.5%. The polarization curve is calculated from:

$$V = OCV - \eta_{act} - \eta_{ohm} - \eta_{conc} \tag{4.1}$$

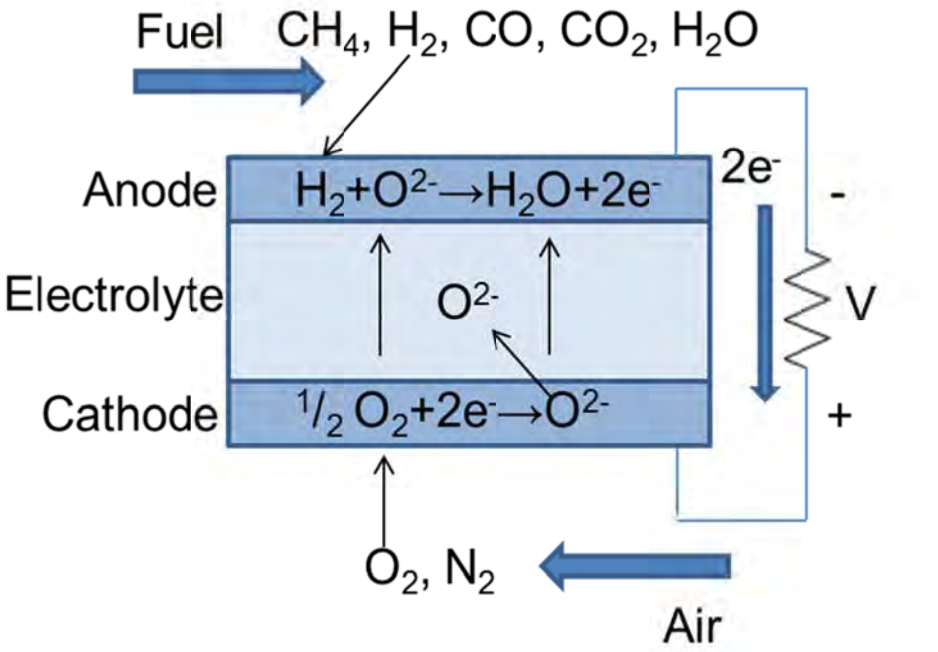

Figure 4.1 SOFC cell operation

The OCV is the open circuit voltage, and the η terms are the activation, ohmic and concentration losses described below. The OCV takes into account the temperature and composition dependence of the Nernst voltage (Equation (4.2)), as well as the deviation of the experimental OCV from theory.

$$E = E_o + \frac{RT}{nF} ln\left[\frac{P_{H_2}P_{O_2}^{0.5}}{P_{H_2O}P_{atm}^{0.5}}\right] \tag{4.2}$$

$$E_o = 1.2723 - 2.7645 * 10^{-4}T, \tag{4.3}$$

In Equation (4.2) n is the number of electrons transferred for each mole of hydrogen (2) and F is Faradays constant (96485 J/mol). The deviation of the experimental OCV from the Nernst voltage is accounted for by Equation (4.4).

$$\theta = \frac{OCV_{exp}}{E} \tag{4.4}$$

θ accounts for electronic and ionic conductivity of the electrolyte at open circuit conditions. This factor is approximated to be 0.94 based on Costamagna et al. [64]. The activation polarization, η_{act}, is determined from the Butler-Volmer (B-V) equation:

$$j = j_o \left[\exp\left(\alpha \frac{nF}{RT} \eta_{act}\right) - exp\left(-(1-\alpha) \frac{nF}{RT} \eta_{act}\right)\right] \tag{4.5}$$

where α is the charge transfer coefficient,

$$j_{o,c} = \gamma_c \left(\frac{P_{O_2}}{P_{atm}}\right)^{0.25} exp\left(-\frac{E_{act,c}}{RT}\right), \tag{4.6}$$

$$j_{o,a} = \gamma_a \left(\frac{P_{H_2}}{P_{atm}}\right)\left(\frac{P_{H_2O}}{P_{atm}}\right) exp\left(-\frac{E_{act,a}}{RT}\right), \tag{4.7}$$

γ is an activation overpotential factor and E_{act} is the activation energy; these values are obtained from Costamagna et al. [65]. The charge transfer coefficient, α, typically ranges from 0.2-0.5 [66]. For “symmetric” reactions (a typical assumption made for SOFC kinetic behavior), the chemical and electrical energy form equal activation barriers for the forward and reverse reactions, so $\alpha = 0.5$; this simplification is used to reduce the B-V Equation (4.5) to:

$$j = 2 j_o sinh\left(\frac{nF}{2RT} \eta_{act}\right) \tag{4.8}$$

The ohmic loss term, η_{ohm}, is dependent on both the resistivity of the stack components and the membrane thicknesses. An area specific resistance can be used as an approximation for this dependence, as given by Equation (4.9).

$$\eta_{ohm} = jASR_{ohm} \tag{4.9}$$

ASR_{ohmic} is the ohmic area specific resistance estimated from O’Hayre et al. [66] to be 0.04 Ω-cm^2. The concentration losses, η_{conc}, is determined by the limiting current density in the following relationship:

$$\eta_{conc} = \frac{RT}{nF} ln\left(1 - \frac{j}{j_L}\right) \tag{4.10}$$

where j_L is the limiting current density and is estimated to be 1.6 A/cm^2 at 800 °C from Lisbona et al. [63].

Figure 4.2 illustrates the polarization curve for the modeled fuel cell operating at an average temperature of 725 °C, atmospheric pressure, fuel utilization of 62.5% and an average composition of 50% H_2, 42% H_2O at the anode and 18.4% O_2 at the cathode.

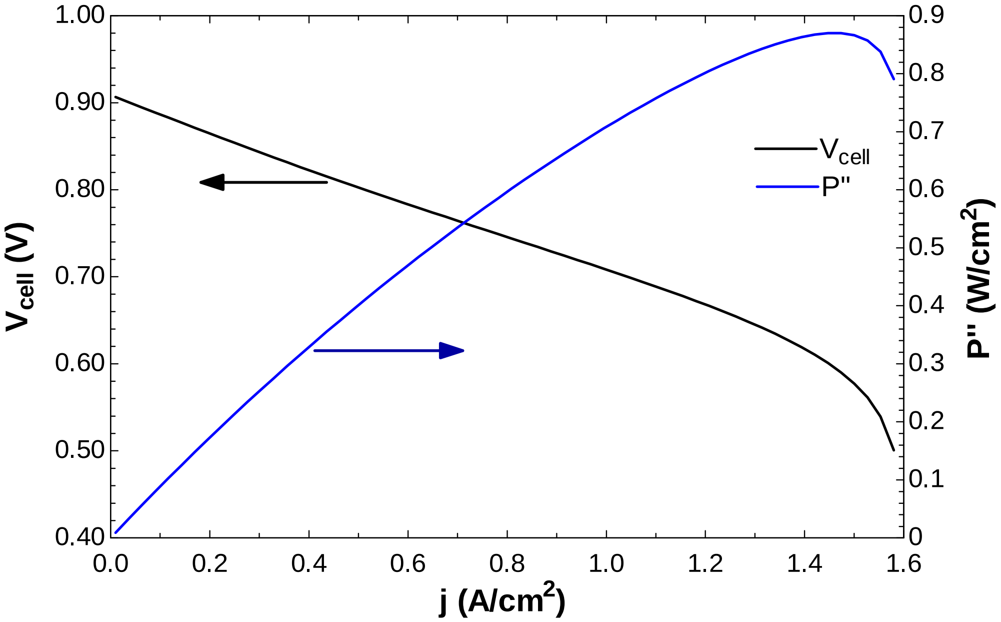

Figure 4.2 SOFC polarization curve and power density for average temperature of 725 °C, atmospheric pressure, and average composition of 50% H_2, 42% H_2O at the anode and 18.4% O_2 at the cathode

The nominal, single cell voltage of 0.78 volts is chosen so that the stack operates at a power density of about 0.5 W/cm^2, which is an achievable performance for a methane-fueled SOFC. This chosen voltage corresponds to a current density of about 0.6 A/cm^2 based on the polarization curve of Figure 4.2. The SOFC stack is sized and designed to operate at this nominal, single cell voltage while generating 1 MWe AC net power. Large-scale planar SOFC stacks are expected to employ cell areas as high as 625 cm^2 [69]. Based on the design voltage and the nominal power output (P_{DC}) , the size and number of stacks can be calculated:

$$P_{DC} = jA_{tot}V \tag{4.11}$$

where P_{DC} is near 1200 kWe DC to generate 1 MWe AC net power (due to internal power needs), j is determined from the modeled polarization curve and operating voltage, and A_{tot} is the total active area of the cells.

Single cell performance is extrapolated to represent the SOFC stack. The number of cells and stacks can be determined as follows:

$$N_{cells} = \frac{A_{tot}}{A_{cell}} \tag{4.12}$$

$$N_{stacks} = \frac{N_{cells}}{Cells\ per\ stack} \tag{4.13}$$

The purpose of the SOFC model is to generate the expected stack performance characteristics and its associated sensitivity to temperature, pressure, and compositional variations in the reactant feed gases. The actual size of the stack can be calculated from the model based on physical dimensions of the stack components. Table 4.1 shows the SOFC operating parameters of this model and a possible stack sizing calculation.

Table 4.1 SOFC Operating Conditions and Stack Sizing Scenario

	Value
T (°C)	727
U_f	0.62
V (V)	0.78
j (A/cm^2)	0.62
P'' (W/cm^2)	0.48
A_{cell} (cm^2)	625
Cells per Stack	200
N_{cells}	3991
N_{stacks}	20

The power density of each cell is 0.48 W/cm^2 based on the polarization curve and design voltage. The stack sizing scenario results in a gross dc power per stack of 60 kW, which requires 20 stacks to produce the 1200 kWe of dc power demanded by the plant.

4.3 Hydrogen Separation

Hydrogen separation units are placed downstream of the SOFC module. Two separation methods are considered: electrochemical hydrogen separation and pressure swing adsorption.

4.3.1 Electrochemical hydrogen separation (Concept 1)

Electrochemical hydrogen separation (EHS) uses electrolytic cells in which an applied voltage drives hydrogen to oxidize to H^+ at the anode, diffuse through the electrolyte membrane, and reduce back to H_2 at the cathode. Figure 4.3 illustrates the separation mechanism.

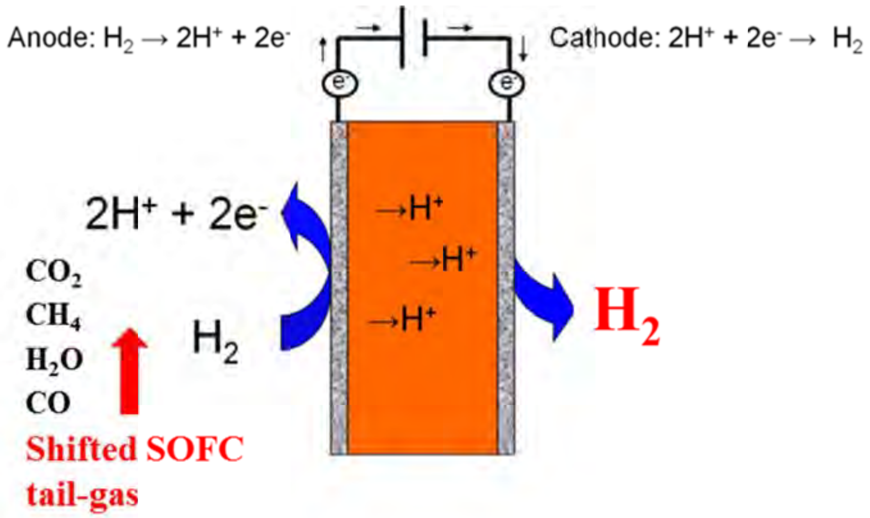

Figure 4.3 Electrochemical hydrogen separation membrane showing electrode half reactions, electron conduction, and proton diffusion through the electrolyte

The result is a hydrogen gas stream exiting the cathode. This process has been shown to be suitable for methane reformate gas streams with a high degree of separation, high purity hydrogen, and relatively small power requirements [70]. PEM electrolytic cells using polybenzimidazole (PBI) doped membranes operate at temperatures of 160-200 °C and are able to tolerate levels of CO up to around 1.5 %, which is above the CO content in typical water-gas shifted anode effluent gas streams. Although the presence of CO can still hinder the performance of the cell due to poisoning, operating at higher temperatures (up to 200 °C) reduces the poisoning effect, and sustained (4000 hours) performance has been demonstrated by Perry et al. [71].

One issue associated with EHS technology is membrane crossover of CO and CO_2 which reduces the hydrogen purity at the cathode. Depending on the catalyst used in the PBI separation unit, the water gas shift reaction could occur at these low temperatures which could further reduce the CO content in the anode. According to one manufacturer (Eisman et al. [72]), a CO reduction of 10,000:1 can be realized which would purify the hydrogen gas to the necessary limit of under 1 ppmv; an experimental evaluation of this system was tested by Mitlitsky [60] using an anode effluent gas stream, and a 2600:1 reduction of CO was achieved. The gas stream from which hydrogen was separated contained less than 30% hydrogen, and an overpotential of 0.08 V was required to achieve 90% hydrogen separation. The CO_2 from the shifted anode effluent also has the potential to cross-over the electrolyte to the hydrogen stream at the cathode, and a 1000:1 reduction was found by Mitlitsky [60]. This amount of CO_2 cross-over reduction would not purify the hydrogen stream to 99.9999% at the cathode, which is the desired purity for PEM fuel cells. It is assumed in this study that the purity of hydrogen will improve to be suitable for PEM-based FCVs as the EHS technology develops.

Although the exact hydrogen separation amount and performance are not known for commercial scale EHS modules, the present model conservatively estimates a 0.1 V overpotential to separate 85% of the hydrogen from the shifted anode effluent. This represents a slight increase in voltage (from 0.08 V) and a slight decrease in separation fraction (from 90%) as reported by Mitlitsky [60]. The 0.02 V estimated increase in overpotential is employed to account for the slightly lower hydrogen content in the feed gas in the present study than that from Mitlitsky [60] (22% versus 29%). A conversation with the manufacturer revealed that the performance estimation in this model is acceptable for a feed gas with a hydrogen composition as low as 20%.

4.3.2 Pressure Swing Adsorption (Concept 2)

Pressure swing adsorption (PSA) is used in industry, specifically in oil refineries, to separate hydrogen from steam methane reforming (SMR) reactor effluent streams. This process uses an adsorbent bed to capture non-hydrogen molecules in the inlet gas stream. The hydrogen is blown out of the first bed before the pressure is lowered to release the non-hydrogen molecules. This process is commercially proven, but the hydrogen content in the feed gas is typically higher than 75%. Figure 4.4 illustrates the PSA process which uses two separate beds to enable continuous operation.

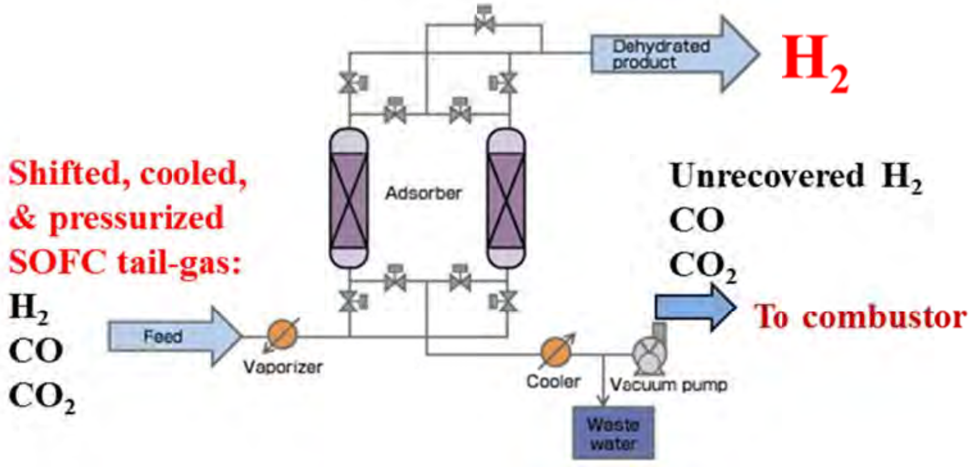

Figure 4.4 Pressure swing adsorption schematic

Product hydrogen purities high enough for PEM fuel cells can be achieved through this process, but the amount of hydrogen recovered decreases substantially with lower hydrogen content in the inlet gas (< 70%, molar basis) [73]. The effluent of SOFC generators with fuel utilizations of about 80% will have lower hydrogen content than SMR effluent (e.g., ~20% versus ~75%, molar basis). For an SOFC system operating at atmospheric pressure, there is no reduction in compression energy by using PSA for hydrogen separation. The composition of hydrogen at the inlet of the PSA unit must be 70% or higher for the process to be economical and achieve 85% separation [29].

In order to achieve the 70% hydrogen content in the feed gas, hydrogen recycle is employed, but this effectively lowers the overall hydrogen separation from 85% down. The optimum feed pressure to the PSA is 15-29 bar [74]; the inlet pressure for this model is chosen to be 22 bar.

4.4 Supporting Plant Processes

In addition to the technologies discussed in *Section 4.3*, various other supporting subsystems are now explained.

Figure 4.5 illustrates the plant's various subsystems, including the SOFC and the hydrogen recovery subsystems, which were explained earlier.

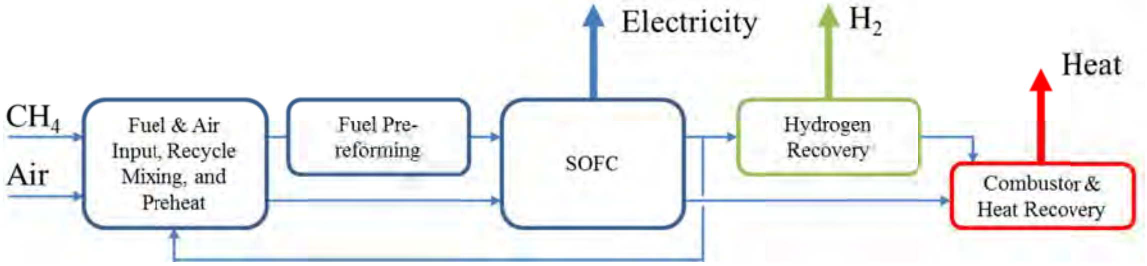

Figure 4.5 SOFC CHHP system process flow diagram

4.4.1 Fuel & Air Input, Recycle Mixing, and Preheat

Methane and air are fed into the system and compressed to 20 kPa above atmospheric pressure to account for pressure loss of the system. The fresh methane feed is mixed with recycled anode exhaust gas, which is used to ensure a steam-to-methane ratio of 2.5-3 at the pre-reformer inlet. Water production at the anode along with 65% anode recycle is sufficient to meet the steam-to-carbon ratio requirement. This extent of recycle brings the fuel utilization up from 62.5% per-pass to 82% overall. A ternary diagram analysis for hydrogen, carbon and oxygen atoms indicates that carbon deposition is not thermodynamically favorable for the pre-reformer and anode operating conditions, as shown by the operating condition mark indicated in Figure 4.6.

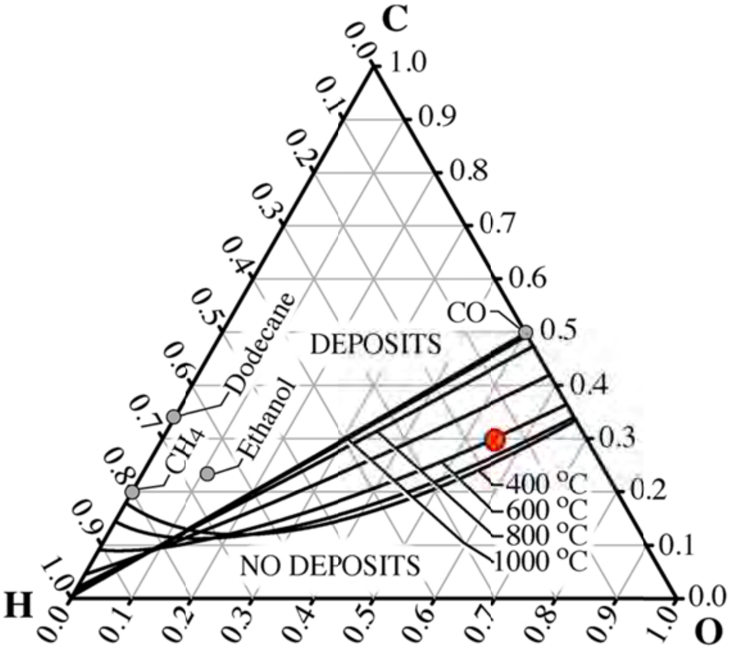

Figure 4.6 Ternary diagram analysis for carbon deposition at the SOFC anode inlet

Air supply is determined by the amount of cooling needed in the stack. An air stoichiometric factor for the system, defined as the ratio of oxygen fed into the cathode to the oxygen that is electrochemically reduced, is about 3.3 to limit the temperature rise of the stack to 150 °C.

The fuel mixture (fresh methane plus recycled gas) is heated to 700 °C by first exchanging heat with the anode effluent and then combustor effluent. The anode effluent is not hot enough after exchanging heat with the reformer effluent to accomplish adequate reformer preheat.

The air must also be heated to 650°C to avoid mechanical failure of the stack from a large temperature gradient. Air preheating also improves the kinetics of the oxygen reduction reaction. The air is partially heated (from 20 °C to about 80 °C) in a heat exchanger which is used to cool the non-recycled anode effluent to a temperature favorable for the water gas shift reaction. The bulk of the air heating (to 650 °C) occurs in a cathode feed-effluent recuperation heat exchanger.

All of the heat exchangers in the model are designed to have a 10 °C minimum temperature approach. The total heat loss for the plant is modeled to be 2.5% of the LHV of the methane feed. Table 4.2 summarizes the distribution of heat loss throughout the plant.

Table 4.2 Heat loss in %LHV of methane feed

	% of Methane Feedstock LHV
Pre-reformer	0.25%
SOFC	1.0%
WGS Reactor	0.25%
Combustor	0.5%
System Piping	0.5%

The heat loss allocation results in about 5 kW of heat loss for the pre-reformer and WGS reactor, 10 kW for the combustor and system piping, and 20 kW for the SOFC.

4.4.2 Fuel Pre-reforming

The fuel mixture is preheated to 700 °C for partial catalytic steam methane reforming (SMR). Pre-reforming of the methane is beneficial to limit the temperature gradients in the stack. The endothermic SMR reaction will occur near the inlet of the cell, and the coinciding exothermic electrochemical oxidation of hydrogen causes a steep temperature gradient down the length of the cell. By limiting the amount of direct internal reforming, the temperature gradient will be reduced. Pre-reforming is also necessary to reduce the higher hydrocarbons (e.g. C_2H_6) typically present in natural gas to CH_4 and H_2 molecules to minimize the risk of carbon deposition, although this aspect is not an issue in the present model. While partial external reforming is beneficial, the endothermic internal reforming also improves the performance of the stack by reducing the cathode air requirement to limit the stack temperature rise. Reforming of 20% of the CH_4 in the fuel mixture is used for the model. The endothermic reforming lowers the temperature of the fuel stream, so another heat exchanger is used to bring the anode inlet stream up to 650 °C using the anode effluent gas stream (exits at 800°C).

4.4.3 Hydrogen Recovery: Water-Gas Shift Reactor

The anode effluent which is not recycled is cooled down to around 300 °C which is favorable for the water gas shift (WGS) reaction. The WGS reactor is necessary to increase the hydrogen content of the gas entering the hydrogen separation unit. The performance of the EHS and PSA unit benefit from increased hydrogen concentrations. Although the EHS unit is modeled to separate 85% of the incoming hydrogen, independent of hydrogen concentration at the inlet, a WGS reactor is assumed beneficial for both separation methods. The anode effluent stream in the presence of a WGS catalyst is assumed to be in shift equilibrium in the model.

4.4.4 Heat Recovery

The hydrogen depleted tail-gas of the hydrogen separation unit is fed into a combustor for heat recovery. If the energy in the depleted gas is not sufficient to raise the combustor effluent to 750 °C, excess methane is fed into the combustor. This is necessary to maintain the minimum temperature difference for fuel reforming gas preheat. Because of the higher overall hydrogen separation amount for the EHS, excess methane is required for the combustor in Concept 1. The PSA Concept does not require excess methane because the heating value of the gas flowing into the combustor is high enough (lower hydrogen separation).

4.4.5 Blower & Compressor Performance

The chosen efficiencies of the blowers and compressors vary because of the different operating temperatures and compositions. Table 4.3 indicates the isentropic efficiency of the blowers and compressors which all have a mechanical efficiency of 95%.

Table 4.3 Isentropic Efficiencies of Compressors and Pump

	Isentropic Efficiency
CH_4 Blower	75%
Air Blower	65%
Recycle Blower	50%
PSA Recycle Compressor	82%
H_2 Compressor	82%
PSA Compressor	75%
Water Pump	85%

The anode recycle compressor operates at a low efficiency of 50% because of the high temperatures of the incoming gases (530 °C). Both the PSA compressor and the hydrogen product compressor require multiple stages because of an imposed pressure ratio limit of 2:1 with intercooling. The model assumes intercooling can be accomplished with negligible energy requirements (e.g. electric power for pumping cooling water to a heat exchanger). While this removes thermal energy from the gas streams, it makes the compression more efficient. By the same reasoning, the power required to cool and condense the gas stream for the PSA was also neglected, but this cooling results in a more significant heat recovery loss which lowers the plant performance.

4.5 System Design

Figure 4.7 illustrates the first design concept (Concept 1) of the CHHP system. Methane enters at state-point (1) and is compressed before mixing with the anode recycle gas. The fuel mixture is then heated in HX-01 before pre-reforming. The gas is heated a second time and enters the anode of the SOFC at state-point (6). The heat from the anode effluent is exchanged with both the anode and pre-reformer inlet gas streams. Part of the gas stream is then recycled, and the rest (10) gets cooled to a temperature (300°C) suitable for the water gas shift (WGS) reactor. The heat from the WGS reactor effluent is partially recovered in the hot water loop (32-33-34-35) before entering the EHS unit. The recovered hydrogen (30) is compressed to 30 bar. The EHS tail-gas (16) is combusted with part of the cathode effluent (air). The combustor effluent exchanges heat with the pre-reformer feed gas (heat exchanger not shown; red arrow indicates heat stream) and then with the water loop in HX-06 before being exhausted (29) at 92°C. The air for the cathode enters at (19) and undergoes the bulk of its preheating in HX-04 before entering the cathode (22) at about 650°C. The cathode effluent heat is recuperated in HX-04 and is then sent to the combustor. Part of the cathode effluent (25) is used for combustion, and the rest is bypassed before exchanging heat with the water loop in HX-06.

Figure 4.8 illustrates the second design concept (Concept 2). The differences between these concepts are evident in the hardware downstream of the water gas shift reactor (14). The shifted anode effluent heat is partially recovered to the water loop in HX-05, and a fraction of the water is condensed out. The remaining water is then drained in the condenser so that the PSA compressor inlet contains no water. The gas is compressed and sent to the inlet (20) of the PSA unit. Part of the hydrogen which is separated by the PSA unit is recycled back to the inlet to achieve the designated inlet composition, and the remaining hydrogen stream (26) is compressed to 30 bar. The PSA tail-gas is sent to the combustor, by which heat is recovered in HX-06 as described in Concept 1.

The design of the heat recovery subsystem is slightly different for the two separation methods. The water loop for Concept 1 flows through combustor effluent heat exchanger (HX-06) first, and then it recovers heat from the WGS effluent heat exchanger (HX-05) to cool the gas down to 190 °C for EHS operation. The water loop for Concept 2 flows through HX-05 first to maximize heat recovery, since the PSA feed gas has to be cooled down much further (to 40°C) than the EHS feed gas. A portion of the condensing can be accomplished in the HX-05 by this design. The remaining cooling for condensing the PSA inlet stream is assumed to be lost to the environment.

4.6 Model Results

The model was simulated in Aspen Plus™ for the generation of performance characteristics. Two baseline operation cases were simulated which differed mainly in the method for hydrogen separation. The plant was designed to output a net power of 1MWe AC, and the required methane fuel was calculated from the simulation.

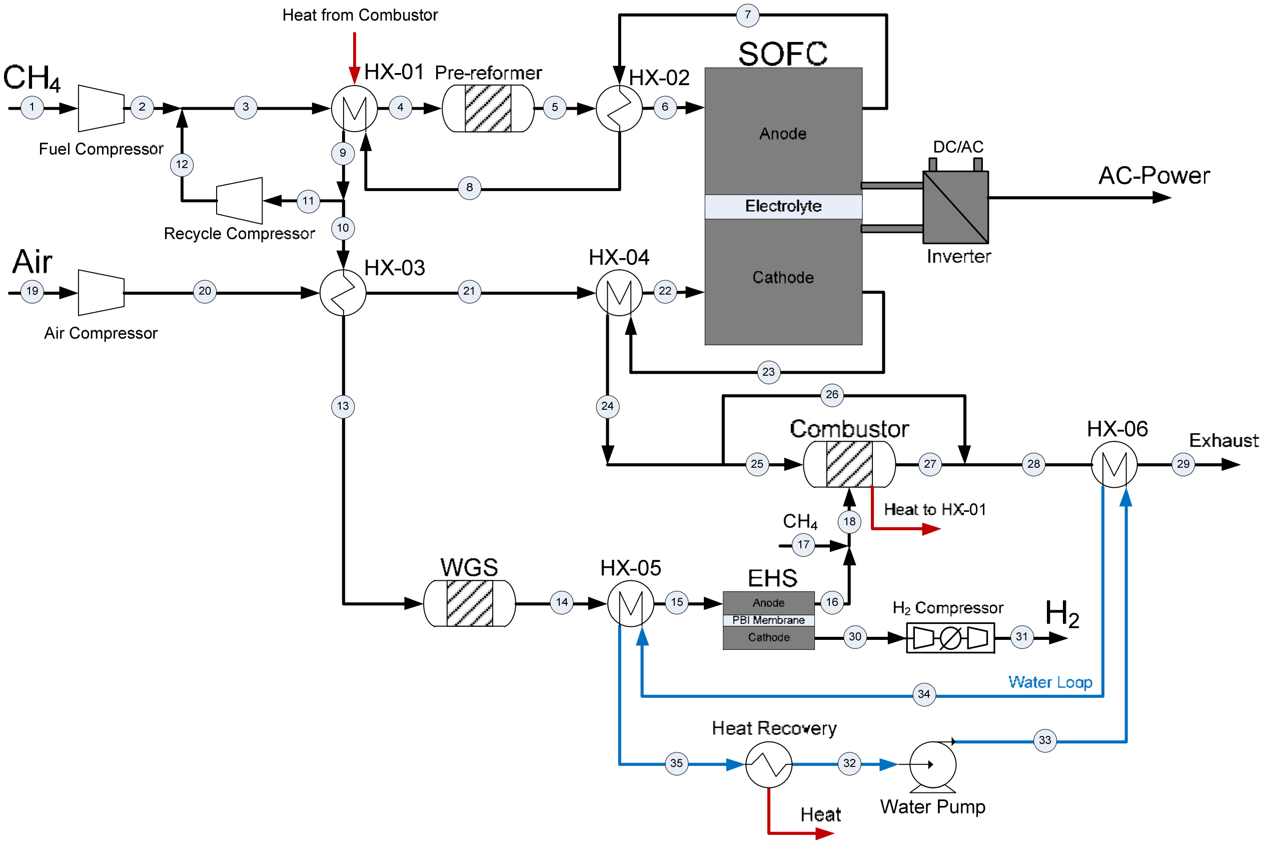

	T (°C)	P (kPa)	ṁ (kg/s)
1	20	101	0.039
2	37	122	0.039
3	484	115	0.349
4	700	112	0.349
5	568	109	0.349
6	658	108	0.349
7	750	103	0.477
8	676	101	0.477
9	533	100	0.477
10	533	100	0.167
11	533	100	0.310
12	581	115	0.310
13	300	98	0.167
14	343	95	0.167
15	190	94	0.167
16	190	94	0.164
17	30	101	0.003
18	184	94	0.167
19	20	101	1.849
20	45	122	1.849
21	80	121	1.849
22	654	119	1.849
23	800	114	1.721
24	201	113	1.721
25	201	113	1.592
26	201	113	0.129
27	676	90	0.296
28	294	90	1.888
29	92	89	1.888
30	70	136	0.003
31	70	3039	0.003
32	60	207	5.372
33	60	276	5.372
34	78	241	5.372
35	80	207	5.372

Figure 4.7 Concept 1: SOFC CHHP with EHS and table of state points

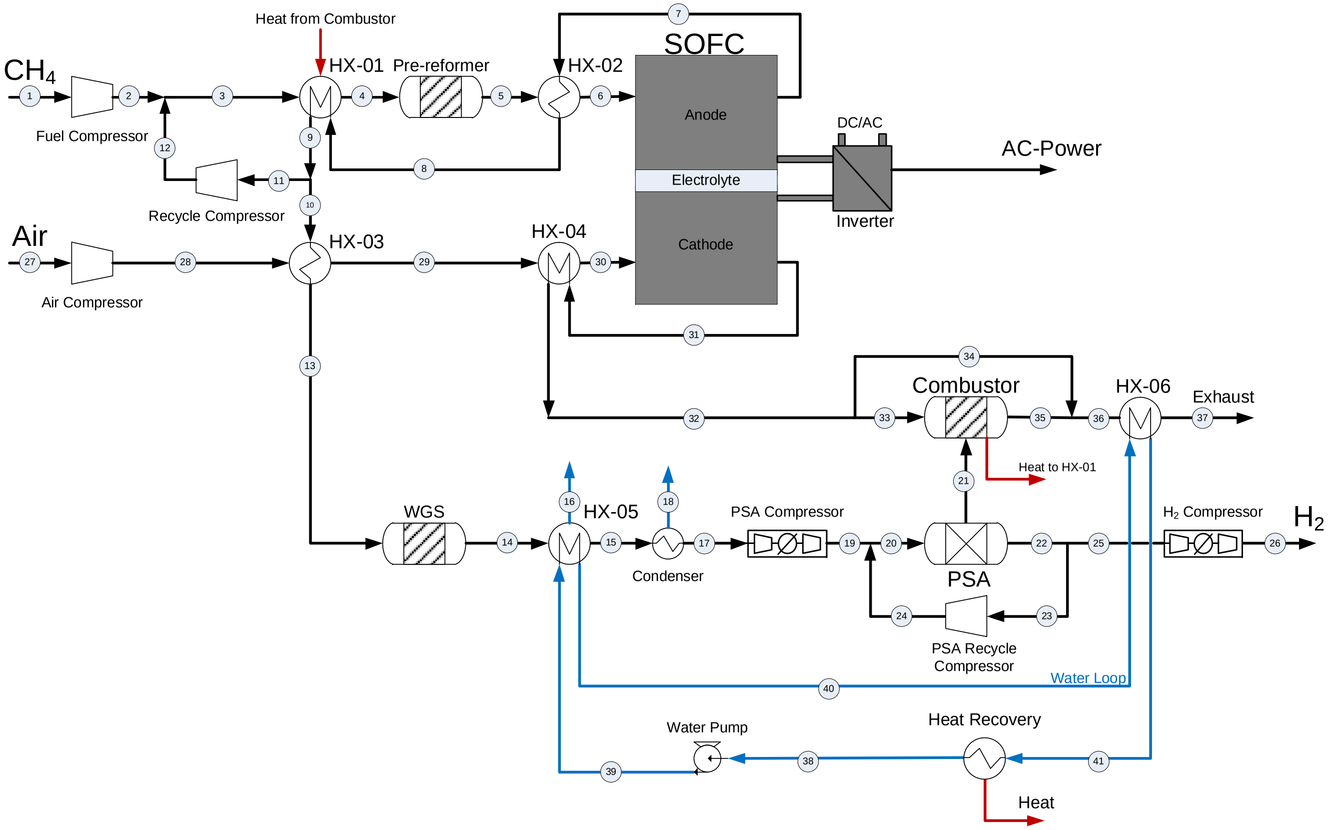

	T (°C)	P (kPa)	$\dot{m}$ (kg/s)
1	20	101	0.039
2	37	122	0.039
3	478	122	0.349
4	700	119	0.349
5	568	116	0.349
6	658	114	0.349
7	750	109	0.477
8	676	108	0.477
9	529	107	0.477
10	529	107	0.167
11	529	107	0.310
12	574	122	0.310
13	301	105	0.167
14	344	102	0.167
15	104	100	0.147
16	104	100	0.020
17	40	100	0.109
18	40	100	0.038
19	50	1772	0.109
20	53	1772	0.118
21	53	1772	0.108
22	53	1720	0.010
23	53	1720	0.008
24	56	1772	0.008
25	53	1720	0.002
26	70	3039	0.002
27	20	101	1.849
28	45	122	1.849
29	79	121	1.849
30	655	119	1.849
31	801	114	1.721
32	201	113	1.721
33	201	113	0.103
34	201	113	1.618
35	845	98	0.211
36	286	98	1.828
37	115	97	1.828
38	60	207	5.215
39	60	276	5.215
40	65	241	5.215
41	80	207	5.215

Figure 4.8 Concept 2: SOFC CHHP with PSA and table of state points

The hydrogen and heat generated downstream of the SOFC are byproducts, so the potential for recovery is dependent on the fuel utilization and efficiency of the SOFC. Figure 4.9 gives the overall plant feedstock consumption and commodity production.

Figure 4.9 SOFC CHHP plant material and energy inputs and outputs

The feed rate of methane is the only energy input into the system, since the SOFC supplies the electrical needs of compression and EHS power. Some excess methane is fed into the burner to supply proper fuel preheating which cannot be accomplished by anode effluent recuperation. The outputs of the system are the net 1 MWe AC power, compressed hydrogen to 30 bar, and heat in the form of a hot water (80 °C). Table 4.4 gives an overview of the net inputs and outputs of the plant.

For concept 1, the overall fuel efficiency is 79.3% based on the HHV of hydrogen and (85.2% on an LHV basis), as defined by Equation 4.14.

$$\eta_{CHHP} = \frac{P_{net} + Heat + HHV_{H_2}}{HHV_{CH_4}} \tag{4.14}$$

The electrical efficiency (HHV) is defined by Equation (4.15):

$$\eta_{elec} = \frac{P_{net}}{HHV_{CH_4}} \tag{4.15}$$

The heat production efficiency (HHV) is defined by Equation (4.16).

Table 4.4 Energy balance summary

	Concept 1: EHS	Concept 2: PSA
Energy Inputs		
Methane Feed (kg/s)	0.0420	0.0388
Methane LHV (MJ/kg)	50	50
Methane HHV (MJ/kg)	55.5	55.5
Power LHV (kW)	2102	1941
Power HHV (kW)	2333	2155
Internal Power Use (kW)		
CH_4 Compressor	1.6	1.6
Air Compressor	48.2	48.2
Recycle Compressor	25.8	25.8
Heating Water Pump	0.5	0.5
H_2 Compressor	16.6	1.6
EHS Unit	26.8	
PSA Compressor		47.5
PSA Recycle Compressor		0.4
Total Internal Power Use (kW)	119.4	125.6
Losses		
Heat Loss	61.9	58.3
DC/AC Inversion Loss	60.3	60.3
Energy Outputs (kW)		
SOFC Gross Power kWe AC	1144.9	1144.9
Heat kWt	427.3	417.2
Hydrogen (kg/day)	241.6	132.1
H_2 Power LHV	338.4	184.9
H_2 Power HHV	396.5	216.7
Gross Output (Power, Heat, H_2) LHV	1910.5	1747.0
Gross Output (Power, Heat, H_2) HHV	1968.6	1778.8
Net Electric Power Output	1025.5	1019.2
Net Energy Output LHV	1791.1	1621.3
Net Energy Output HHV	1849.3	1653.1
Efficiency		
Electrical Efficiency LHV	48.8%	52.5%
Electrical Efficiency HHV	44.0%	47.3%
Heat Production HHV	18.3%	19.4%
H_2 Production HHV	17.0%	10.1%
Fuel Efficiency LHV	85.2%	83.5%
Fuel Efficiency HHV	79.3%	76.7%

$$\eta_{heat} = \frac{Heat}{HHV_{CH_4}} \tag{4.16}$$

The hydrogen production efficiency (HHV) is defined by Equation (4.17).

$$\eta_{H_2} = \frac{HHV_{H_2}}{HHV_{CH_4}} \tag{4.17}$$

These efficiencies are given in Table 4.4. Two main differences between the two concepts are the hydrogen production and the electrical efficiency. The hydrogen production for Concept 1 is much higher due to the increased separation fraction of hydrogen for EHS compared to PSA; this is discussed in more detail below. The electrical efficiency for Concept 2 is higher than Concept 1 mainly because Concept 2 does not require the combustion of excess methane for preheating the SOFC fuel; while the PSA unit separates less hydrogen, the combustible tail-gas energy is sufficiently high to provide adequate fuel preheat. The gross AC power of 1145 kW is required to provide a net output of 1026 kW, while supplying the internal electricity of 119 kW (Concept 1).

In Concept 1, the EHS separates 85% of the hydrogen from its feed gas with the assumption of faradaic flows and an overpotential of 0.1V. The total power required for hydrogen separation is about 27 kW which includes a small amount of internal compression of the hydrogen gas up to 133 kPa as estimated by Thomassen et al. [70]; in essence this is a “free” compression because the voltage required for separation is also compressing the gas for no additional power input. The separated stream is assumed purified to 1 ppm of CO based on the cathode reduction of CO reported by Mitlitsky [60]: a high enough quality for PEM transportation fuel cells which are the likely recipient of the product hydrogen.

Concept 2 exhibits an 76.7% overall efficiency (HHV). To reiterate, the PSA can only economically separate hydrogen if three criteria are met: the gas is at low temperatures (40-50 °C), the gas is dry, and the hydrogen composition is above 70% [29]. The anode effluent must be cooled and drained of water before entering the PSA subsystem. About half of the heat loss due to PSA inlet gas cooling is recovered in the heating water loop, but the other half is lost to the environment; this loss partially offsets the additional heat from the excess hydrogen going into the combustor. For the composition requirement, a hydrogen recycle of the separated hydrogen coming out of the PSA is needed to bring the 40% H_2 anode effluent content by volume up to 70%. While each pass of the PSA separates 85% of the hydrogen, the required recycle of 84% brings the net hydrogen recovery down to about 47%.

The electric power required for hydrogen separation and compression are nearly equal for both Concepts (~5 kW difference), but that is mainly because the PSA requires less power to compress less hydrogen. In terms of energy-per-kg of hydrogen separated (compression energy not included), the EHS unit requires 2.7 kWh/kg-H_2 while the PSA unit requires about three times more energy (8.2 kWh/kg-H_2) to separate hydrogen from the shifted SOFC tail-gas. It should be noted that the compression power is significantly less for Concept 2 because the PSA-separated hydrogen is already compressed to 22 bar.

Concept 1 requires an additional 160 kW of fuel to the combustor for SMR preheat which also increases the heat recovery. Both concepts generate about 400 kW of thermal energy in the form of hot water which translates into a plant thermal-to-electric ratio of about 0.4. The chemical (hydrogen fuel)-to-electric ratio differs more substantially between concepts, with Concept 1 at 0.33 and Concept 2 at 0.18 on an LHV basis. As will be discussed, the amount of hydrogen production can be increased by increasing the fuel input to the plant without substantially increasing the electric power production via electrochemical fuel conversion.

4.6.1 Hydrogen Over-production Case Study

An operational case study for this system is carried out to explore the effect of producing excess hydrogen. The requirement for each concept is to produce an extra 100 kg-H_2/day from the baseline case (Table 4.4). This requirement is met by feeding excess methane into the system, while the electric power requirement is still 1 MWe AC. The excess methane fed into the system gets reformed in the SOFC subsystem, and there is a

Table 4.5 Hydrogen over-production case study model results

	Concept 1: EHS	Concept 2: PSA
Energy Inputs		
Feed rate (kg/s)	0.0441	0.0417
Meth LHV (MJ/kg)	50	50
Meth HHV (MJ/kg)	55.5	55.5
Power LHV (kW)	2206	2084
Power HHV (kW)	2449	2313
Internal Power Use (kW)		
CH_4 Compressor	1.7	1.7
Air Compressor	41.8	42.5
Recycle Compressor	27.9	27.7
Heating Water Pump	0.4	0.4
H_2 Compressor	24.4	3.0
EHS Unit	38.5	
PSA Compressor		57.3
PSA Recycle Compressor		0.4
Total Internal Power Use (kW)	134.7	133.0
Losses		
Heat Loss	61.5	59.7
DC/AC Inversion Loss	61.0	61.0
Energy Outputs (kW)		
SOFC Gross Power (kWe AC)	1160	1159
Heat (kWt)	391.5	416.6
Hydrogen (kg/day)	344.9	237.7
H_2 Power LHV	482.9	332.9
H_2 Power HHV	566.0	390.1
Gross Output (Power, Heat, H_2) LHV	2034	1908
Gross Output (Power, Heat, H_2) HHV	2117	1965
Net Electric Power Output	1025	1026
Net Energy Output LHV	1900	1775
Net Energy Output HHV	1983	1832
Efficiency		
Electrical Efficiency LHV	46.5%	49.2%
Electrical Efficiency HHV	41.9%	44.3%
Heat Production HHV	16.0%	18.0%
H_2 Production HHV	23.1%	16.9%
Fuel Efficiency LHV	86.1%	85.2%
Fuel Efficiency HHV	81.0%	79.2%

reduction in fuel utilization (from 63% to 54% per pass). Results from this scenario are given in Table 4.5.

The increase in hydrogen production for this operation mode is about 100 kg/day, as specified. The total hydrogen production amounts to 345 kg/day for the Concept 1, and 238 kg/day for Concept 2. For perspective on the amount of fuel cell vehicles that this level of production can sustain, a couple of assumptions must be made: the vehicle owner drives 12,000 miles per year (33 miles per day) and the fuel cell vehicle achieves 55 miles per kilogram of hydrogen. These assumptions lead to a hydrogen supply for 577 vehicles for Concept 1 and 398 vehicles for Concept 2. These are approximations of the usage and performance of fuel cell vehicles, but they give a ballpark estimate as to the scale of fuel cell vehicles this production plant could supply.

The results from this case study show an increase in overall system efficiency for several reasons. Both scenarios resulted in an increase in operating voltage by about 10 mV due to a higher content of reactant hydrogen (increases the Nernst potential), which slightly increased the SOFC efficiency. Despite this increase in operating voltage, both electrical efficiencies went down because of decreases in fuel utilization and increases in compression work for the recovered hydrogen. Slightly less compression power is required for the air blower (excess air is used for cooling the SOFC stack) in both concepts because the heat capacity of the anode gas increased. Concept 1 (ESA) required less additional methane for fuel preheat than the baseline case, even with the high amount of hydrogen recovery. Overall efficiency for Concept 2 (PSA) shows a greater increase than Concept 1 due to an increase in hydrogen separation efficiency; hydrogen recovery from the PSA increased from 47% to 60% because of a higher hydrogen content in the feed gas of the PSA. The energy required for PSA hydrogen separation in Concept 2 was lowered to 5.8 kWh/kg-H_2 (from 8.7), while the EHS unit in Concept 1 remained the same at 2.7 kWh/kg-H_2.

While the operation for producing excess hydrogen results in a higher overall efficiency, the value of hydrogen versus electricity is uncertain. If there is no demand for the excess hydrogen, it is not recommended to operate in this mode. This study is only analyzing the *production* of hydrogen, and additional compression is necessary if hydrogen *storage* is used. The hydrogen must be highly compressed (up to 450 bar) for adequate volumetric energy density in storage tanks. This excess energy requirement for storing hydrogen emphasizes the value of producing hydrogen on demand. This system could divert the anode effluent to the combustor if the demand for hydrogen is low to mitigate the need for storage.

4.7 Economics

The economics of this process are evaluated to determine the value of the hydrogen produced in a polygeneration SOFC system. The economics are evaluated on the baseline EHS Concept system.

4.7.1 Capital Investment

The capital investment of the plant must first be determined. The subsystems of the plant include methane fuel and air preheat, SOFC electricity generation, hydrogen production, and heat recovery.

Multiple sources are used to determine the capital cost of the plant. The cost scaling methodology explained in Chapter 2 is used for some of the plant components, but several of the component costs are determined on a “per-unit” basis (e.g. \$/kW). Table 4.6 gives the component cost breakdown of the plant, and the details of the cost references are given as footnotes of Table 4.6. It should be noted that this costing methodology results in an accuracy of ±30%.

In addition to direct costs, the indirect costs shown in Table 4.7 include engineering and design, plant construction, legal and contractors fees, and project contingencies; these costs were allocated based on Spath et al. [29]. The total capital investment (direct plus indirect costs) amounts to 4,042 k$\$_{2009}$

Table 4.6 Cost of system components in k$\$_{2009}$

	C_o[a]	S_o	S	units	n	IF[b]	IC
SOFC & Inverter[c]	0.53	1	1145	k$/kW	-	1.42	858
Reformer[d]	204	1125	334	kgH_2/day	0.7	1.1	96
WGS Reactor[d]	169	1500	282	kgH_2/day	0.7	1.1	58
EHS Unit[e]	2.23	1	27	k$/kW	-	1.42	85
Heat Exchangers[f]	-	-	-	-	-	-	675
Blowers & Pumps[f]	-	-	-	-	-	-	215
Burner[f]	-	-	-	-	-	-	248
H_2 Compressor[g]	23	1	10	kgH_2/hr	-	2.47	155
Total Installed Costs[h]							2,390
Total Direct Costs[i]							2,677

[a] These base costs have been scaled from the original cost index (CEPCI$_o$) to the 2009 CEPCI (521.9)

[b] The installed factor is only used if the base cost does not include installation (otherwise its value is 1).

[c] Gerdes et al. [58]: cost of SOEC module of 400 $\$_{2002}$/kW uninstalled based on DOE cost target for SOFC systems including rectifier and controls. An installation factor of 1.42 is also referenced.

[d] James [75]: H2A forecourt SMR derived H_2 case study; scaled based on kg H_2/day produced.

[e] Saur [76]: based on a PEM electrolyzer cost of 2000 $\$_{2005}$/kW.

[f] AspenTech Economic Analyzer™ software is used to calculate the installed cost of floating head shell and tube heat exchangers based on heat transfer area (heat transfer coefficients calculated from P&T and materials suitable for the operating temperature (inconel was used for high temperature (>700 °C) operation), blowers and pumps based on flow rates and design pressure, and a high temperature burner based on heating duty and flow rate.

[g] James [75]: H2A forecourt SMR derived H_2 case study

[h] The TIC of the plant components is not inclusive of buildings and service facilities for the plant.

[i] The buildings and services facilities are estimated to be 12% of the total installed cost, adding 287 k$ to the installed component costs for the total direct costs.

Table 4.7 Indirect costs allocated as a percentage of TDC from Spath et al. [29] and actual costs for this plant

	% of TDC	k$
Engineering & design	13	348
Site prep & construction	14	375
Legal and contractors fees	9	241
Project contingency	15	402
Total Indirect Costs	51	1,365

4.7.2 Operating & Maintenance Costs

The operating costs for the plant were estimated using multiple sources and assumptions. The SOEC operating, maintenance, and replacement costs were estimated based on Gerdes et al. [58] to be 0.22 ¢/kWh; the same assumption for operating the EHS unit is made. Table 4.8 gives the annual O&M costs for the major components of the plant.

Table 4.8. Operating costs for various components

	Annual k$
SOFC[a]	20.9
Reformer catalyst[b]	13.3
WGS Reactor catlayst[c]	4.7
EHS unit[d]	0.5
Unplanned[e]	40.4
Total[f]	79.9

[a] Gerdes et al. [58]: 0.22 ¢/kWh of SOFC AC_e production
[b] James [75]: reactor sizing from 20,000 GHSV with 7 $\$_{2005}$/lb-cat. Assumed catalyst density of 1200 kg/m^3. Catalyst replaced every year.
[c] James [75]: reactor sizing from 10,000 GHSV with 7 $\$_{2005}$/lb-cat. Assumed catalyst density of 1200 kg/m^3. Catalyst replaced every year.
[d] Assumed same operating costs as SOFC (0.22 ¢/kWh for DC power input to EHS)
[e] Unplanned O&M assumed to be 1% of the production TDC based on Steward et al. [77].
[f] This total is not inclusive of labor and overhead, insurance and taxes, licensing and permitting, and property rental.

In addition to the total O&M in Table 4.8, the annual labor and overhead, licensing and permitting, insurance and taxes, and rent payments amount to 89.1 k$. The total annual O&M amounts to 168.9 k$.

4.7.3 Methane Feedstock & Electricity Credit Rates

2010 data from the Energy Information Agency data gives insight into the range for both methane feedstock and electricity credit rates. The range of natural gas rates for commercial consumers is roughly 7-15 $/MMBTU (HHV basis) for the continental United States (30 $/MMBTU for Hawaii), with the average at 10 $/MMBTU. Electricity rates range from 0.07 $/kWh to 0.16 $/kWh for the continental United States (0.29 $/kWh for Hawaii), with the average at 0.10 $/kWh. The heat production is accounted for by assuming it is displacing hot water produced from a natural gas fired boiler which operates with 80% efficiency; this reduces the net cost of natural gas feedstock proportional to the heat production.

4.7.4 H2A Life Cycle Analysis

The total capital investment (direct and indirect) for the plant is an input for the H2A life cycle analysis tool [42], which is used to generate a levelized cost for hydrogen production. The various economic parameters specified for the H2A program are given in Table 4.9.

Table 4.9. Economic inputs to the H2A tool

	Value
Constant dollar value	2005
Internal rate of return (after-tax)	10%
Debt/Equity	0%/100%
Plant life	20 years
Depreciation	MACRS
Depreciation recovery period	7 years
Construction period	1 year
1st year	100%
2nd year	0%
Start-up time	6 months
Revenues	50%
Variable costs	75%
Fixed costs	100%
Working capital	15% of total capital investment
Inflation rate	1.90%
Total taxes	38.90%
Decommissioning costs	10% of depreciable capital
Salvage value	10% of total capital investment
Operating capacity	90%
CH_4 feedstock cost	Varied
Electricity product price	Varied
Heat product cost	Equivalent to CH_4 feedstock
Hydrogen product cost	Output

The operating capacity is assumed to be 90%; this is relatively high compared to the previous two fuels production plants for two reasons: i) the methane feedstock (natural gas) is available on-demand and ii) the SOFC system is assumed to be operating continuously (to baseload a building cluster), so downtime is only caused by routine maintenance and replacements. A range of methane feedstock cost is explored to account for the dynamic nature of natural gas pricing and the variation of prices throughout the United States. The electricity product value is also varied for the same reason.

4.7.5 Hydrogen Production Cost Sensitivity Analysis

A breakdown of cost contributions to the total cost of hydrogen produced from this system in $/kg is shown in Figure 4.10.

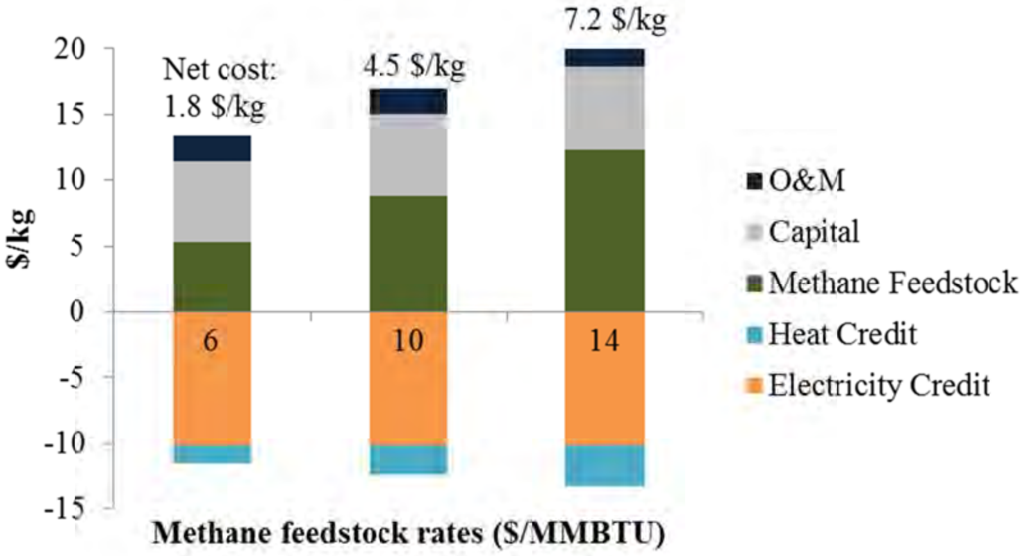

Figure 4.10. Cost contribution to hydrogen production for an electricity credit price of 0.10 $/kWh at various methane feedstock costs

The capital costs are the most significant contributor when the methane feedstock costs are low (below 8 $/MMBTU). The methane feedstock cost contribution dominates when the costs are high, and the hydrogen production cost rises quickly for a constant electricity credit price of 0.10 $/kWh. As the methane feedstock costs increases, the heat production credit also increases which decreases the rate at which hydrogen production cost goes up. The O&M cost adds about 2 $/kg to the hydrogen production cost.

Figure 4.11 illustrates the dependence of hydrogen production cost on the methane feedstock cost at various electricity credit prices. The cost of hydrogen has an increasing linear dependence on the methane feedstock cost, as shown in Figure 4.11. For the electricity credit of 0.12 $/kWh, the hydrogen production cost ranges from 0-6.5 $/kg for the methane feedstock cost of 6-16 $/MMBTU. For each 1 $/MMBTU of methane feedstock cost, the hydrogen production cost increases by about 0.67 $/kg. For the electricity credit of 0.08 $/kWh and a methane feedstock cost of 6 $/MMBTU, the cost of hydrogen production is about 4 $/kg, and it rises to about 11 $/kg for a high methane feedstock cost of 16 $/MMBTU.

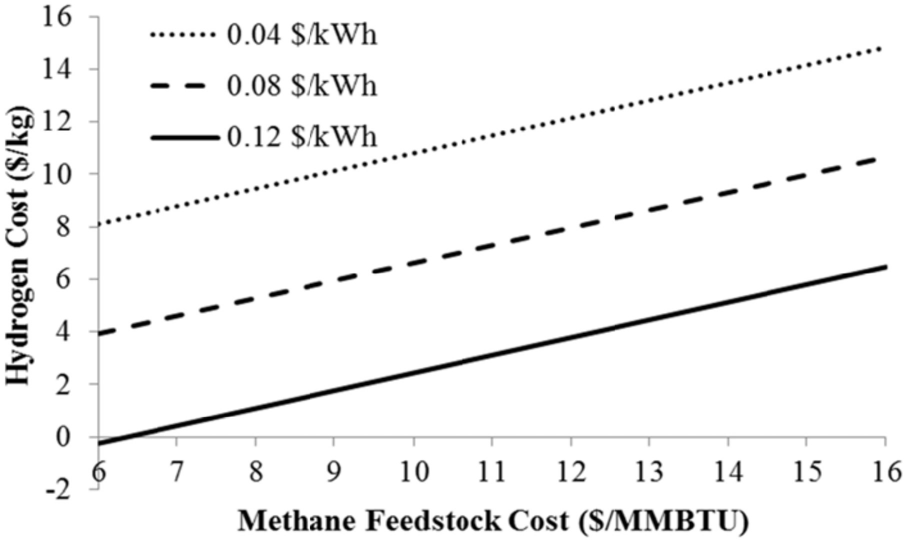

Figure 4.11. Cost of hydrogen production dependency on methane feedstock costs for various electricity credit prices

Figure 4.12 illustrates the dependence of hydrogen production cost on the electricity credit prices at various methane feedstock costs.

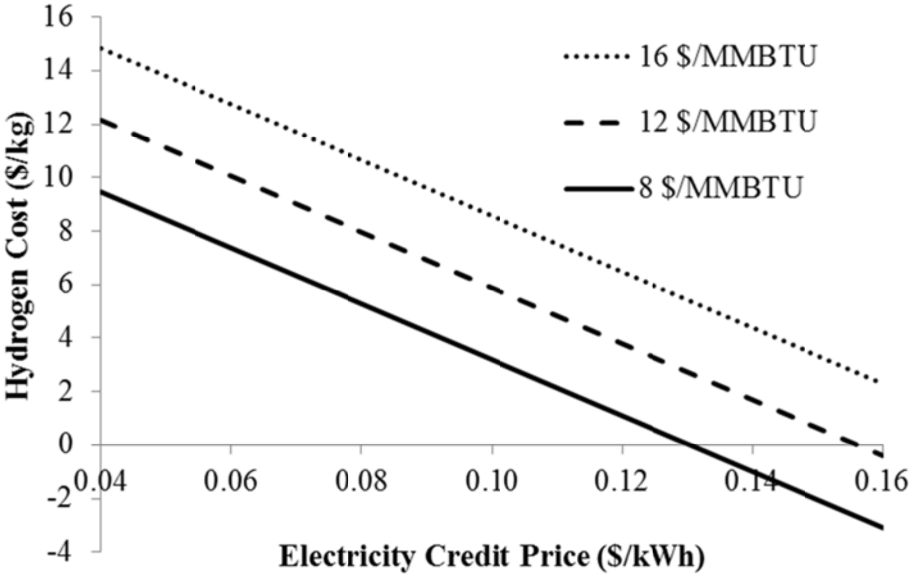

Figure 4.12. Cost of hydrogen production dependency on electricity credit prices for various methane feedstock costs

The cost of hydrogen production has a decreasing linear dependence on the electricity rate. The hydrogen production cost ranges from 12 $/kg to essentially free for an electricity credit price range of 0.04 $/kWh to 0.16 $/kWh. For each 0.01 $/kWh of electricity credit, the hydrogen production cost increases by about 1 $/kg. For a methane feedstock cost of 12 $/MMBTU and an electricity credit price of 0.10 $/kWh, the cost hydrogen is 5.9 $/kg. For a methane feedstock cost of 16 $/MMBTU, the hydrogen cost ranges from 14.7 $/kg to 2.3 $/kg for the range of electricity credit prices shown.

The cost of producing hydrogen from the SOFC CHHP system is highly dependent on both the methane feedstock cost rate and the electricity product value. This is consistent with the economic trade-offs of fuel and power producing systems: higher value products and lower value feedstock will result in favorable economics. The Spark Spread can be approximated as the difference between the cost of natural gas (in $/MMBTU) and electricity (in ¢/kWh), and it determines the economic viability of using fuel cell systems. As a rule of thumb, the Spark spread should be greater than two for fuel cell systems to be cost effective; this is also necessary for the hydrogen production cost to be low. The cost of hydrogen is 2.4 $/kg when the electricity price is 12 ¢/kWh and the methane feedstock cost is 10 $/MMBTU; lowering the cost of the methane feedstock down to 9 $/MMBTU (Spark spread of three) brings the hydrogen production cost down to 1.77 $/kg.

In relation to gasoline prices for which the hydrogen would replace, hydrogen fuel cell vehicles can achieve between 50-70 miles per kg of hydrogen; this is almost double the fuel economy, in miles per gallon of gasoline, compared a gasoline powered car. The value of hydrogen in $/kg can be competitive with gasoline at prices above the selling price of gasoline (3-4 $/gal) for this reason.

4.8 Summary & Conclusions

This study aimed to demonstrate the potential benefits of hydrogen co-production from an SOFC system. The unique aspect of this plant, compared to other co-generating fuel cell systems, is the separation of hydrogen which could be used for end uses such as PEM fuel cell vehicles. SOFC systems with co-generation are known to exhibit high overall efficiency, and this study characterized the potential for a relatively new technology (EHS) to separate hydrogen from SOFC effluent gas streams. The overall fuel efficiency of 79.3% HHV (85.2 LHV) is relatively high, and the value of PEM fuel cell grade hydrogen could make this type of a system even more desirable.

There are several trade-offs between the two methods for hydrogen separation. The PSA system is a commercially developed separation method, but the performance suffers from a low concentration of hydrogen in the anode effluent stream. This results in a low overall hydrogen separation rate of less than 50% for the PSA method. While ESA units are less commercially available, they use less electricity based on the assumed overpotential of 0.1V, and the separation rate of 85% is much higher.

The case study for hydrogen overproduction results in increased overall efficiency for both concepts: an increase of 1.7 efficiency points for Concept 1 and 2.5 points for Concept 2 (HHV basis). The PSA efficiency shows a greater increase due to the increase in hydrogen content for the PSA, but the EHS concept still has higher efficiency (both hydrogen and overall). The increase in hydrogen recovery and a higher overall efficiency makes the EHS unit a better option than PSA for SOFC effluent hydrogen separation.

The economics of this process were evaluated to determine the value of the hydrogen produced in a co-generation plant. For the electricity credit of 0.08 \$/kWh and a methane feedstock cost of 6 \$/MMBTU, the cost of hydrogen production is about 4 \$/kg, and it rises to about 11 \$/kg for a high methane feedstock cost of 16 \$/MMBTU. For each 1 \$/MMBTU of methane feedstock cost, the hydrogen production cost increases by about 0.67 \$/kg. For a methane feedstock cost of 12 \$/MMBTU and an electricity credit price of 0.10 \$/kWh (spark spread of 2), the cost hydrogen is 5.9 \$/kg. For each 0.01 \$/kWh of electricity credit, the hydrogen production cost increases by about 1 \$/kg. The economic findings in this study show that hydrogen production costs are highly dependent on the spark spread of methane and electricity.

CHAPTER 5

FUEL PRODUCTION AND DELIVERY COST COMPARISON

A discussion of the relative advantages and disadvantages of the analyzed pathways to fuel production is presented in this chapter. The cost of fuel production for the three pathways presented in Chapters 2, 3, and 4 are compared using a range of primary feedstock costs. A case study is analyzed for the delivery costs to fueling stations based on a common set of assumptions for all fuels. The fuel delivery cost is determined to compare the total consumer cost of hydrocarbon fuels to a hydrogen production pathway at the same scale. This analysis is made to determine the relative benefits of producing fuels which can be used the existing infrastructure. A discussion on the advantages of producing hydrogen from the small-scale SOFC CHHP plant is given in comparison to large-scale renewable production and distributed production.

5.1 Fuels Production Cost Comparison

To compare fuel production cost from the plants presented in this thesis, it is necessary to use a consistent cost of energy for both the plant inputs and outputs. Figure 5.1 illustrates the production cost of SNG from Chapter 2, gasoline and diesel from Chapter 3, and hydrogen from Chapter 4 in units of \$/GJ; the primary feedstock costs for these plants represent hydrogen, electricity, and methane (equivalent to natural gas), respectively. The range which corresponds to the feedstock cost for each plant is 0-7 \$/kg-H_2, 0-0.14 \$/kWh, and 3-20 \$/MMBTU for the hydrogen, electricity, and methane, respectively. The upper end of the hydrogen feedstock cost range is representative of renewable hydrogen production from electrolysis [41]. The electricity cost range is assumed to capture the costs of electricity generated from renewable sources, such as wind. The methane feedstock cost range is inclusive of the range of fossil-based natural gas costs for the continental U.S; the upper end of this range captures a scenario of purchasing a renewable energy credit (REC) for the methane feedstock. A REC for the methane feedstock represents the production of a renewable energy source such as biogas or landfill gas. A premium (estimated to be 4-10 $/MMBTU) is added on to the cost of the fossil-based natural gas, and the feedstock is then considered renewable. The plant capacity factor was shown to have a significant impact on production cost in the F-T liquid fuels plant, and the relatively high capacity factor of 90% is chosen to compare the best case scenarios of fuel production cost. The electricity credit price for the SOFC CHHP hydrogen production plant is chosen to be 0.10 $/kWh based on the 2011 average price for consumers in the U.S.

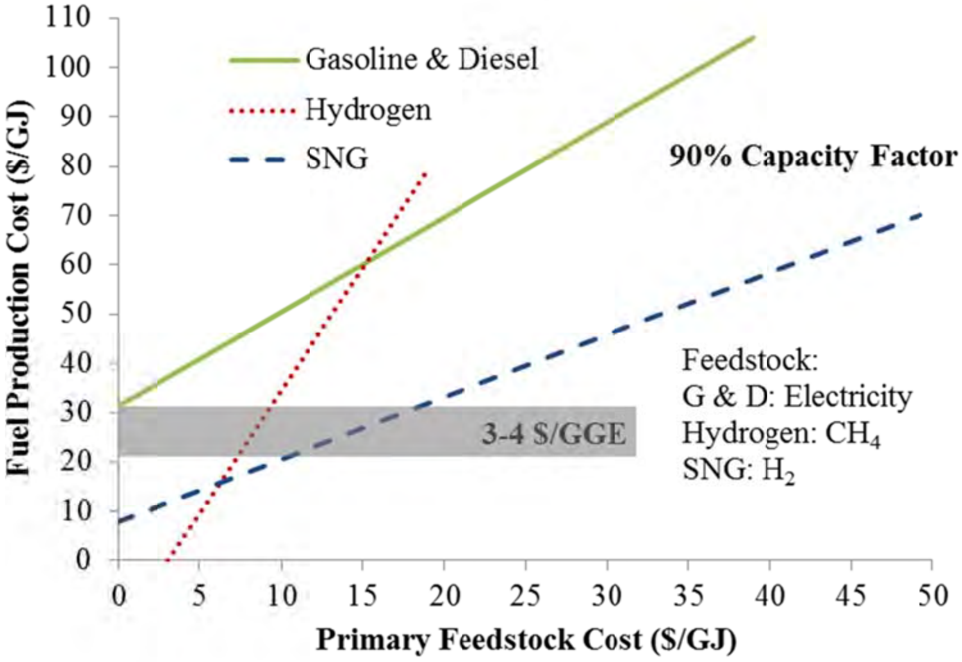

Figure 5.1 Fuel production cost dependence on primary feedstock cost. A 90% capacity factor is used for each production scenario.

From Figure 5.1, the range primary feedstock costs are different based on the criteria given above. A range of fuel cost corresponding to 3-4 $/GGE is shown for reference to the current price of gasoline and diesel fuels derived from crude oil. The rate of change of fuel production cost is indicative of the efficiency for the SNG and F-T liquid fuels production plants. The overall plant efficiencies for the SNG and F-T liquid fuels plant are 78.0% and 50.1% (HHV), respectively; the ratio of efficiencies for the two plants is approximately equal to the ratio of the slope of the respective lines in Figure 5.1 (less than a 3% difference). It should be noted that the likelihood of having no cost for the feedstock (y-intercept) is not high in the future, but it is less likely to obtain free hydrogen piped to the SNG plant than it is to obtain free electricity at the wind farm site. If there is no immediate demand for electricity at the time of production (e.g. if the wind farm in a remote location has no demand for the wind production at certain times), the electricity cost could be very low. Therefore, the lower end of the feedstock cost range is more relevant to the F-T liquid fuels plant than the SNG plant.

The steep slope of the hydrogen production cost line in Figure 5.1 is not explained by the overall SOFC CHHP plant efficiency (the plant efficiency is 79.3% HHV). The high rate dependence of hydrogen production cost on methane feedstock cost is because hydrogen is not the main co-product for the SOFC plant, and the hydrogen production efficiency (Equation (4.17)) for the plant is only 16.1%. The electricity is the largest co-product for the SOFC plant, and the economics of the process are highly dependent on the difference between methane feedstock cost and the electricity credit price (this difference is termed the Spark Spread). The electricity credit price used for the hydrogen production cost line in Figure 5.1 is 0.10 $/kWh, and the upper end of the methane feedstock cost range is 20 $/MMBTU, which corresponds to a Spark Spread of negative 10. SOFC systems are typically only cost effective if the Spark Spread is around 2 or greater, which would produce hydrogen at 3.2 $/kg.

To illustrate the increase in production cost with an operating capacity factor similar to that of a wind farm (35%), Figure 5.2 shows the resulting fuel costs. The SOFC CHHP plant still has a 90% capacity factor because the natural gas feedstock is assumed to be readily available on demand.

It is indicated from Figure 5.2 that the production cost for gasoline and diesel increases the most by lowering the capacity factor, and this is due to the large capital investment which is underutilized with low operation time. Although the SNG production cost is substantially lower than the synthetic gasoline and diesel cost on an energy basis, the current (2011) value of the gasoline and diesel is about 3 times greater than SNG (natural gas market) because of its widespread use in the transportation market.

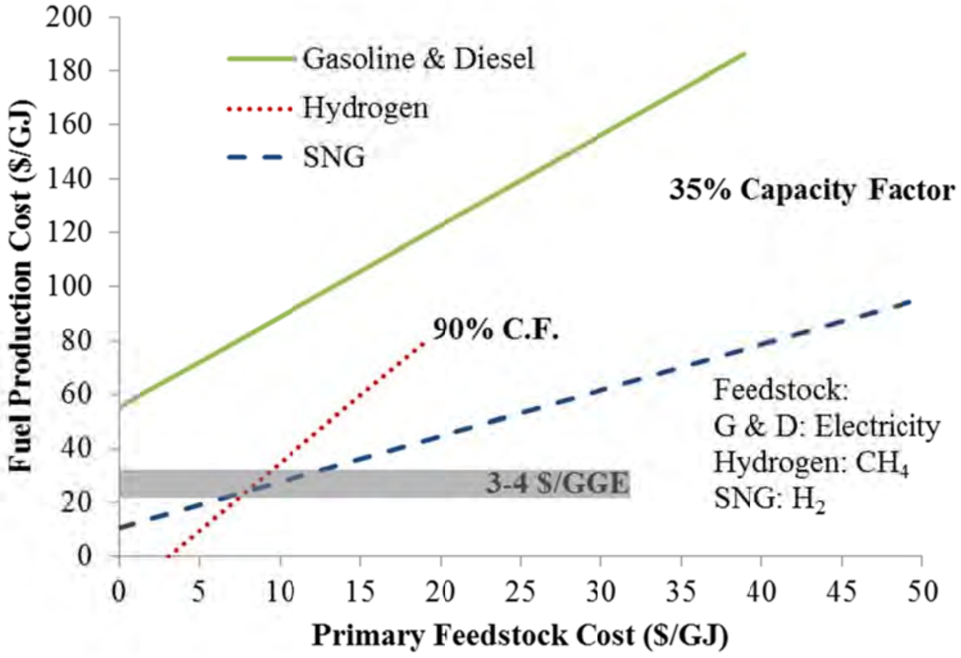

Figure 5.2 Fuel production cost dependence on primary feedstock cost. A 35% capacity factor is used for the SNG and G &D production scenario.

5.2 Important Factors for Production Economics

There are common factors of the fuel production pathways that require attention for cost effectiveness and deployment viability:

- Plant efficiency
    - Efficient conversion of renewable energy to fuels
- Feedstock cost
    - Cheap, renewable hydrogen and electricity
- Capital cost
    - Improve technological and manufacturing maturity
- Operating capacity factor

    - High resource availability (e.g. wind, solar, multiple sources)
- Infrastructure and market value of fuels
    - End-use infrastructure
    - Cheaply deliver to consumers

It is crucial for fuel production plants to utilize the renewable energy, which is expensive at present (e.g. wind-generated electricity), in the most efficient process possible. This will allow for the preservation of the source energy in the product fuels, which is the purpose of the conversion process. The feedstock cost must be as low as possible to compete with fossil fuels in the near-term, and this variable is dependent on the technological and manufacturing maturity of the source energy converter (e.g. wind turbines and electrolysis units). The capital costs for this study assumed a high degree of technological and manufacturing maturity (e.g. SOEC cost of 750 $/kW installed), and this is imperative for the co-electrolysis plant in particular. The SOEC capital investment accounts for about 50% of the total capital cost, and the capital cost contribution to the fuel production cost is much more significant than the SNG plant, for which the capital cost represents a much lower percentage of the production cost (20-25%). A high operating capacity of the plant is crucial to keep the capital investment low with respect to the lifetime of the plant. The operating capacity depends on the resource availability, so it is important to construct these plants in a region with continuous, strong winds or use multiple sources of electricity generation (wind, solar, geothermal, hydro), for example. Typical wind farm capacity factors range from 30-40%; a slightly higher capacity factor (40-50%) for the *plant* can be achieved by under sizing it compared to the capacity of the *wind farm*, but using only one intermittent resource for electricity generation as a feedstock to the plant still represents a major barrier to the economics of the pathway.

The last *factor* from the above list has not been discussed in detail, and a high-level analysis is presented in the following section for the comparison of the value of the fuels with respect to the existing and future infrastructure and the costs associated with delivery to the consumer.

5.3 Case Study for SNG, Gasoline, and Diesel Versus Hydrogen Fuel: Production and Delivered Cost Comparison

The transport (e.g. pipelines) and end-use (e.g. fuel cell vehicles) infrastructure for hydrogen is in its infancy. A comparison is made here as to the relative costs of producing and distributing hydrogen from electrolysis with the costs of producing and distributing SNG and liquid fuels (gasoline and diesel) from the production plants presented in Chapters 2 and 3. The SNG plant converts hydrogen, which is piped to the plant from a wind farm powered electrolysis plant, to SNG, and it is distributed from the city-gate to the city for end-use. The gasoline and diesel liquid fuels are produced at the wind farm site, where the co-electrolysis and F-T plant is located. In this case study, the analysis for hydrogen production is wind-powered electrolysis, which is located at the wind farm site. The delivery costs for the respective fuels are added to the production costs for comparison of total consumer cost (excludes taxation of fuels for simplicity).

It is assumed in the fuel production plants from Chapters 2 and 3 that technological maturity for all components (e.g. SOEC production costs of 750 \$/kW) and resource availability (abundant sources for wind power and carbon dioxide) is attained at the time of production; these assumptions are reasonable projections for 20-30 years in the future. A future scenario analysis for central (~50,000 kg-H_2/day, located at the wind farm site) hydrogen production from electrolysis is used from Ramsden et al. [78] to make an equivalent comparison; this analysis assumes a 44.7 kWh/kg-H_2 electricity input (~80% electricity-to-hydrogen conversion efficiency) and an installed electrolyzer cost of 360 \$/kW. Using an electricity feedstock cost of 0.08 \$/kWh and a capacity factor of 90%, the hydrogen production cost is 4.5 \$/kg-H_2 or 4.2 \$/GGE (HHV basis). A 90% capacity factor is used here just for comparison of these pathways which all rely on the this factor.

The same assumptions can be used to analyze the cost of SNG and liquid fuels production. For a 4.5 \$/kg-H_2 production cost with a 0.9 \$/kg-H_2 cost to pipe the hydrogen to the SNG plant (100 mile pipeline transport [41]), the feedstock cost for the SNG plant is 5.4 \$/kg-H_2. The production cost for SNG using a hydrogen feedstock cost of 5.4 \$/kg and a 90% capacity factor is 58.7 \$/MMBTU or 7.3 \$/GGE. Using 0.08

$/kWh for the electricity feedstock cost and capacity factor of 90%, the cost of liquid fuels production is 9.7 $/GGE. Table 5.1 summarizes the production costs and location of production for this case study. These costs can then be used with a delivery cost estimation to determine the cost for the end-user.

Table 5.1 Fuels production case study: costs and location of production

Fuel	Production Cost ($/GGE)	Location of Production
SNG	7.3	City-gate
Gasoline & Diesel	9.7	Wind farm (100 miles from city-gate)
Central Hydrogen[a]	4.2	Wind farm (100 miles from city-gate)

[a] The plant for large-scale, central hydrogen production was not modeled in this thesis. The analysis was made by Ramsden et al. [78], using an equivalent feedstock cost and capacity factor.

5.3.1 SNG Delivery Cost

There are two main costs associated with the consumer price of natural gas: the commodity (the gas itself, or the production of the gas), and the transmission and distribution costs. Data from the Energy Information Agency (EIA) indicates that roughly 45% of the natural gas price to the consumer is due to the transmission and distribution costs. This cost is for the delivery from the city-gate to the end-user, so it is accurate to estimate that the same cost would be added to the SNG for delivery from the city-gate (where the SNG plant is located) to the consumer. It would be an overestimation to assume that the delivery cost is 45% of the SNG production cost because the SNG production cost in much higher than natural gas at present. The average city-gate price of natural gas in the U.S. is approximately 5.5 $/MMBTU, and the residential consumer price is approximately 10-11 $/MMBTU (2011 EIA data); the cost of SNG delivery is estimated to be 5 $/MMBTU.

In addition to standard delivery to residential and commercial end-users (for heating, and cooking appliances), natural gas can be supplied to the vehicle fleet which uses compressed natural gas as a fuel. An estimated natural gas dispensing cost of 2.5 $/MMBTU (from EIA) is allocated to the fueling station expenses. To use the produced SNG for the transportation sector, an estimated 7.5 $/MMBTU (includes the 5

\$/MMBTU for delivery to the fueling station) or 0.93 \$/GGE is added on to the cost of SNG production. In order to compare the fuels on a consistent basis, the cost for SNG distribution and dispensing to the transportation market should be added. For this case study, the delivered cost of SNG is 8.2 \$/GGE.

5.3.2 Gasoline & Diesel Delivery

The price of gasoline and diesel for the consumer also has a delivery cost component. It is estimated by the EIA that the delivery and marketing component, including tanker transport and fueling station costs, contributes about 10% of the gasoline price paid by consumers. With increasing crude oil prices, this percentage will decrease slightly. Assuming a conventional gasoline price of 3.5 \$/GGE, the delivery cost contributes about 0.35 \$/GGE; this is a reasonable estimate for the delivery cost of the F-T gasoline and diesel fuels. The distance traveled by gasoline tanker trucks from crude oil refineries to fueling stations is potentially much greater than that for distributed production from the F-T liquid fuels plant in this study, which would make the delivery costs proportionally less. Assuming the 0.35 \$/GGE delivery cost, this represents a relatively small fraction of the total F-T liquid fuels cost. The estimated total cost for delivered liquid fuels (to the consumer) is 10.0 \$/GGE.

5.3.3 Hydrogen Delivery

Yang et al. [79] estimated the additional costs associated with hydrogen delivery from a centralized production facility (e.g. at the wind farm site), including transmission (long distance, simple transport), distribution (complex network dispersal to multiple fueling stations), and dispensing (fueling stations) costs associated with a hydrogen infrastructure. The study assumes that the hydrogen-powered fuel cell vehicle fleet and hydrogen fueling stations are abundant, and the process for construction is mature. The total delivery costs associated with transmission (0.4-4.2\$/kg-H_2), distribution (1.0-4.4\$/kg-H_2) and dispensing (0.4-0.9 \$/kg-H_2) amount to 1.8 to 9.5 \$/kg-H_2 or 1.7 to 8.8 \$/GGE; these cost ranges are from various scenarios (hydrogen demand, city size, population density, etc.) analyzed by Yang et al. [79] for fueling station sizes in the range of 500-3000 kg-H_2/day. It is likely that the hydrogen delivery costs are closer to the upper-end of this range while the hydrogen demand (for fuel cell vehicles) is low. Table 5.2 summarizes the production costs and the delivered costs of the fuels; the hydrogen delivered cost includes the range of delivery costs from Yang et al. [79].

Table 5.2 Production and delivered cost for fuels

Fuel	Production Cost (\$/GGE)	Delivered Cost (\$/GGE)
SNG	7.3	8.2
Gasoline & Diesel	9.7	10.0
Central Hydrogen	4.2	5.9-13.0

The cost for hydrogen delivery which equates the delivered hydrogen cost with the delivered SNG and liquid fuels costs is 4.0 and 5.8 $/GGE, respectively; these values fall near the center of the delivery cost range predicted by Yang et al. [79] for a full scale hydrogen infrastructure, which is not in place currently. To this end, the SNG and liquid fuels have an advantage compared to hydrogen production based on the added expense for hydrogen delivery and the existing market for the fuels.

Figure 5.3 illustrates the delivered fuel cost of the SNG, F-T liquid fuels, and hydrogen from central electrolysis. The range of delivered hydrogen cost captures the range of delivery cost estimates from Yang et al. [79].

From Figure 5.3, the top x-axis range corresponds to the production cost for hydrogen from the central electrolysis plant, and this value, along with the pipeline transmission cost from the electrolysis plant to the SNG plant, is used for the SNG feedstock cost range. This plot illustrates the case study results for a range of feedstock costs, where there is synergy between the hydrogen source for the SNG plant and the production cost for the electrolysis plant. The gasoline and diesel costs are within the range of delivered hydrogen costs, but the gap between the upper end of the delivered hydrogen cost and the delivered cost for the liquid fuels decreases as the feedstock cost increases (electricity cost range of 0-0.14 $/kWh is shown); this is indicative of the higher efficiency conversion of the electrolysis plant (80%) compared to the co-electrolysis and F-T synthesis plant (50%).

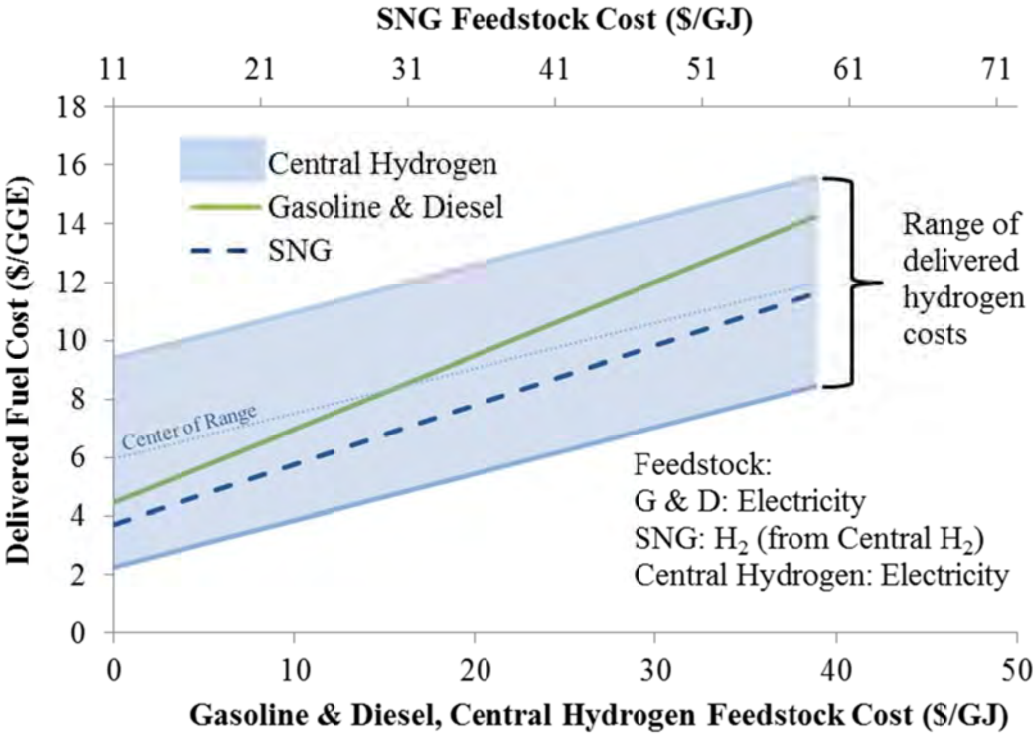

Figure 5.3 Delivered fuel cost dependence on feedstock cost. The range for hydrogen delivered from central electrolysis is shown. The top x-axis corresponds to the SNG feedstock (hydrogen produced from the central electrolysis) for SNG production.

The delivered SNG cost range is near the low end of the delivered hydrogen cost for low feedstock costs, and it increases to just below the average of the hydrogen delivered costs for high feedstock costs. While the central electrolysis plant is feeding the SNG plant hydrogen, the SNG plant efficiency of 78% (HHV) is decreasing the energetic content of the intermediate hydrogen, making it less cost effective to avoid the hydrogen delivery through conversion to SNG. However, the SNG delivery cost is less than hydrogen for the range shown, so it is more cost effective to convert the hydrogen to SNG than it is to produce and deliver the hydrogen directly.

5.3.4 Distributed SOFC CHHP Hydrogen Production

The comparison of centralized hydrogen production and distributed hydrogen production from the proposed SOFC CHHP plant (Chapter 4) can also be made to identify the advantage avoiding the hydrogen transmission and distribution costs. The advantage of eliminating the majority of the delivery costs is apparent from the findings in Yang et al. [79]. The additional dispensing cost would still be applied to the SOFC system to construct and maintain a fueling station, but this only adds 0.4-0.9 $/kg-H$_2$ to the production cost.

It is difficult to make an equivalent comparison of central hydrogen production and distributed hydrogen production because the two scenarios are producing to a different size market. The central production is much larger scale with the aims to supply a large demand. If the demand does not exist, there is no value for the fuel product. Conversely, if there is no production available, then there is no incentive to create the demand infrastructure (e.g. there is no motivation for manufacturers to produce fuel cell vehicles if there is no hydrogen to fuel them). This is termed the “chicken and egg” problem. There must be a fuel supply and a fuel demand to kick-start the growth of a transportation market such as hydrogen and fuel cell vehicles. Small-scale hydrogen production could help solve this dilemma, especially if other co-products can be produced in place of hydrogen when the demand is temporarily low. The SOFC CHHP plant can produce hydrogen when it’s needed, and it can divert the tail-gas directly to the combustor to generate additional heat when there is no demand; this would also eliminate the need for large amounts of hydrogen storage at the fueling station.

As shown in Chapter 4, the hydrogen production from the SOFC CHHP plant is highly dependent on the methane feedstock cost and the electricity credit price. For a methane feedstock cost of 10 $/MMBTU and an electricity credit price of 0.10 $/kWh, the hydrogen production cost is 4.5 $/kg, which is the same price as the central hydrogen production from electrolysis (case study described above); this hydrogen is already at the location of the filling station, so it represents cheaper hydrogen for the consumer (by 1.4-8.6 $/kg-H$_2$) than producing it at the central production plant. The methane feedstock of

10 $/MMBTU is equivalent to the current price of fossil natural gas (EIA, 2011), so the hydrogen production is not renewable in this scenario.

Another small-scale, non-renewable strategy to produce hydrogen is steam methane reforming (SMR) with subsequent hydrogen purification. This strategy could produce hydrogen at a similar scale as the SOFC CHHP system, but the only function of the SMR system is to produce hydrogen. If there is a shortage of demand for the hydrogen, the system would need to be shut down or implement enough on-site storage of the excess hydrogen for continuous production. By shutting the system down, the operating capacity decreases, and the capital investment increases relative to the production. On-site storage is energy intensive and expensive due to the high pressure compression needed for adequate volumetric energy density and the need for thick-walled, non-corrosive storage vessels. The SOFC CHHP system could mitigate these issues due to its production of multiple co-products. With a temporary low demand for hydrogen, the system could increase the fuel utilization to produce more electricity, or it could produce more heat by combusting the SOFC effluent.

It has been noted that the unit cost of hydrogen should be lower for fuel cell-based distributed polygeneration systems, because the capital investment is leveraged across all co-products. This claim is examined more closely by comparing hydrogen production costs via other pathways, as shown in Table 5.3. At distributed-scales (~250 kg/day), SMR-based hydrogen production cost has been estimated at 3.5 $/kg and around 4.17 $/kg for distributed electrolysis plants (~1050 kg/day scale). In the present study, the SOFC CHHP plant generates hydrogen at a comparable cost of 4.4 $/kg, which is about 25% higher than SMR-based hydrogen production. As with distributed electrolysis systems, hydrogen production from fuel cell-based CHHP plants is sensitive to grid electricity prices (sell-back). Therefore, fuel cell-based polygeneration plants are shown to have hydrogen production costs that are on par with conventional and alternative pathways (although not necessarily cheaper) while providing power and thermal energy commodities.

Table 5.3 Comparison of distributed hydrogen production costs

Hydrogen Production Pathway[1]	$/kg
SMR of natural gas (distributed-scale[2])	3.5 [80]
Electrolysis (distributed-scale[2])	4.17 [82]
SOFC CHHP System (distributed-scale[2,3])	4.4

[1] Distributed-scale hydrogen cost is estimated from ~250 kg/day production values for SMR and SOFC CHHP and 1050 kg/day for grid-powered electrolysis. A capacity factor of 90% is used for all cases.

[2] Distributed scale hydrogen cost subtracts out an estimated 4.03 $/kg for compression, storage, and dispensing [81] and 1.88 $/kg for electrolysis [82].

[2] Price of natural gas feedstock is $7/MMBtu (0.024 $/kWh) and electricity sell-back of 0.082 $/kWh.

The SOFC CHHP system is an example of a high efficiency electricity generator with heat and hydrogen co-products. While the economics of such a system are only competitive using fossil fuel natural gas equivalent feedstock costs, the system lowers the overall fuel consumption with high efficiency fuel-to-electricity conversion and offers a transitional supply of hydrogen for fuel cell vehicles. The small-scale supply could give hydrogen-powered fuel cell vehicle manufacturers the opportunity to compete with the current fleet of internal combustion engine vehicles.

CHAPTER 6

CONCLUSIONS

The analysis of alternative pathways to fuels broadens the spectrum of renewable energy deployment options. Fuel production is one way to capture and store the electric power produced from renewable energy resources, such as wind. Energy storage is an important aspect of harnessing renewable energy as it becomes available, thereby increasing the power density of land-intensive generation technologies (e.g. wind turbines and solar panels). The development and integration of renewable energy into the existing infrastructure is a major challenge. This thesis presents two pathways to fuels for which there is an existing demand and one pathway for which the gap between supply and demand is moderated. Fossil fuels will eventually run out, and investigating alternative fuel production pathways is important to determine suitable replacements to fossil fuels in a growing energy market.

6.1 Summary of Findings and Conclusions

This thesis focused on production scales which could be accommodated by renewable resources, such as wind. Two pathways for the production of SNG and F-T gasoline and diesel were presented. The SNG plant used hydrogen as an intermediate energy carrier for the subsequent conversion to SNG. The co-electrolysis plant utilized the electric power generation directly to produce gasoline and diesel fuels. The capture and recycle of carbon dioxide is used as the carbon source for both of these fuel production plants. A third production plant is presented which employs small-scale hydrogen production by using SOFC polygeneration. The gap between supply and demand of hydrogen for FCVs is moderated through the use of polygeneration, whereby the capital investment is leveraged across all co-products.

6.2 Summary and Implications of Pathways

It is not suggested that the production plants explored in this thesis are holistic solutions to renewable energy integration within the transportation market or the replacement of fossil fuels. It is evident from the limited scale and locations in which these plant are feasible (e.g. near a strong wind resource) that they can only be *part* of the solution. The geographic regions which have strong wind resources tend to be less populated than those without, so the potential to harness and store the wind resource, when it cannot be directly used as electricity, is an important aspect of increasing the value of the wind turbines.

A source for the carbon dioxide is also needed, and there are very limited sources at present because carbon capture is not incentivized. The carbon capture and storage (CC&S) process is energy intensive, and the technology must improve to make it more efficient and cost effective. Different sources and methods for power generation (e.g. biomass gasification) will make the CC&S process easier and more cost effective, thus increasing the potential sources of carbon dioxide. It is assumed that future governmental policy will place more value on mitigating the harmful environmental effects of burning fossil fuels.

While the fuel production plants presented in this thesis are not going to be built in the next 10-15 years, the modeling and simulation efforts give insight into system level design considerations. The following conclusions are made based on the design considerations explored for the fuel production plants. A discussion on future work for each production pathway is given.

6.2.1 SNG Production Plant

Thermodynamic and kinetic considerations of the methanation reaction were explored to model and simulate a system of reactors for the conversion of hydrogen and carbon dioxide to SNG. Reactor design is important to maximize the conversion of carbon dioxide by maintaining optimal reaction temperatures. Heat integration and recovery is a crucial part of plant operation when highly exothermic reactions, such as methanation, are involved. Multiple reactor stages are also necessary to condense and purge the produced water from the process stream, thereby promoting the methanation reaction; this is thought to be a main driving force for the conversion of carbon dioxide. Multiple reactors increase the per-pass conversion of the reactor train, thereby allowing the separation and recycle processes to produce an SNG composition which is adequate for natural gas pipeline transport and end-use applications. Inter-stage heat recovery is used, and organic rankine cycles (ORC) are ideal candidates for producing electricity from low temperature waste-heat. The ORC units supplied all of the internal electricity needs, which enable the plant to operate without reliance on the grid. Separation processes were investigated to recycle the reactant species and increase overall reactant conversion. Conventional separation technologies were found to adequately produce SNG with high methane content while limiting the amount of carbon dioxide in the product.

There are no previous studies which model the production of SNG from hydrogen and carbon dioxide in a process similar to that which is presented in this thesis. The SNG production plant is a unique analysis, so there are no benchmark studies from which to compare the results. The plant model was reviewed and validated by an expert in the natural gas processing industry as well as other sources with industrial chemical processing experience. Many laboratory studies are presented in the literature which attempt to characterize the reaction kinetics of carbon dioxide methanation, but there is a large gap between these studies and large-scale reactor performance for carbon dioxide methanation. The SNG plant in Chapter 2 characterizes the synergies between large-scale reactors, thermal management, and system level design considerations.

The overall plant efficiency of this process is 78.1% HHV. The SNG production cost ranges from 8 to 80 \$/MMBTU based on the range of hydrogen feedstock costs relevant to renewable production from wind-powered electrolysis and operating capacity factors; for each 1 \$/kg of hydrogen feedstock cost, the SNG production cost increases 9.4 \$/MMBTU.

6.2.1.1 Implications for Future Work

The main source of uncertainty of the SNG plant is the reaction kinetics of the carbon dioxide methanation reaction. Future experimental work is warranted to design and test a large-scale reactor with thermal management (cooling). A two-dimensional model employing reaction kinetics, fluid dynamics, and heat transfer properties would give additional insight into the design of such a reactor and the implementation of a suitable catalyst.

The feasibility of the SNG plant from Chapter 2 is mainly dependent on obtaining a cheap hydrogen source. Hydrogen production will not be cheap in the near-term, so producing SNG that can compete in the near-term energy market is not likely without substantial financial incentives for renewable energy and carbon emission mitigation. Natural gas is a relatively cheap commodity, so the renewable SNG has a disadvantage compared to gasoline and diesel fuels, which are higher priced fuels (comparing $/energy). The conversion efficiency for the SNG plant is relatively high at 78% HHV, and the capital costs are small compared to the hydrogen feedstock cost; this implies that future work should focus on realizing a cheap source of hydrogen.

From the economic evaluation of this pathway to SNG, it is not predicted that such a process will become economically competitive because of the low cost of natural gas at present. Although there is uncertainty in the methanation reactor performance, it should be noted that all of the process technologies are commercially available for this pathway. While not competitive with natural gas prices, the conversion of hydrogen to SNG was shown to be more cost effective than producing and delivering hydrogen from Chapter 5.

6.2.2 Gasoline & Diesel Production Plant

A thermochemical model for the conversion of SOEC derived syngas to liquid fuels via F-T synthesis and product upgrading was presented. SOEC systems have not been deployed at industrial scales, but laboratory studies have shown their potential for high efficiency conversion of steam and carbon dioxide to highly reactive syngas. F-T synthesis and product upgrading are technologically mature processes which are used in select locations for large scale liquid fuel production (e.g. Sasol in Africa). Prior to this effort, there have been no modeling studies which combine the two major subsystems of SOEC co-electrolysis and F-T synthesis. The present study gives insight into the synergies between the syngas generation and F-T synthesis subsystems, and the resulting electricity-to-liquid fuels conversion efficiency represents a realizable process.

The performance model for the SOEC co-electrolysis module was based on experimental data, and the model was extended to account for the methanation reaction at elevated operating pressures. The sensitivity analysis on the component level SOEC model was carried out with the goal of determining optimal operating conditions to produce syngas which is most beneficial for the performance of the F-T synthesis reactor. System level analysis determined the effects of operating the SOEC at elevated pressures; it was found that the negative effects of operating the SOEC module at elevated pressures (increased methane production and lower current density) outweighed the positive effects of decreased SOEC power requirement and decreased downstream compression power for the F-T reactor feed gas.

The model for the F-T synthesis reactor employed a cobalt-based catalyst for which high per-pass conversion can be obtained. The performance estimation of carbon monoxide conversion is relatively high (70%), but the reactor operating conditions (high pressure and a high syngas concentration) achieved by the SOEC module and compression allows for high conversion.

The system model resulted in an overall electricity-to-liquid fuels efficiency of 50.1% HHV (46.3% LHV). The scenario of operating the SOEC at 5 bar results in an overall efficiency that is 2.7% lower than operation at 1.6 bar. The liquid fuels production costs range from 5.8 \$/GGE to 18.2 \$/GGE for the explored range of electricity feedstock costs and operating capacity factors. For every 0.01 \$/kWh of electricity feedstock cost, the cost of liquid fuels production increases about 0.7 \$/GGE.

The feasibility of the gasoline and diesel production plant from Chapter 3 is highly dependent on obtaining a cheap price of renewable electricity and maintaining a high operating capacity. These conditions are only obtainable in select locations, where there is a large wind farm and a low demand for the electricity nearby. In certain scenarios, it may be more cost effective to use the electricity onsite for co-electrolysis than it is to transport the electricity long distances and suffer losses from the transmission lines. Regarding capacity factor, the plant would benefit from being powered by a much larger (e.g. greater than 100 MW) wind farm than the maximum capacity of the plant (e.g. 50 MW) so as to supply the most electricity when the wind farm is not running at maximum capacity. The capital cost of the plant is largely dominated by the cost of the SOEC unit, for which the assumption of technological maturity and a high manufacturing capacity was made. It is imperative that SOEC co-electrolysis technology and manufacturability improve to achieve the performance and unit costs assumed in this study.

6.2.2.1 Implications for Future Work

High temperature co-electrolysis is a promising technology, but much research and development is still required to transform the laboratory-tested modules into a commercially available technology. The technology could benefit from one and two-dimensional models which simulate the chemical reactions, fluid dynamics, and heat transfer characteristics of the stack. Further understanding from these models would give insight into the relative reaction mechanisms of steam and carbon dioxide in the stack. The present study estimates a relatively high performance SOEC module using a zero-dimensional model, but realization of this performance will require technological advancement; this advancement is currently under research by several institutions (e.g. INL, Risø National Laboratory, Ceramatec™)

The present study conducted a sensitivity analysis of SOEC operating conditions (temperature, pressure, voltage) on the product syngas composition. A high pressure case study was explored to realize the system level effects. Future work could involve developing the model for more robust system level sensitivity analysis to explore the system level effects for the entire range of SOEC operating conditions. An additional sensitivity analysis on the effect of carbon monoxide conversion in the F-T synthesis reactor could also be explored along with the possibility of F-T product recycle to achieve higher overall conversion to hydrocarbons. The current model is capable of determining the system results of one set of operating conditions (e.g. T_1, P_1, V_1) at a time, but manual adjustments must be made to the system model to ensure certain constraints are met. For example, the amount of LFG diverted to the PSA for hydrogen production must satisfy the product upgrading requirements *and* the SOEC feed gas requirements without producing in excess. Meeting this constraint is not currently automated in the Aspen Plus™ model, so manual adjustments must be made. The upgrading of the present system-level automation, along with a more detailed SOEC component model, would provide a highly versatile system model with high fidelity.

Heating the SOEC reactant gas stream to 800 °C is an energy intensive process, so it is suggested to explore the integration of high temperature co-electrolysis with another process which has a high temperature heat source. It is necessary for the production plant to have a self-sustaining heat source (internally produced LFG) when operating at a remote wind farm location, but the coupling of this plant with a high temperature heat source would alleviate this constraint. Employing high temperature co-electrolysis with a larger, more constant source of electricity, such as a nuclear power plant, would benefit from: i) a high operating capacity factor, ii) a high temperature heat source, iii) economy of scale and iv) enabling the use of LFG in a gas turbine for electricity generation or reforming it to syngas to be recycled for additional F-T synthesis. Coupling high temperature co-electrolysis with heat and electricity produced by a nuclear power plant has been studied by O'brien et al. [43], but further analysis can be made by exploring the synergies between the co-electrolysis, F-T synthesis, and product upgrading subsystems.

6.2.3 Hydrogen Production

The final study aimed to demonstrate the potential benefits of hydrogen co-production from an SOFC system. The unique aspect of this plant, compared to other co-generating fuel cell systems, is the separation of hydrogen which could be used for FCVs. SOFC systems with co-generation are known to exhibit high overall efficiency, and this study characterized the potential for a relatively new technology (EHS) to separate hydrogen from SOFC effluent gas streams. The conventional method for hydrogen separation using pressure swing adsorption (PSA) was also evaluated for comparison to EHS. PSA is a commercially available technology which is commonly used for separating hydrogen from SMR effluent streams, and the product hydrogen can achieve purity levels suitable for use in PEM FCVs. PSA separation performance degrades if the feed gas has a low concentration of hydrogen, which is the case for the anode effluent of an SOFC. Hydrogen separation performance using EHS units is much less dependent on the hydrogen concentration, and EHS can achieve a high degree of separation using less electrical energy than the PSA process.

The exploration of system level synergies between the SOFC performance, hydrogen separation units, and heat recovery is unique to this study. The case study for hydrogen overproduction exemplifies the advantage of the modeling the entire system; both of the analyzed hydrogen separation design concepts resulted in increased overall efficiency for several reasons: i) higher SOFC operating voltage, ii) lower cathode air flow requirement, iii) less additional methane for the combustor was required to accomplish fuel preheat, and iv) the PSA separation efficiency increased. Despite the increase in hydrogen separation efficiency for the PSA concept in the hydrogen overproduction case study, the EHS unit is more suitable than PSA for hydrogen separation from SOFC tail-gas.

The overall fuel efficiency for the SOFC CHHP plant is 79.3% HHV for the EHS concept. The range of hydrogen production costs from this plant is 4 to 11 \$/kg-H_2 based on the relevant range of methane feedstock costs and electricity credit prices. For each 1 \$/MMBTU of methane feedstock cost, the hydrogen production cost increases by about 0.67 \$/kg. In a location with significantly lower natural gas prices than electricity, hydrogen production can be achieved at less than 2 \$/kg.

6.2.3.1 Implications for Future Work

The main source of uncertainty in the present study is the performance and development of the EHS technology. Although EHS units are predicted to perform well under the aforementioned conditions, they have yet to be demonstrated at commercial scales (>100 kg-H_2/day). Further demonstrations of EHS technology from manufacturers will serve to validate the hydrogen separation performance and product purity.

Several steps could be taken to further the development of the current model. The hydrogen over-production case study makes several assumptions that potentially over-predict the system performance, which showed an increase in overall efficiency compared to the baseline case. The case study assumed that the system components are the same as those in the baseline case (e.g. the size of the SOEC, EHS, and PSA modules). The EHS overpotential could increase due to the effective ASR of the stack when operating at a higher current density. The PSA performance may also decrease because there is not as much membrane surface area onto which the non-hydrogen molecules adsorb, and this could lead to a decrease in hydrogen purity. The implementation of performance curves for the EHS and PSA would make the model more robust for sensitivity analyses such as flow rate and fuel utilization variations.

The economic feasibility of hydrogen production from the SOFC CHHP plant is dependent on the market value of hydrogen and relative price of electricity and methane in the selected location. To generate hydrogen cheaply in the near-term, the range of methane feedstock costs must be similar to the current price of natural gas. While this would not be a renewable pathway to hydrogen, it would offer the transitional supply of hydrogen using a highly efficient conversion of the natural gas to allow the fuel cell vehicle fleet a chance to grow.

6.3 Socio-Economic and Environmental Considerations

While this section does not aim to quantify the scenarios for carbon taxation, emissions trading, and subsidies, a discussion is warranted on socio-economic and environmental considerations, including the avoided carbon emissions and governmental policy implications for renewable energy.

Placing a value on the carbon dioxide that is recycled by the fuel production plants discussed in Chapters 2 and 3 would benefit the economics of the pathways. This value would represent the avoided external costs of burning fossil fuels, such as pollution and climate change, which are not currently included in the cost of fossil fuels.

The SNG and F-T liquid fuel production costs using the feedstock cost ranges for renewably generated hydrogen and electricity are not economically competitive with existing fossil-derived fuel prices. There are attributes of the renewable fuel products that could incur cost reductions from government incentives. The renewable fuels are produced using carbon dioxide that would have otherwise been emitted to the atmosphere. All of the carbon dioxide feedstock (~80,000 tonne/yr) from the SNG production can be considered greenhouse gas emissions (GHG) reductions compared to natural gas use. Similarly, the gasoline and diesel fuels produced from recycled carbon dioxide (~120,000 tonne/yr) represent significant reductions in GHG emissions compared to petroleum derived gasoline and diesel fuels. While the carbon dioxide feedstock does not represent a significant cost for the SNG or liquid fuels production, the environmentally benign aspects of these processes could be rewarded by governmental policy in the future.

The product costs could benefit from a cap and trade scenario for carbon dioxide. Since the carbon dioxide is recycled, there would be substantial ‘credits’ earned by the fuels production plants. The credits represent the avoided carbon dioxide emissions that would have otherwise been emitted to the atmosphere in comparison to fossil fuel use. Similar to earning credits, a tax on carbon emissions would also make the source for carbon dioxide more available because power plants would have economic motivation to capture it. This would increase the feasible locations for the construction of fuel production plants which utilize recycled carbon dioxide.

The EIA estimates that direct subsidies for fossil fuels amounted to $313 billion in 2009 (world-wide); this does not include indirect subsidies such as tax expenditures, military expenses for securing resources, and under-priced access to scarce resources (e.g. land under governmental control) , which are harder to quantify. In addition, the effects of burning fossil fuels include air quality degradation, water contamination, and climate change which place an indeterminate socio-economic burden on society and the Earth. The total renewable energy subsidies were estimated to be $57 billion (includes $20 billion for biofuels) from a 2009 EIA report. While renewable energy generates far less chemical and electric power at present (the $/kWh for fossil fuel subsidies is less than that of renewable energy), it is clear that the removal of fossil fuel subsidies will have a positive impact on the economic competitiveness of renewable-based generation facilities.

It is clear that renewable resources such as wind are stronger in certain locations than others, but there are also geo-political considerations which affect the viability of the presented pathways. In the U.S., crude oil commodities such as gasoline and diesel are not taxed as heavily as they are in Europe (tax accounts for about 70% of the total consumer cost at the pump, compared to about 10% in the U.S.). Therefore, gasoline and diesel prices are high in Europe compared to the U.S (about twice as high). Locating the liquid fuel production plant from Chapter 3 in a favorable Europe country makes it much more economically attractive. High renewable power availability (high capacity factor) would make the liquid fuel products competitive in the near-term, assuming they are not taxed the same as fossil fuels.

In addition to concerns of carbon emissions, the fact that the world has a limited supply of fossil fuels provides motivation to explore various alternatives for fueling the energy market. It is clear than there will not be only one technology that replaces fossil fuels with a sustainable alternative. There is much uncertainty in the future technologies and pathways that will provide fuels for the transportation market. Hydrogen is the most heavily researched chemical for use as a renewable energy carrier, and it is proposed that it can potentially supply most of the world's energy needs in a "hydrogen economy". It is clear the hydrogen economy is a long-term prospect, and there must be other mid- to near-term strategies of integrating renewable energy into the existing infrastructure.

6.4 Final Statements

This thesis presents two renewable pathways to SNG and F-T liquid fuels for use in the existing energy infrastructure. A distributed polygeneration plant, which could provide hydrogen fuel as a means to supply a potential market for fuel cell vehicles, is also presented. The question of whether or not the hydrogen economy will come to fruition is not predicted or suggested in this thesis, but several potential pathways are explored for increasing renewable energy penetration into the existing transportation sector without the need for large scale hydrogen vehicle deployment. The advantage of producing fuels for which there is an existing demand leverages the value of the renewable energy source. Small-scale hydrogen production as a co-product of an SOFC electricity generator captures the benefits of high efficiency conversion while allowing a potentially renewable transportation fleet of fuel cell vehicles to evolve. This thesis quantifies the performance and economics of various fuel production pathways to broaden the potential for renewable energy integration in our society.

REFERENCES CITED

[1] Tripati, A.K., Roberts, C.D., Eagle, R.A., Li, G., 2011. A 20 million year record of planktic foraminiferal B/Ca ratios: Systematics and uncertainties in pCO2 reconstructions, Geochimica et Cosmochimica Acta, 75(10):2582-2610

[2] University of California - Los Angeles, 2009. Last Time Carbon Dioxide Levels Were This High: 15 Million Years Ago, Scientists Report. ScienceDaily. Retrieved July 2, 2011, from http://www.sciencedaily.com /releases/2009/10/091008152242.htm

[3] NREL GIS Wind Resource Data & Map. Available at: http://windpoweringamerica.gov/wind_maps.asp.

[4] NREL GIS Natural Gas Pipelines and Power Plants Data & Map. Permission of use by Michael Penev.

[5] Parker, N., 2004. Using Natural Gas Transmission Pipeline Costs to Estimate Hydrogen Pipeline Costs. Institute of Transportation Studies. U. Cal. Davis Report: UCD-ITS-RR-04-35.

[6] Mintz, M., Folga, S., Molburg, J., Gillette, J., 2002. Cost of Some Hydrogen Fuel Infrastructure Options", Argonne National Laboratory: Transportation Research Board presentation.

[7] Dean, J., Braun, R., Penev, M., Kinchin, C., Munoz, 2010. Leveling intermittent renewable energy production through biomass gasification-based hybrid systems. ASME 4th International Conference on Energy Sustainability: ES2010-90067.

[8] Gassner, M., Marechal, F., 2008. Thermo-economic optimisation of the integration of electrolysis in synthetic natural gas production from wood, Energy, 33(2):189-198.

[9] Larson, E.D., Jin, J., Celik, F.E., 2005. Gasification-Based Fuels and Electricity Production from Biomass, without and with Carbon Capture and Storage. Princeton U., Princeton, NJ & Dartmouth College, Hanover, NH. Technical Report.

[10] Graves, C., Ebbesen, S.D., Mogensen, M., Lackner, K.S., 2011. Sustainable hydrocarbon fuels by recycling CO2 and H2O with renewable or nuclear energy, Renewable and Sustainable Energy Reviews, 15(1):1-23.

[11] Colella, W., Rankin, A., Margalef, P., Sun, A., Brouwer, J., 2009. Thermodynamic, Economic, and Environmental Modeling of Hydrogen (H2) Co-Production Integrated with Stationary Fuel Cell System (FCS). DOE Hydrogen Program: FY 2009 Annual Progress Report.

[12] Sirohi, V.P., 1978. Fixed Bed Methanation Processes: Final Report. Department of Energy and C. F. Braun & Co., Alhambra, CA.

[13] Kertamus, N.G., 1978. Combined Shift-Methanation Processes: Final Report. Department of Energy and C. F. Braun & Co., Alhambra, CA.

[14] Dirksen, H.A., Linden, H.R., 1963. Pipeline Gas from Coal by Methanation of Synthesis Gas. The Gas Operations Research Committee of the American Gas Association, Illonois.

[15] Zahnstecher, L.W., 1984. Coal Gasification via the Lurgi Process, Topical Report Volume 1: Production of SNG. DOE contract No.: DE-AC01082FE05081.

[16] Seglin, L., Geosits, R., Franko, B.R., Gruber, G., 1974. Methanation of Synthesis Gas. Ch. 1: Survey of Methanation Chemistry and Processes.

[17] Panek, J.M, Grasser, J., 2006. Practical Experience Gained During the First Twenty Years of Operation of the Great Plains Gasification Plant and Implications for Future Projects. DOE Office of Fossil Energy: Technical Report.

[18] Wang Q., Gong J., 2011. Methanation of carbon dioxide: an overview. Chem. Sci. Eng. 5(1):2-10.

[19] Twygg, M., 1997. Catalyst Handbook. 2nd Edition. Oxford University Press.

[20] Rostrup-Nielsen, J.R., Pedersen, K., Sehested, J., 2007. High Temperature Methanation Sintering and Structure Sensitivity, Applied Catalysis A: General 330:134-138.

[21] Chlang, J.H., Hopper, J.R., 1983. Kinetics of the hydrogenation of carbon dioxide over supported nickel, Ind. Eng. Chem. Prod. Res. 22(2).

[22] Saletore, D.A., Thomson, W.J., 1977. Methanation reaction rates for recycle reactor compositions, Ind. Eng. Chem. Process Des. Dev. 16(1)

[23] Hoekman, S.K., Broch, A., Robbins, C., Purcell, R., 2010. CO_2 recycling by reaction with renewably-generated hydrogen, Int. J. Greenhouse Gas Control 4(1):44-50.

[24] Habazaki, H.,Yamasaki, M., Zhang, B-P., Kawashima, A., Kohno, S., Takai, T., Hashimoto, K., 1998. Co-methanation of carbon monoxide and carbon dioxide on supported nickel and cobalt catalysts prepared from amorphous alloys, J. Catalysis, 62:349-356.

[25] Maatman, R., Hiemstra, S., 1980. A kinetic study of the methanation of CO_2 over nickel-alumina, J. Catalysis, 62(2):349-356.

[26] Weatherbee, G.D., Bartholomew, C.H., 1982. Hydrogenation of CO2 on group VIII metals : II. kinetics and mechanism of CO2 hydrogenation on nickel, J. Catalysis 77(2):460-472.

[27] Helfrich, D., 2010. Sud-Chemie: industrial quote for methanation catalyst composition and cost: SNG 1000. April.

[28] Borkink J.G.H., Westerterp K.R., 1992. Determination of effective heat transport coefficients for wall-cooled packed beds, Chemical Engineering Science 47(9):2337-2342.

[29] Spath P., Aden A., Eggeman T., Ringer M., Wallace B., Jechura J., 2005. Biomass to Hydrogen Production Detailed Design and Economics Utilizing the Battelle Columbus Laboratory Indirectly-Heated Gasifier, NREL Technical Report: TP-510-37408: 13.

[30] Stone, J., 2010. UTC Power: industrial quote for organic rankine cycle unit: efficiency and cost. May.

[31] Peters, M.S., Timmerhaus, K.D., West, R.E., 2003. Plant Design and Economics for Chemical Engineers, 5th ed., McGraw-Hill, New York. Ch. 6, 14.

[32] Kinay A., Parrish, W., 2006. Fundamentals of Natural Gas Processing. Taylor and Francis Group, LLC.

[33] Alie C., Backham L., Croiset E., Douglas P.L., 2005. Simulation of CO_2 capture using MEA scrubbing: a flowsheet decomposition method. Energy Conversion and Management 46: 475-487.

[34] Nextant, 2009. Task 2: Detailed MDEA Process Analysis. Prepared for DOE/NREL. NREL Task Order No. KAFT-8-882786-01.

[35] Ho, W., Sirkar, K., 1992. Membrane Handbook. 1st Ed. Springer.

[36] Baker, R.W., 2000. Membrane Technology and Applications. McGraw-Hill.

[37] Haeseldonckx, D., D'haeseleer, W., 2006. The Use of the Natural-gas Pipeline Infrastructure for Hydrogen Transport in a Changing Market Structure, J. Hydrogen Energy 32: 1381-1386.
[38] Industry review: Ray Hobbes (Hobbes Energy), Rich Bain (National Renewable Energy Laboratory), Christopher Kinchin (NREL), Michael Penev (NREL), Robert Braun (Colorado School of Mines).
[39] Newpoint Gas, LP, 2010. Amicalc™ amine plant sizing and costing software. http://www.newpointgas.com/downloads.php. Accessed: June 2010.
[40] Rubin, E.S., Chen, C. Rao, A.B., 2007. Cost and Performance of Fossil Fuel Power Plants with CO_2 Capture and Storage. Dept. of Engineering and Public Policy. Carnegie Mellon U. PA.
[41] U.S. DOE Hydrogen Program, 2010. Hydrogen production economics program. http://www.hydrogen.energy.gov/h2a_analysis.html. Accessed: June 2010.
[42] Steward, D., Ramsden, T., Zuboy, J., 2008. H2A Production Model, Version 2 User Guide. Technical report: NREL/TP-560-43983.
[43] O'Brien, J.M., McKellar, M.G., Stoots, C.M., Herring, J.S., Hawkes, G.L., 2008. Parametric study of large-scale production of syngas via high-temperature co-electrolysis, J. Hydrogen Energy, 34:4216-4226.
[44] Hamelinck, C.N., Faaij, A.P.C., den Uil, H., Boerrigter, H., 2004. Production of FT transportation fuels from biomass; technical options, process analysis and optimisation, and development potential, Energy, 29(11):1743-1771.
[45] Bechtel, 1998. Aspen Process Flowsheet Simulation Model of a Battelle Biomass-Based Gasification, Fischer-Tropsch Liquefaction and Combined-Cycle Power Plant, DOE Topical Report DE-AC22-93PC91029, Pittsburg, PA.
[46] Stoots, C.M., O'Brien, J.E., Hartvigsen, J.J., 2009. Syngas Production Via High-Temperature Coelectrolysis of Steam and Carbon Dioxide, J. Fuel Cell Science & Technology, 6.
[47] Timmermann, H., Sawady, W., Reimert, R., Ivers-Tiffee, E., 2009. Kinetics of (reversible) internal reforming of methane in solid oxide fuel cells under stationary and APU conditions, J. of Power Sources, 195:214-222.
[48] Gopalan, S., Mosleh, M., Hartvigsen, J., McConnell, R., 2008. Analysis of self-sustaining recuperative solid oxide electrolysis systems, J. Power Sources, 185:1328-1333.
[49] Jager, B., Espinoza, R., 1995. Advances in low temperature Fischer-Tropsch synthesis, J. Catalysis Today, 23:17-28.
[50] de Klerk, A., 2008. Hydroprocessing peculiarities of Fischer-Tropsch syncrude, Catalysis Today, International Symposium on Advances in Hydroprocessing of Oils Fractions, 130(4):439-445
[51] Iliuta, I., Larachi, F., Anfray, J., Dromard, N., Schweich, D., 2008. Comparative Simulations of Cobalt- and Iron-Based Fischer-Tropsch Synthesis Slurry Bubble Column Reactors, Ind. Eng. Chem Res 47:3861-3869.
[52] Leckel, D., 2010. Upgrading of Fischer-Tropsch Products to Produce Diesel. Sasol Technology R & D. Haldor Topsoe Catalysis Forum, August.
[53] Yates, I.C., Satterfield, C.N., 1991. Intrinsic Kinetics of the Fischer-Tropsch Synthesis on a Cobalt Catalyst, J. Energy & Fuels, 5:168-173.

[54] Botes, F.G., van Dyk, B., McGregor, C., 2009. The Development of a Macro Kinetic Model for a Commercial Co/Pt/Al2O3 Fischer-Tropsch Catalyst, Ind. Eng. Chem Res, 48:10439-10447.

[55] Espinoza, R.L., Steynberg, A.P., Jager, B., Vosloo, A.C., 1999. Low temperature Fischer-Tropsch synthesis from a Sasol perspective, J. Applied Catalysis, 186:13-26.

[56] Pipitone, G., Bolland, O., 2009. Power generation with CO2 capture: Technology for CO2 purification, Journal of Greenhouse Gas Control, 3:528-534.

[57] Gary, J.H., Handwerk, G.E., Kaiser, M.J., 2007. Petroleum Refining Technology and Economics, 5th Edition, Taylor & Francis Group, 6000 Broken Sound Parkway NW, Suite 300, Ch. 7.

[58] Gerdes K., Grol E., Keairns D., Newby R., 2009. Integrated Gasification Fuel Cell Performance and Cost Assessment. Technical Report: DOE/NETL-2009/1361. March.

[59] Encana, Dakota Gasification Company, 2008. Weyburn Enhanced Oil Recovery Project Summary. www.co2captureandstorage.info/project_specific.php?project_id=70. Accessed: May, 2011.

[60] Mitlitsky F., 2008, Low-cost Co-production of Hydrogen and Electricity, DOE Hydrogen Energy Program. Project ID #FC1.

[61] Perdikaris N., Panopoulos K.D., Hofmann P., Spyrakis S., Kakaras E., 2010, Design and Exergetic Analysis of a Novel Carbon Free Tri-Generation System for Hydrogen, Power and Heat Production from Natural Gas, Based on Combined Solid Oxide Fuel and Electrolyser Cells, International Journal of Hydrogen Energy, 35(6):2446-2456.

[62] Colella, W., Rankin, A., Margalef, P., Sun, A., Brouwer, J., 2009. Thermodynamic, Economic, and Environmental Modeling of Hydrogen (H_2) Co-Production Integrated with Stationary Fuel Cell System (FCS). DOE Hydrogen Program: FY 2009 Annual Progress Report.

[63] Lisbona P., Corradetti A., Bove R., Lunghi P, 2006. Analysis of a Solid Oxide Fuel Cell System for Combined Heat and Power Applications under Non-Nominal Conditions, Electrochimica Acta, 53(4):1920-1930.

[64] Costamagna P., Honegger K., 1998. Modeling of Solid Oxide Heat Exchanger Integrated Stacks and Simulation at High Fuel Utilization, J. of Electrochemical Society, 145(11):3995–4007.

[65] Costamagna P., Selimovic A., Borghi M.D., Agnew G., 2004. Electrochemical Model of the Integrated Planar Solid Oxide Fuel Cell (IP-SOFC), Chemical Engineering Journal, 102 (1):61.

[66] O'Hayre, R.P., Cha S-W., Colella W., Prinz F.B., 2009. Fuel Cell Fundamentals, 2nd Edition, John Wiley & Sons, Inc., New York, USA, Ch. 3,6.

[67] Campanari S., Iora P., 2004. Definition and Sensitivity Analysis of a Finite Volume SOFC Model for a Tubular Cell Geometry, J. of Power Sources, 132 (2):113.

[68] Bove R., Lunghi P., Sammes N.M., 2005. SOFC Mathematic Model for Systems Simulations. Part One: From a Micro-Detailed to Macro-Black-Box Model, Int. J. of Hydrogen Energy, 30 (2):181.

[69] Lai K., Koeppel B.J., Choi K.S., Recknagle K.P., Sun X., Chick L.A., Korolev V., Khaleel M.,2011. A Quasi-Two-Dimensional Electrochemistry Modeling Tool for Planar Solid Oxide Fuel Cell Stacks, J. of Power Sources, 196(6):3204-3222.

[70] Thomassen M., Sheridan E., Kvello J., 2010. Electrochemical Hydrogen Separation and Compression Using Polybenzimidazole (PBI) Fuel Cell Technology, J. of Natural Gas Science and Engineering, 2(5):229-234.

[71] Perry K.A., Eisman G.A., Benicewicz B.C., 2008. Electrochemical Hydrogen Pumping Using a High-Temperature Polybenzimidazole (PBI) Membrane, J. of Power Sources, 177(2):478-484.

[72] Eisman G., Neumann D., Benicewicz B., Galeano A-M., 2011. H2 Pump, LLC Website, http://www.h2pumpllc.com/5.html. Date Accessed: Feb, 2011.

[73] Mann, M. K., 1995. Technical and Economic Assessment of Producing Hydrogen by Reforming Syngas from the Battelle Indirectly Heated Biomass Gasifier, NREL Technical Report: TP-431-8143.

[74] Leiby, S.M., 1994. Options for Refinery Hydrogen. SRI Report No. 212. Menlo Park, CA.

[75] James, B.D., 2008. H2A hydrogen production analysis software case study: Current (2005) Steam Methane Reformer at Forecourt 1500 kg/day. Available at: http://www.hydrogen.energy.gov/h2a_production.html. Accessed: July, 2011.

[76] Saur, G., 2008. Wind-To-Hydrogen Project: Electrolyzer Capital Cost Study. NREL Technical Report. NREL/TP-550-44103.

[77] Steward, D., Penev, M., 20010. Fuel Cell Power Model: Evaluation of CHP and CHHP Applications," 2010 Vehicle Technologies and Hydrogen Programs, Annual Merit Review and Peer Evaluation Meeting, U.S. Department of Energy, June 7-11, 2010, Washington, D.C., available at http:/www.hydrogen.energy.gov.

[78] Ramsden, T., Steward, D.M., 2008. H2A Hydrogen analysis software case study: Long-Term Hydrogen Production from Central Grid Electrolysis. Available at: http://www.hydrogen.energy.gov/h2a_prod_studies.html. Accessed: July, 2011.

[79] Yang, C., Ogden, J., 2007. Determining the lowest-cost hydrogen delivery mode, Int J of Hydrogen Energy, 32(2):268-286.

[80] Joseck, F., 2010, "Systems Analysis," Annual Merit Review and Peer Evaluation Meeting, U.S. Department of Energy, June 7-11, 2010, Washington, D.C., available at http:/www.hydrogen.energy.gov/.

[81] Steward, D., 2011, personal communication, regarding "Comparison of Various Strategies for Small Scale Production of Hydrogen," Internal report, National Renewable Energy Laboratory, Golden, CO, December, 2009.

[82] Ruth, M.F., Diakov, V., Laffen, M., Timbario, T.A., 2010, "Projected cost, energy use, and emissions of hydrogen technologies for fuel cell vehicles," FuelCell2010-33185, Proc. of ASME 8th International Fuel Cell Science, Engineering, and Technology Conference, June 14-16, Brooklyn, NY.